Changes in Sea Ice Motion and Exchange in the Beaufort Sea: 1997-2012

by

Michael Anthony Brady

A thesis
presented to the University of Waterloo
in fulfillment of the
thesis requirement for the degree of
Master of Science
in
Geography

Waterloo, Ontario, Canada, 2014

Author's Declaration

I hereby declare that I am the sole author of this thesis. This is a true copy of the thesis, including any required final revisions, as accepted by my examiners.

I understand that my thesis may be made electronically available to the public.

Abstract

Sea ice motion and area exchange are investigated within the Beaufort Sea to examine the effects of a diminishing sea ice cover on the dynamics in the region. Monthly sea ice motion estimates are produced by applying a pre-existing ice-tracking approach on sequential overlapping RADARSAT image pairs. Mean July-October sea ice drift over the 1997-2012 time series is estimated to be 4.78 km day^{-1} (±3.30 km day^{-1}). A significant positive trend of 0.07 km day^{-1} $month^{-1}$ is shown for the same period, representing a 1.5% $month^{-1}$ linear increase in ice drift speeds over the 16-year time series. Ice motion results show a consistent positive bias ranging from 0.63 km day^{-1} to 2.02 km day^{-1} in ice drift speeds when compared with 4 independent datasets. Estimates of ice area exchange are calculated for 3 thresholds over the same 16-year period; the results of which reveal that in recent years (2008-2012), westward sea ice area export towards the Chukchi Sea has dramatically decreased to be relatively negligible when compared to exports during 1997-2007. Investigating the root causes of these changes in ice motion and exchange reveal that despite few changes in the overall sea ice circulation pattern in the Beaufort Sea, changes in melt processes brought about by increases in surface temperatures and solar radiation absorption in addition to declines in sea ice concentration, age and thickness are instrumental in changing the Beaufort Sea from being known as a region for sea ice to thicken and mature to a region where sea ice has little chance of surviving summer melt.

Acknowledgements

This work was funded via the department of Aboriginal Affairs and Northern Development Canada and their Beaufort Regional Environmental Assessment program. This research would not have happened without their generous financial assistance.

I would like to acknowledge and thank Dr. Stephen Howell for his endless patience in assisting with the research and writing processes as well as for his willingness to readily share his expert knowledge of Arctic sea ice.

Thanks go to my advisors Dr. Chris Derksen and Dr. Richard Kelly for their guidance, support, and contributions through the research process.

Thank you to Dr. Christian Haas for volunteering to be on my thesis review committee, and for his insight into my research efforts.

Thanks to the many people who have helped me over the years to reach this point, including members of the Cryo-group at the University of Waterloo, the Climate Processes section team at Environment Canada, and the fellow students whom I have met along the way.

Finally, thanks to my parents for believing in me and reminding me about vacations.

Table of Contents

List of Figures

List of Tables

List of Acronyms

AMSR-E	Advanced Microwave Scanning Radiometer – EOS
AO	Arctic Oscillation
APL-UW	University of Washington's Applied Physics Laboratory
APP	AVHRR Polar Pathfinder
APP-x	Extended AVHRR Polar Pathfinder
ASAR	Advanced Synthetic Aperture Radar
ASF	Alaska Satellite Facility
AVHRR	Advanced Very High Resolution Radiometer
CAA	Canadian Arctic Archipelago
CASPR	Cloud and Surface Parameter Retrieval
CICE	Los Alamos sea ice model
CIS	Canadian Ice Service
CIS-ASITS	Canadian Ice Service Automated Sea Ice Tracking System
CMC	Canadian Meteorological Centre
DESDynl	Deformation, Ecosystem Structure and Dynamics of Ice
EASE-Grid	Equal Area Scalable Earth Grid
EOS	Earth Observing System
ERS	European Remote Sensing Satellite
ESRL-PSD	Earth System Research Laboratory - Physical Science Divisions
FFT	Fast Fourier Transform
FYI	First-Year Ice
GCCS	Generalized Curvilinear Coordinate System
IABP	International Arctic Buoy Programme
ICESat	Ice, Cloud and land Elevation Satellite
MODIS	Moderate-Resolution Imaging Spectrometer

MYI	Multi-Year Ice
NASA	National Aeronautics and Space Administration
NCAR	National Center for Atmospheric Research
NCEP	National Centers for Environmental Protection
NEODF-Cat	National Earth Observation Data Framework Catalog
NOAA	National Oceanic and Atmospheric Administration
NRCan	Natural Resources Canada
NSIDC	National Snow and Ice Data Center
PIOMAS	Pan-Arctic Ice-Ocean Modeling and Assimilation System
PPT	Parts Per Thousand
PSC	Polar Science Center
RCM	RADARSAT Constellation Mission
RGPS	RADARSAT Geophysical Processor System
RIPS	Regional Ice Prediction System
RMSE	Root Mean Square Error
SAT	Surface Air Temperature
SHEBA	Surface Heat Budget of the Arctic
SLP	Sea Level Pressure
SMMR	Scanning Multichannel Microwave Radiometer
SSM/I	Special Sensor Microwave/Imager
SSMIS	Special Sensor Microwave Imager/Sounder
URSA-DAAC	User Remote Sensing Access Distributed Active Archive Center
WMO	World Meteorological Organization

Chapter 1. Motivation

1.1. Introduction

Sea ice in the Arctic is an important part of the surface energy balance because it acts as an insulating layer, regulating the energy flux between atmosphere and ocean. Changes in sea ice also affect neighbouring systems including primary production and wildlife sustainability. Moreover, the influence of sea ice variability affects the salinity in the North Atlantic, thus regulating the global thermohaline circulation that distributes heat around the world (Aagaard and Carmack, 1989).

Over the passive microwave satellite record (1979 to present), Arctic sea ice is experiencing decreases in extent in all months of the year with the largest decreases occurring in summer months (Serreze et al., 2007; Meier et al., 2007; Parkinson and Cavalieri, 2008; Comiso, 2012). The September trend between 1979 and 2014 is 13.3% per decade (Figure 1.1). In addition to extent, submarine observations and laser altimetry indicate that in many regions of the Arctic, sea ice thickness has been decreasing since the late 1950s (Figure 1.2) (Kwok and Rothrock, 2009). However, sea ice thickness change since 2007 has experienced little variation thus far (Haas et al., 2010). Research suggests that there are numerous contributing factors to this decline in extent including: larger areas of open water observed in September affecting temperatures and ice albedo feedbacks, a thinner ice cover due to shorter growth seasons, a higher fraction of thick multi-year ice failing to remain through summer melt, and anomalous atmospheric circulation affecting a weaker ice pack (see Stroeve et al., 2012 for a thorough review).

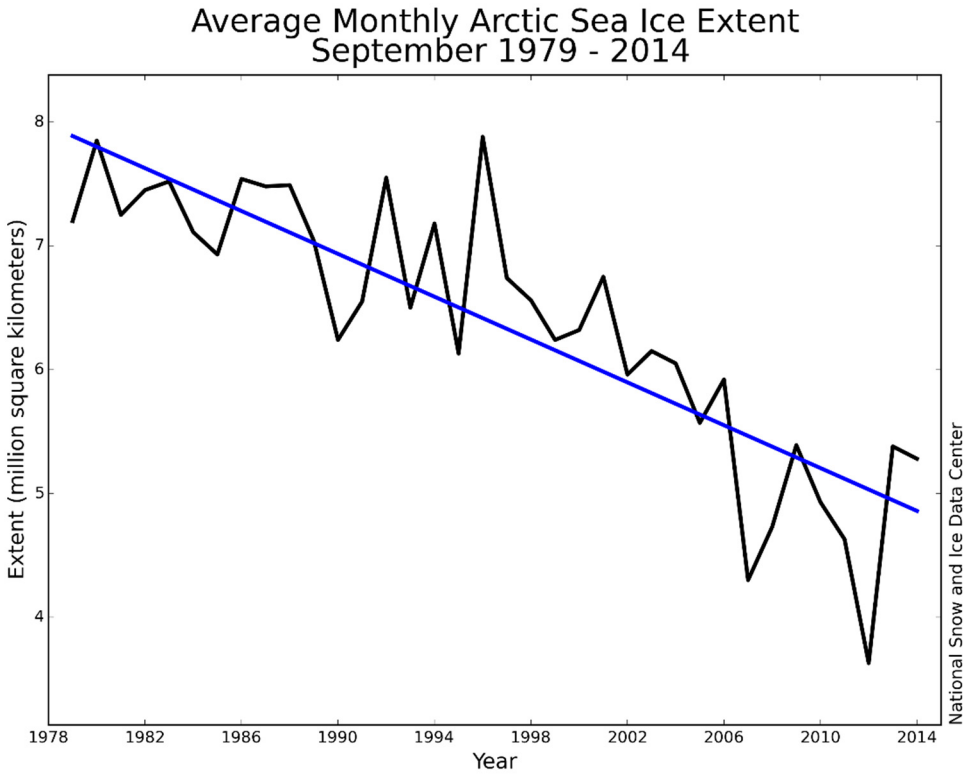

Figure 1.1. Mean September sea ice extent for 1979 to 2014 shows negative trend of 13.3% per decade relative to the 1981 to 2010 climatology. Source: National Snow and Ice Data Center

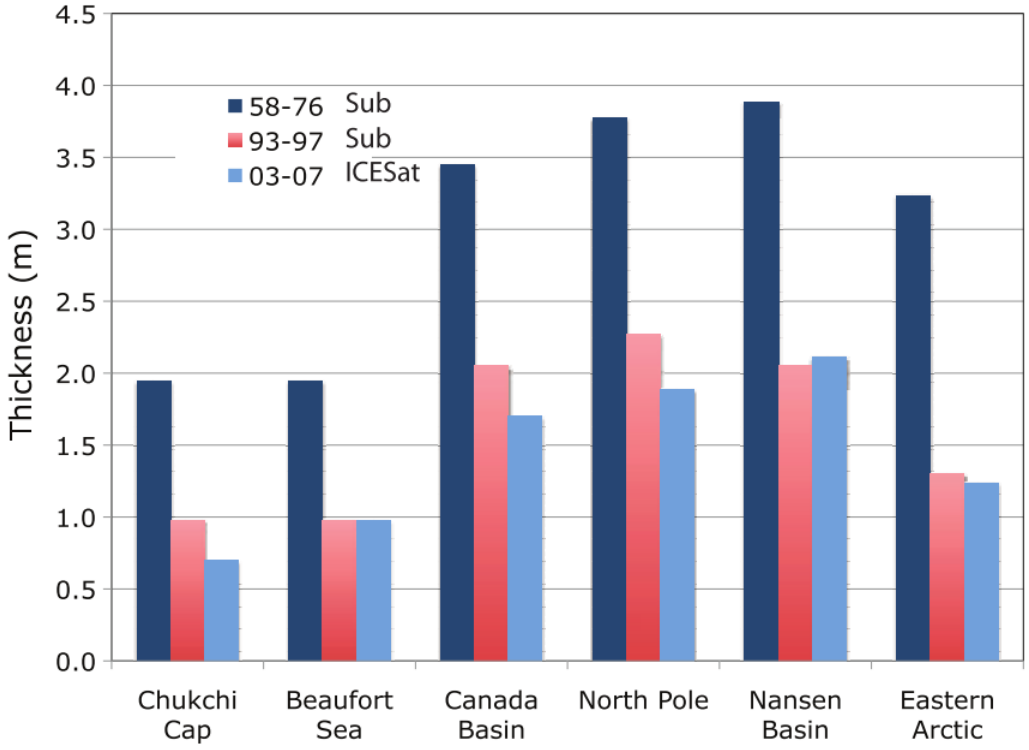

Figure 1.2. Mean ice thicknesses of six Arctic regions for three periods (1958-1976, 1993-1997, and 2003-2007). Thickness measurements have been seasonally adjusted to September 15. Source: (Kwok and Rothrock, 2009)

The Beaufort Sea, situated in the Canada Basin near the North American coastline and west of the Canadian Arctic Archipelago (Figure 1.3), is an area of growing interest for natural resource exploration and maritime transportation due to lightening ice conditions during summer months. Figure 1.4 shows the time series of September total sea ice area and multi-year ice (MYI) area in the Beaufort Sea from 1968-2012. The trend is: -5.4×10^3 km^2 year^{-1} and -4.5×10^3 km^2 year^{-1} for total ice area and MYI, respectively. Historically, the Beaufort Sea was known as a place for sea ice to thicken and mature before recirculating to other regions of the Arctic (Rigor et al., 2002). This process appears to have relaxed in recent years (Kwok and Cunningham, 2010; Stroeve et al., 2011) and the driving processes responsible require more investigation. Previous studies have

typically investigated sea ice dynamic processes within the Beaufort Sea through passive microwave remote sensing, drifting buoy observations, or reanalysis data (e.g. Lukovich and Barber, 2006; Galley et al., 2013; Olason and Notz, 2014). These datasets suffer from coarse spatial resolution (≥25 km for passive microwave, ~2.5º for reanalysis) and relatively sparse observations (~25 buoys in service). The continual availability of RADARSAT satellite data since 1997 allows for the construction of high resolution datasets in the Beaufort Sea that now span 16+ years. The overall goals of this study are to produce a high-resolution (≤25 km) sea ice motion data record for the Beaufort Sea region, and investigate possible driving factors that relate to the recent changes in sea ice variability. These goals are achieved through the following objectives:

i. Estimate monthly sea ice motion for the Beaufort Sea using RADARSAT from 1997-2012 and compare the results with previous methods.
ii. Estimate the sea ice area flux between the Beaufort Sea and its surrounding regions from 1997-2012.
iii. Using the results from i) and ii), explore the drivers of recent variability in sea ice dynamics within the Beaufort Sea.

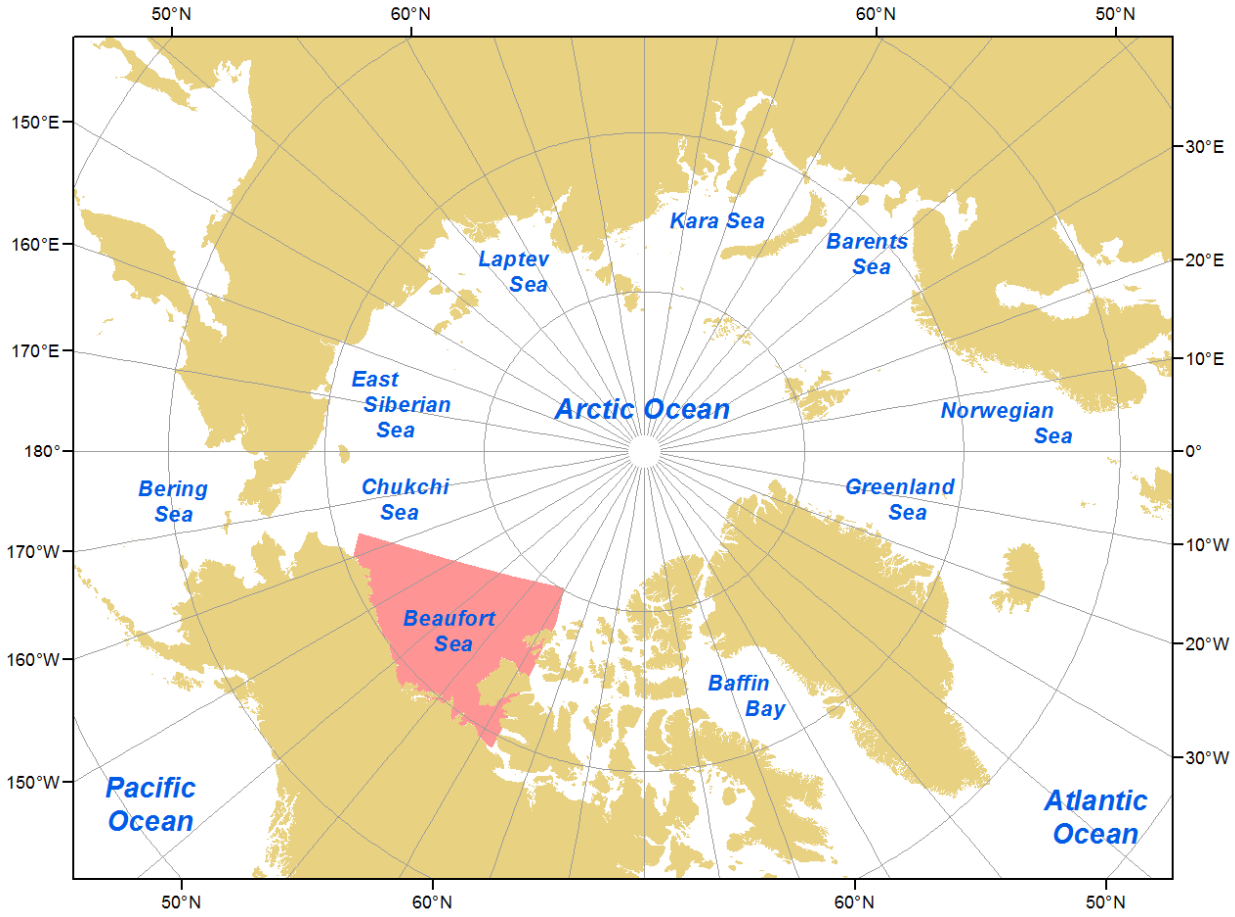

Figure 1.3. Regional overview of circumpolar water bodies. Study area boundaries are highlighted in red.

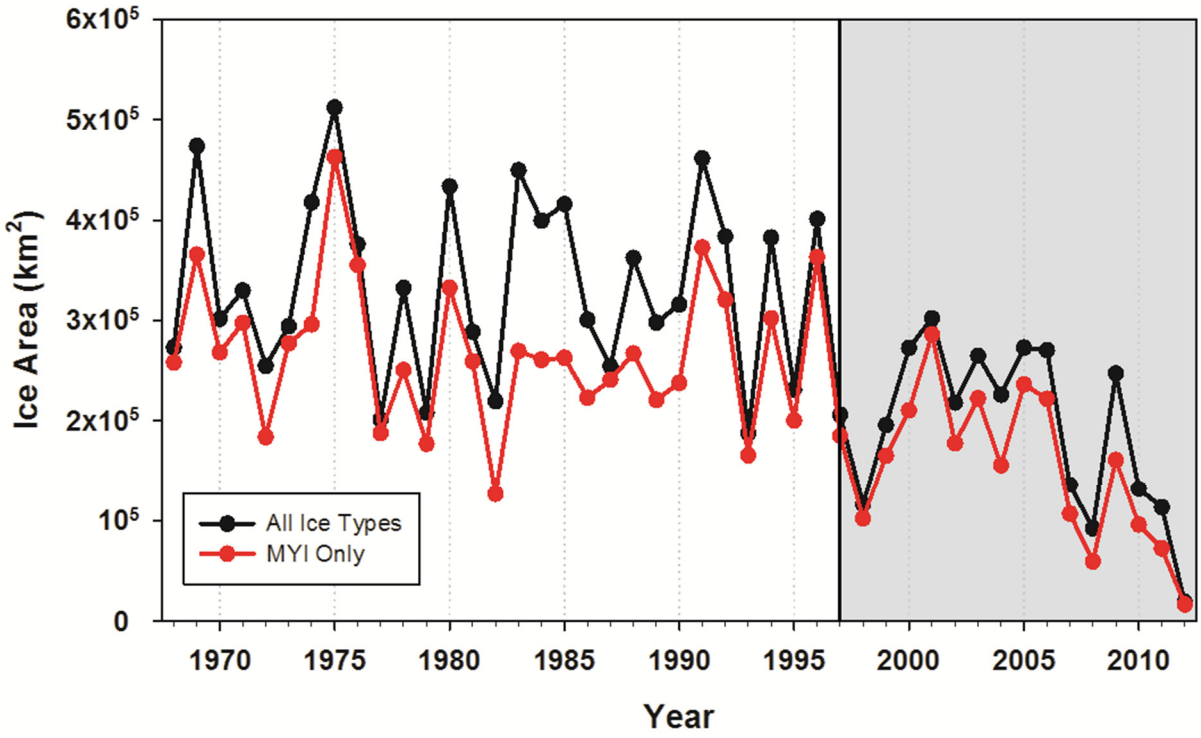

Figure 1.4. Time series of September sea ice extent (1968-2012) in the Beaufort Sea. Shaded area refers to the RADARSAT time period considered for this study (1997-2012). Data source: Canadian Ice Service

1.2. Structure of Thesis

Chapter 2 provides detailed background information on: sea ice characteristics; sea ice dynamic and thermodynamic processes; sea ice as it exists in the Beaufort Sea including regional dynamic and thermodynamic processes. Chapter 2 also reviews microwave remote sensing as it relates to estimating sea ice motion. Chapter 3 describes the data and methods used in this research. Chapter 4 summarizes the results of the RADARSAT-derived ice motion estimates and compares them to previous approaches, summarizes the results of sea ice area exchange estimates, and discusses the drivers of variability and change of sea ice in the Beaufort Sea. Chapter 5 summarizes the key findings and implications of the ice motion and area flux estimation study, and provides

recommendations for future research endeavours involving sea ice motion extraction through active microwave remote sensing.

Chapter 2. Background

2.1. Introduction

Sea ice separates the ocean from the atmosphere and controls the exchanges of energy between the two interfaces. Sea ice cover is composed of ice of varying age, thickness, and salinity which is influenced by changes and variability in dynamic and thermodynamic forces. The proliferation of sea ice across the Arctic is mostly governed by a growth period in the cold winter months and melt in the warm summer months. The majority of sea ice in the Arctic can be considered as a body in constant motion, except in coastal areas where sea ice can be observed to be "fast" or restricted from moving through connections to land or the ocean floor.

Arctic sea ice is exhibiting negative trends in nearly every aspect, from accelerating decreases in overall extent (Serreze et al., 2007; Comiso et al., 2008; Cavalieri and Parkinson, 2012; Comiso, 2012; Stroeve et al., 2012) to reductions in thickness (Rothrock et al., 1999; Kwok and Rothrock, 2009) and age (Maslanik et al., 2007; Kwok, 2007; Comiso, 2012). These declines are associated with positive trends in surface air temperatures (Serreze et al., 2009; Screen and Simmonds, 2010; Comiso, 2012), increases in absorbed solar energy (Perovich et al., 2007; Perovich et al., 2008), and accelerating mean drift speed of sea ice (Rampal et al., 2009; Spreen et al., 2011; Kwok et al., 2013). The Arctic melt season is trending toward earlier melt onset and a later freeze onset resulting in an overall increase in the length of the Arctic melt season by ~5 days decade^{-1} (Markus et al., 2009; Stroeve et al., 2014). Understanding Arctic sea ice change and variability is therefore important because of the potential implications of a decaying ice pack on wildlife habitat (Post et al., 2013), shipping navigation (Stephenson et al., 2011; Smith and

Stephenson, 2013; Pizzolato et al., 2014), natural resource exploration (Barber et al., 2014), and tourism (Stewart et al., 2007; Meier et al., 2014). Of particular importance to shipping and natural resource exploration is the recent state of sea ice properties and trends in the Beaufort Sea, due to the unpredictable effects of mobile ice on transportation and infrastructure planning in the Canadian Arctic.

The objectives of this chapter are to provide a review of i) physical characteristics of sea ice, ii) sea ice variability and change in the Beaufort Sea and iii) the utility of microwave remote sensing for estimating sea ice motion.

2.1.1. Sea Ice Characteristics

Sea ice can be broadly classified into either first-year ice (FYI) or MYI. FYI is ice that has not endured a complete growth-melt cycle (WMO, 1970). FYI is generally composed of weaker, more brine-infused ice that can be more susceptible to melt and deformation events. MYI is ice that has survived at least one growth-melt cycle (WMO, 1970) and is made up of much more resilient ice which is not easily deformed. FYI that is unbroken by ridging (i.e. not deformed) is characterised by a smooth, relatively level surface. MYI has a rougher surface topography composed of low-lying melt ponds surrounded by raised hummocks and also has lower salt content, owing to the years of deformation and melt that it has survived. Without the presence of ridge features or other dynamic influences, FYI formations are typically observed to be thicker than 0.3 m but less than 2.0 m (Wadhams, 2000; Canadian Ice Service, 2005), while MYI formations are usually found to be between 3 and 5 m thick (Serreze and Barry, 2009). Events brought about by sea ice dynamics can vastly increase the thickness of a given ice feature, creating

conditions where below-ocean surface drafts of greater than 10 m can be observed (Bourke and Garrett, 1987). An important distinction must be made between the relative sizes of the sail and keel of a given ice floe, since thickness must take into account that which is above the surface of the ocean ("freeboard"), and that which resides below the surface ("keel" or "ice draft"). The keel of an ice floe is typically much thicker than the sail that is visible above the surface, thus a given floe that appears to be less than 5 m thick from surface observation may actually be much thicker beneath the waterline.

Additional criteria are used to provide spatial information about sea ice which include: concentration, area, and extent. Sea ice concentration refers to the fraction of sea ice relative to the total area of the region. Frequently expressed in tenths, each level of concentration corresponds to a certain ice formation category, ranging from 0/10 or "Ice Free" to 10/10 or "Compact/Consolidated Ice" (Canadian Ice Service, 2005). Sea ice area is calculated by determining the surface area in km^2 of sea ice covering a given area. Ice area is a useful metric for determining the effectiveness of a given growth season, the prospects of sea ice recovery in subsequent seasons, as well as how a subset of the Arctic has reacted to variability in regional weather. Sea ice extent defines given regions as either covered in ice, or not covered in ice. Ice extent estimates typically make use of thresholds of ice concentration (usually ~10-15%) to designate an area being "ice-covered" (Wadhams, 2000).

2.1.2. Sea Ice Thermodynamics

The surface energy balance of Arctic sea ice is given by the following equation from Eicken (2003):

$$(1-\alpha)F_r\downarrow - I_0 + F_L\downarrow - F_L\uparrow + F_s + F_e + F_c + F_m = 0 \qquad (2.1)$$

where α is albedo, $F_r\downarrow$ is the incoming shortwave flux, I_0 is the shortwave flux penetrating into the ice, $F_L\downarrow$ is incoming longwave flux, $F_L\uparrow$ is outgoing longwave flux, F_s is the sensible heat flux, F_e is the latent heat flux, F_c is the conductive heat flux, and F_m is the heat flux due to melting or freezing at the surface. Further details concerning the surface energy balance shown in Equation 2.1 and individual fluxes are discussed in (Maykut, 1986). Sea ice growth and melt occurs on an annual cycle, where the terms in Equation 2.1 favour the development or decay of ice as conditions dictate. Distinct regimes of this cycle have been identified to describe the annual cycle of sea ice and include: freeze-up, winter, early melt/melt onset, and advanced melt (Livingstone et al., 1987). The seasonal evolution is illustrated in Figure 2.1 and will be used to describe the annual cycle of sea ice.

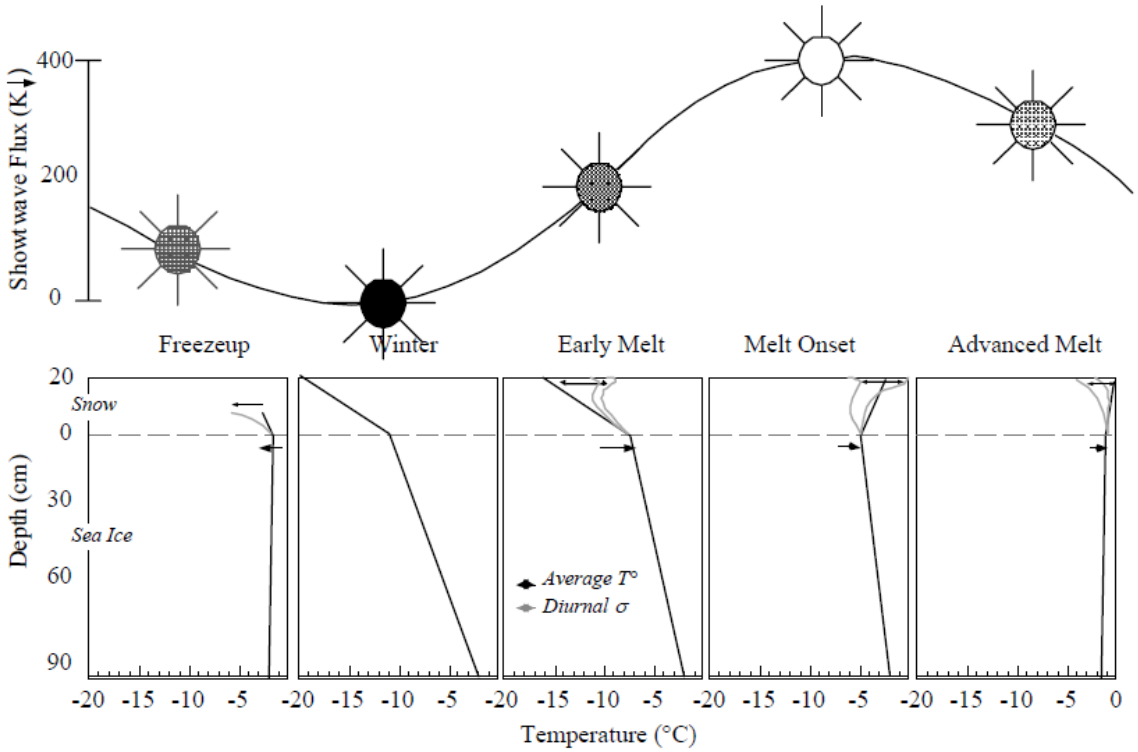

Figure 2.1. Categorical structures of the general thermodynamic regimes representing the seasonal transition from Freeze-up to Advanced Melt for landfast FYI in the Canadian Arctic. Shortwave energy flux term K↓ corresponds to F_r ↓ term used in this study. Source: (Barber et al., 2001)

2.1.2.1. Freeze-Up

The freezing temperature of sea water is slightly lower than 0 ºC at -1.86 ºC (Wadhams, 2000; Eicken, 2003), since the salinity of the water directly affects its ability to solidify (i.e. lowers the freezing point). As the surface of the ocean reaches the freezing point, ice begins to form. Cooling surface water become denser, introducing a mixing of the water column as warm deep water rises to replace the dense cold water. This is known as thermohaline convection and in seawater with a salinity exceeding 24.7 parts per thousand (PPT), mixing continues until the freezing point is reached by the entire water column between the surface and pycnocline layers

(Wadhams, 2000). This uniform cooling of the water column allows for rapid production of frazil ice crystals to take place, which can, in calm waters, form a thin, transparent ice sheet on the surface known as “nilas”. As the nilas layer thickens, it remains transparent (dark nilas) before taking on a grey then white appearance. Congelation growth in the form of water freezing to the underside of the nilas layer produces FYI (Wadhams, 2000).

In rough waters, frazil ice crystals form coherent “pancakes” of ice, so-called for their raised edges of frazil ice which are caused by collisions between pancakes driving frazil crystals upwards between formations. With increasing distance from the marginal ice zone, pancake ice formations increase in diameter and thickness, eventually freezing together to form FYI or more specifically “consolidated pancake ice” (Wadhams, 2000). Pancake ice in the Arctic occurs near the marginal ice zones where rough waters are found, although it is not the dominant ice formation process for the majority of Arctic regions. As ice continues to form on sea water, brine is rejected downwards into the underlying water column which results in further mixing as the dense salt-infused surface layers are replaced by deeper water.

2.1.2.2. Winter

As ice thickens thermodynamically, the rate of growth begins to slow as the cooling effect of surface temperatures must penetrate further into the ice to affect the underlying water (Figure 2.1). Sea ice will continue to grow while the surface temperatures remain below the freezing point of sea water although winter ice growth is also influenced by the oceanic heat flux. (Maykut and McPhee, 1995; Eicken, 2003).

Snow cover on sea ice is another control acting on winter growth, as it is a poor conductor of heat hence, is excellent at insulating ice from heat exchanges (Sturm et al., 2002) and reducing the amount of incoming solar radiation through a high albedo, thus influencing subsequent sea ice cover. Thicker snow covers have steeper temperature gradients within the snow layer (Figure 2.1) which inhibits sea ice thickness growth over the winter. Thinner snow covers enhance ocean heat export to the atmosphere, thus enhancing ice thickening over the winter.

Cloud cover in the winter growth season acts to warm the surface due to longwave radiation being the dominant flux term in the winter energy balance (Wang and Key, 2005). Seasonal variability in the effect of cloud cover on sea ice growth is contingent on the balance between the warming (longwave) and cooling (shortwave) components. As illustrated in Figure 2.2, the cooling phase of cloud cover is due to the presence of low-altitude clouds which act to reflect incoming solar shortwave radiation. The warming phase is also shown, where high-altitude cloud cover traps longwave radiation and reflects it back to the surface. With the absence of clouds, a smaller fraction of incoming solar radiation is reflected or scattered by clouds (thus more incident solar radiation to the ice surface), and the warming effect of longwave radiation reflected back to the surface is reduced.

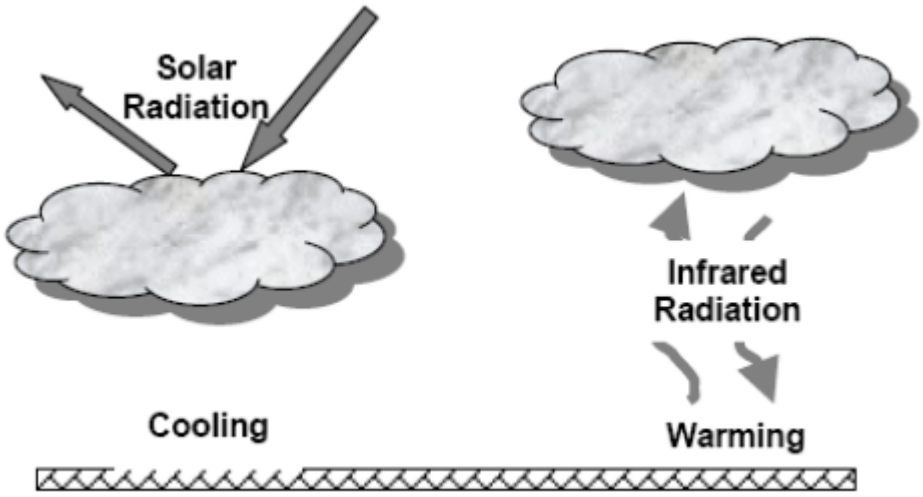

Figure 2.2. Schematic illustration of the solar and infrared effects of clouds on surface temperature. Source: (Zhang, 2004)

2.1.2.3. Early Melt/Melt Onset

As winter transitions to spring, the air temperature and the amount of incoming solar energy increases, signalling the onset of melt. When meltwater on the snow and ice surface surpasses approximately 2% water by volume, melt onset is said to have occurred for the given area (Barber et al., 2001). Snow cover atop the sea ice usually melts from increases in surface temperature and incoming solar radiation and experiences the widest diurnal range of temperatures leading into the early melt/melt onset regimes (Figure 2.1). Wet snow decreases surface albedo which in turn allows for increased absorption of solar radiation and accelerates melt. Warming temperatures enhance melt conditions, which reduces the ice extent, resulting in further melt (Curry et al., 1995). This classic positive sea-ice albedo feedback mechanism is shown in Figure 2.3.

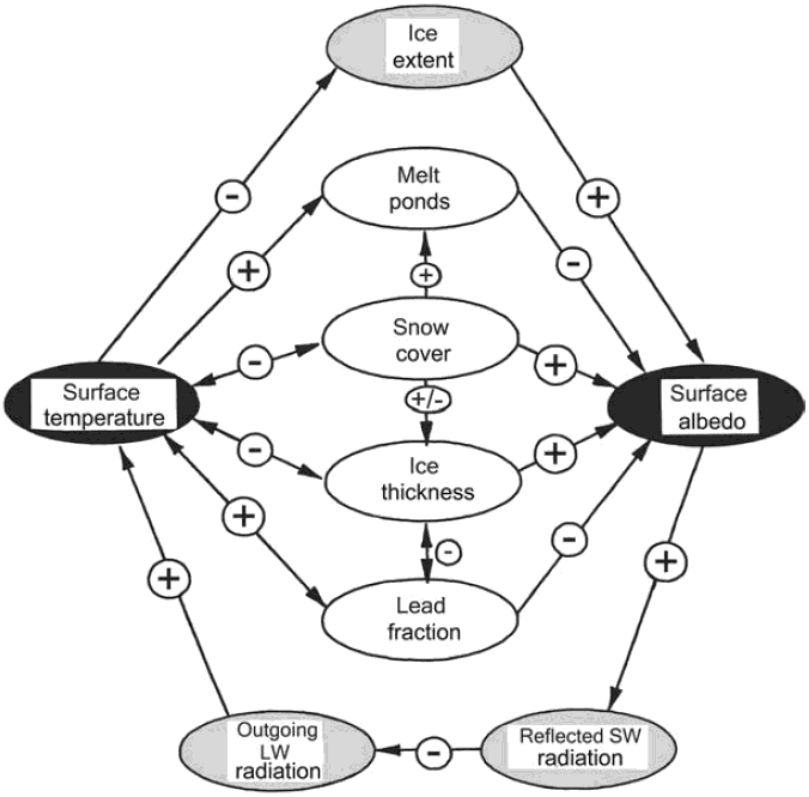

Figure 2.3. Schematics of the ice-albedo feedback mechanism. The direction of the arrow indicates the direction of the interaction. A + indicates a positive interaction (increase in first quantity leads to increase in the second quantity) and a - indicates a negative interaction (increase in first quantity leads to decrease in second quantity). A ± indicates either that the sign of the interaction is uncertain or that the sign changes over the annual cycle. Source: (Curry et al., 1996)

2.1.2.4. Advanced Melt

The advanced melt regime is partially defined by the saturation of above-freezing temperatures in the snow layer (Figure 2.1) and subsequent rapid melt of the snow cover atop sea ice (Barber et al., 2001). As a result, melt ponds at the surface become more prevalent, forming interspersed collections as dictated by the patterns of localised depression of the sea ice surface (Wadhams, 2000). Sea ice melts from the bottom via an imbalance in the oceanic heat flux where

the absorption of energy into the ice-water interface exceeds the outward energy flux (Eicken, 2003). Due to the relatively low albedo of water on sea ice (0.05 – 0.08) compared to bare sea ice (0.4 – 0.7) (Maykut, 1986), melt ponds experience preferential absorption of downward solar radiation, thus deepening into the surface of the sea ice as the melt season progresses.

FYI that has formed during the winter and survived thus far into the melt season usually undergoes a rapid decline in salinity during advanced melt, which weakens the structural integrity of the ice through production of drainage channels. By draining salt content through meltwater channels, the sea ice surface also alters its physical appearance due to the drainage "flushing" patterns within the ice pack and begins to appear more irregular or "hummocky". Melt occurring at the bottom of sea ice is also a component of the summer melt regime and can cause variation in bottom roughness that most often consists of downward "bulges" rather than the depressions seen at the surface (Wadhams, 2000).

2.1.3. Sea Ice Dynamics

Sea ice in the Arctic is in continual motion except for regions where it is landfast. Sea ice motion is determined by the following momentum balance equation from Haas (2003):

$$Ma = \tau_a + \tau_w + F_C + F_i + F_t \tag{2.2}$$

where mass (M) times acceleration (a) equals the sum of aerodynamic drag (τ_a), hydrodynamic drag (τ_w), Coriolis force (F_C), internal ice stress (F_i), and sea surface tilt (F_t). The order of forcing terms in Equation 2.2 are shown relative to highest to lowest weighting, with the drag coefficients usually exerting the strongest influence. Individual definitions of each term in Equation 2.2 are discussed in greater detail in Wadhams (2000). Winds and ocean currents have direct effects on floating ice that serve to influence the speed of ice motion as well as the thickness of the ice in the form of deformation events. Examples of deformation brought about by the movement of ice floes include instances of convergence, where two or more floes are brought together to form pressure ridges of much thicker ice, and divergence, where ice formations break contact and move apart to leave areas of open water (Figure 2.4).

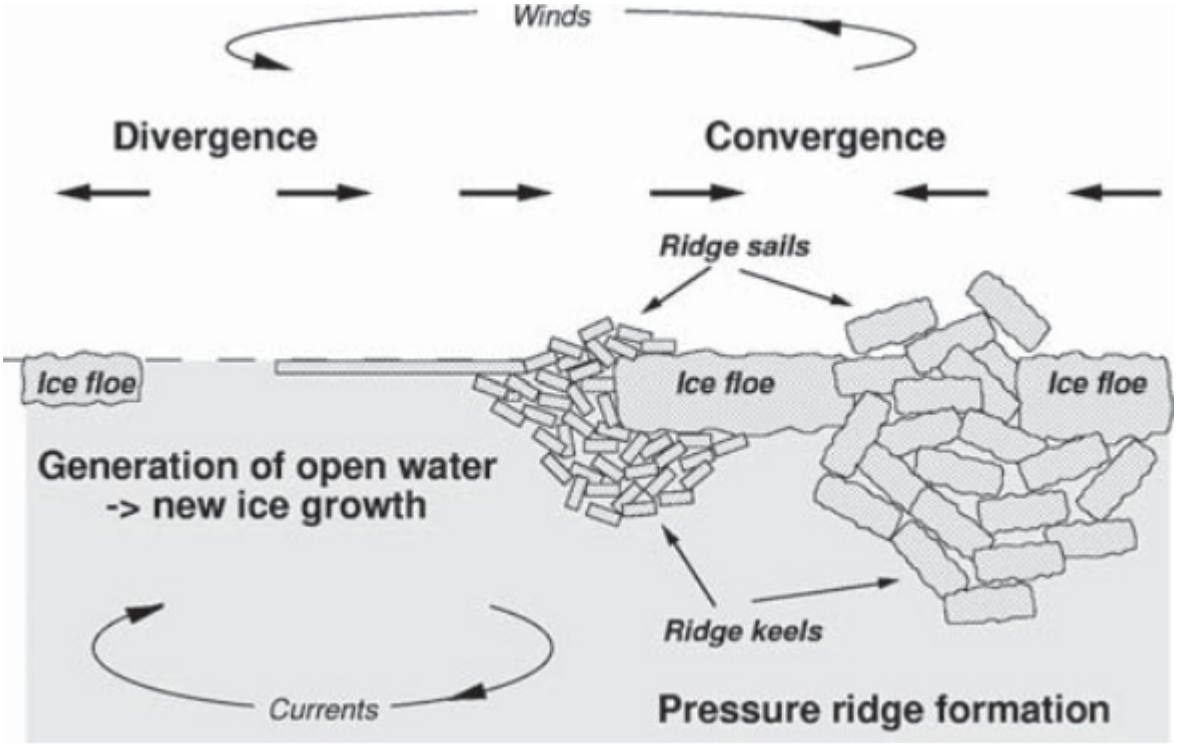

Figure 2.4. Illustration of the processes that dynamically (i.e. by divergent or convergent ice motion and deformation) modify the ice thickness distribution. Source: (Haas, 2003)

2.1.3.1. Convergence

A convergence event is characterized by floating ice coming together under the influence of dynamic forces acting upon them. Deformation in the sense of development of pressure ridges usually follows, which involves broken-up sections of collided floes being pushed tightly together (Figure 2.4). Thin ice is typically more susceptible to deformation than thicker ice, as the mechanical strength is weaker and thus, more easily fragmented. Increases in ice thickness as a result of the creation of pressure ridges are usually more pronounced than ice thickness growth via thermodynamic means (Wadhams, 2000), and the overall regional ice volume is influenced more by dynamic thickening than thermodynamic growth (Haas, 2003).

2.1.3.2. Divergence

Divergence occurs due to opposing drift vectors that result in areas of open water between ice floes (Figure 2.4). The formation of leads and polynynas is the usual by-product of divergence events and these areas can have short to long-term impacts on the sea ice that include new ice growth or enhanced solar energy absorption. Cracks and leads are extended channels of open water that can allow for new ice to grow or can provide an additional avenue for solar radiation absorption. Polynyas can occur on much wider scales and are characterized by their longevity and development in winter conditions when persistent open water is least expected.

Two main types of polynyas are briefly described here, with further detail in Smith et al., (1990). Latent heat polynyas are primarily driven by persistent winds and currents that remove continually-formed ice from the polynya in which it grew. Commonly located in coastal regions, latent heat polynyas balance the heat lost by the ocean through the latent heat of fusion gained by continual new ice formation (Wadhams, 2000). Sensible heat polynyas are a result of oceanic heat fluxes that prevent ice formation, leaving an open water area (Wadhams, 2000). Polynyas and leads are by-products of divergence events that produce areas of open water, thinning or reducing the concentration of the insulating sea ice layer between ocean and atmosphere. Decreases in albedo from more open water implies higher rates of solar radiation absorption and heat exchange between atmosphere and ocean, both of which feed into the classic positive feedback loop mentioned previously.

2.2. Sea Ice in the Beaufort Sea

The sea ice cover of the Beaufort Sea consists of a mixture of FYI and MYI (Figure 2.5). Based on 1981-2010 climatology, sea ice in the Beaufort Sea tends to break up in the first week of June and resumes freeze-up conditions in mid-to-late September (Figure 2.6). The observed (as of April 2009) thickness distribution of sea ice in the Beaufort Sea is roughly bimodal, with a primary mode of ~2.0-3.0 m followed by a secondary mode at ~0.1-0.7 m (Figure 2.7, sectors 6 and 7) (Haas et al., 2010).

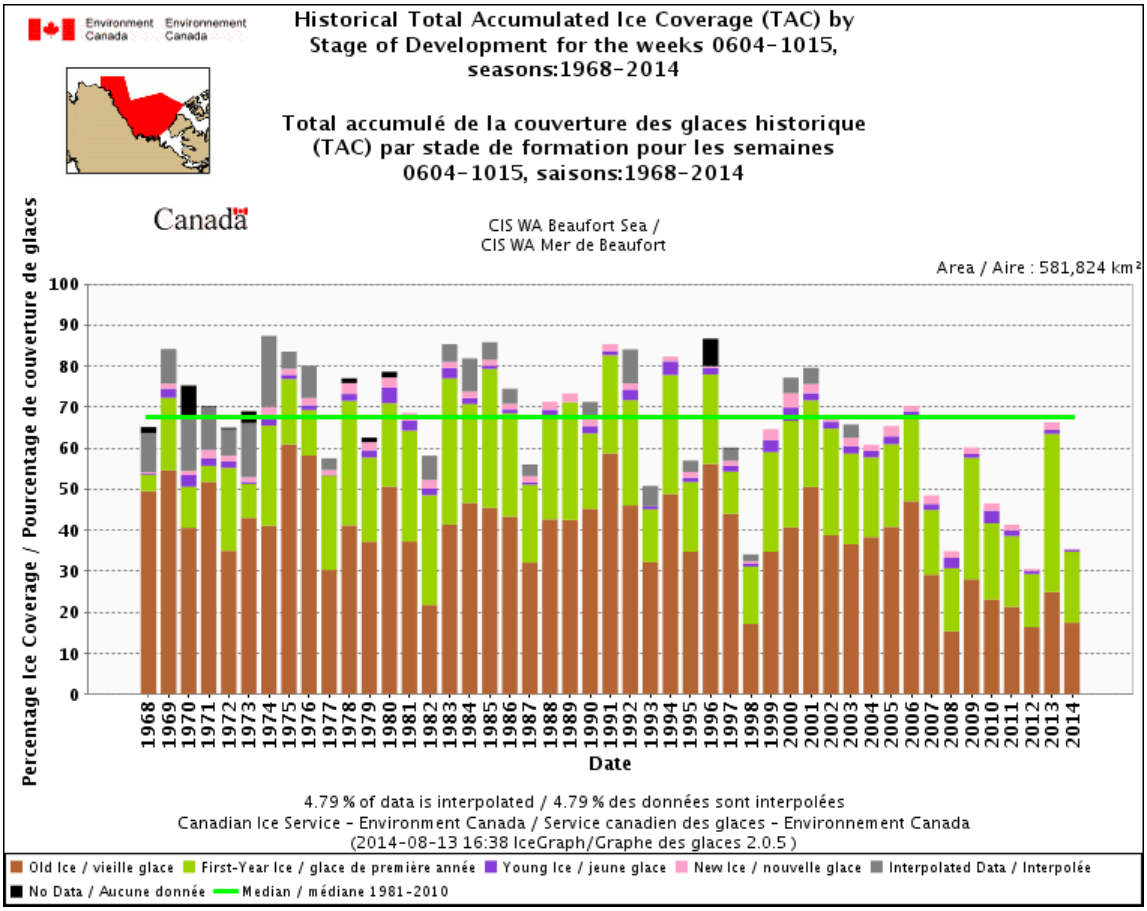

Figure 2.5. Sea ice percent coverage and type composition of the Beaufort Sea region between 1968 and present. Top left inset represents regional boundary constraints. Note that Old ice is also referred to as MYI. Source: Canadian Ice Service

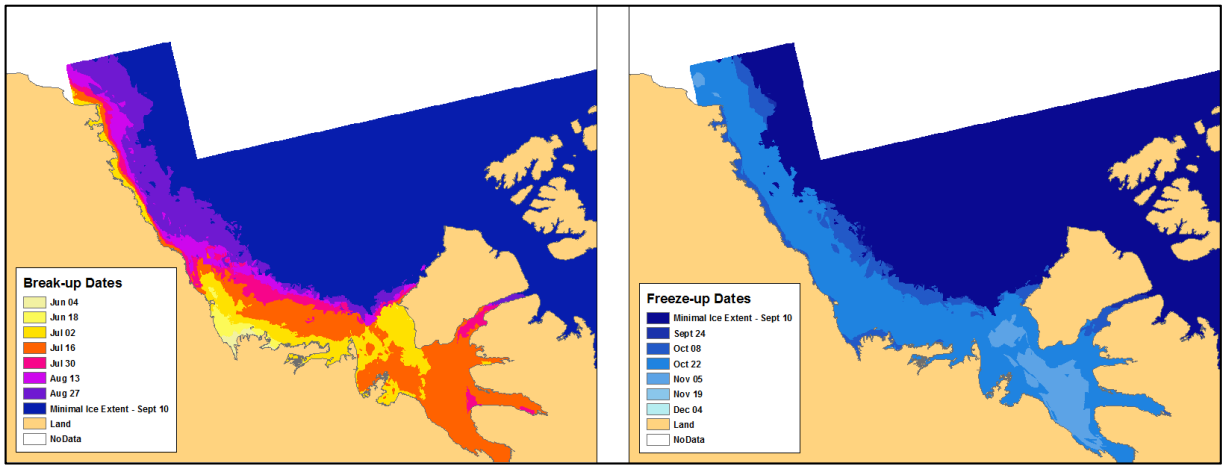

Figure 2.6. Spatial distribution of mean break-up (left; range between June 04 and Aug 27) and freeze-up (right; range between Sept 24 and Dec 04) dates for sea ice in the Beaufort Sea based on 1981-2010 climatology. Data source: Canadian Ice Service

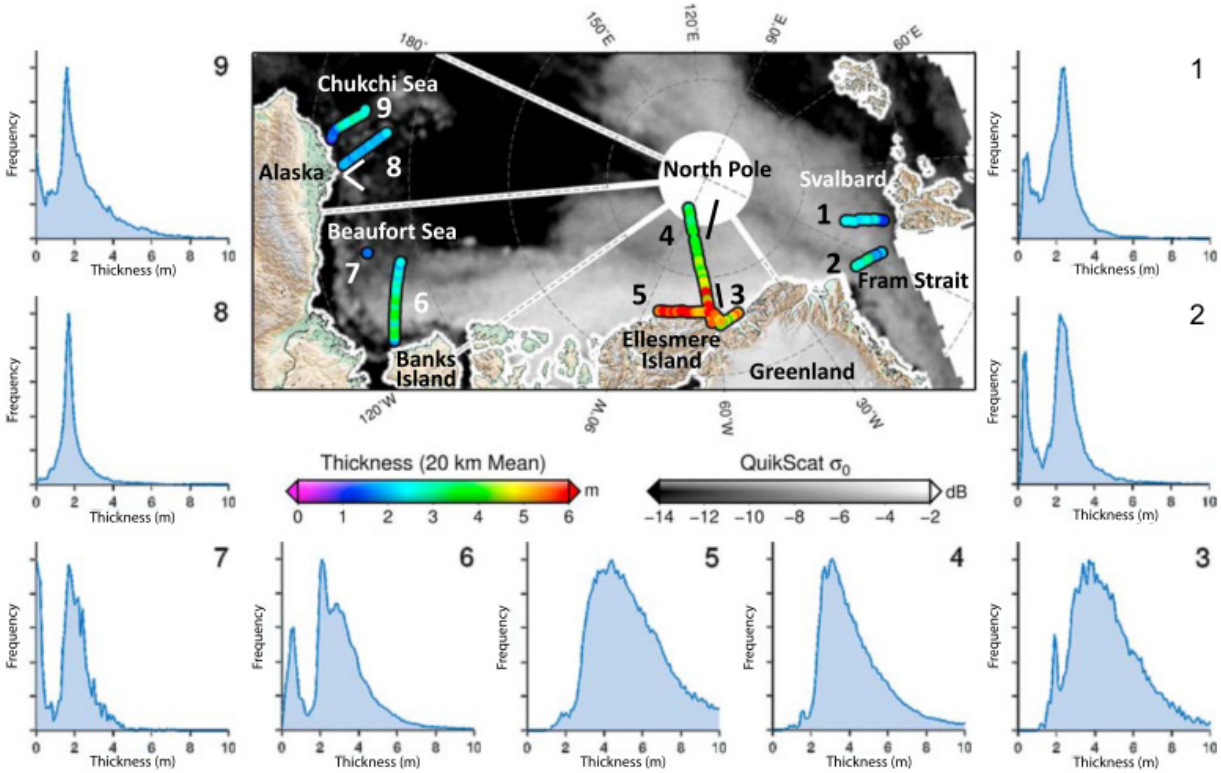

Figure 2.7. Map of the Arctic Ocean showing ice thickness surveys from April 2009. Colors indicate mean thickness of 20 km flight sections. Grey shades represent sea-ice HH-polarized radar backscatter obtained from the QuikSCAT satellite scatterometer. Sectors indicate different radar acquisition dates within ±1 day of respective thickness surveys. Histograms show ice thickness distributions of all nine flights. Flight numbers are indicated in histograms and on map. Source: (Haas et al., 2010)

Sea ice motion in the Beaufort Sea region is dominated by the wind-driven ocean current known as the Beaufort Gyre (Figure 2.8). The Beaufort Gyre is primarily influenced by prevailing winds, salinity changes from freshwater river runoff, and variability in sea level pressure (Proshutinsky et al., 2002; Lukovich et al., 2011). The strength of the primarily anti-cyclonic direction of the Beaufort Gyre is dictated in large part by the presence of a corresponding high pressure system centered north of Alaska, known as the Beaufort High (Thorndike and Colony, 1982; Serreze and Barrett, 2011). The strength and vorticity of the Beaufort Gyre is usually strongest in the late summer near the end of the melt season when sea ice extent is at a minimum and weakest during the winter when ice cover is at its maximum extent. Rigor et al. (2002) demonstrated that variability in strength and location of the Beaufort Sea High was shown to be related to the phase of the Arctic Oscillation (AO; Thompson and Wallace, 1998). A positive index of the AO is characterized by negative SLP anomalies over the polar region (Figure 2.9a) and a negative AO is represented by higher than normal SLP (Figure 2.9b). A positive index AO weakens the Beaufort Gyre, and enhances the export of sea ice via the Transpolar Drift Stream (Figure 2.10). A negative AO favours predominantly anti-cyclonic surface winds, which strengthen the Beaufort Gyre thus facilitating dynamic ice retention and thickening in the Beaufort Sea (Figure 2.10).

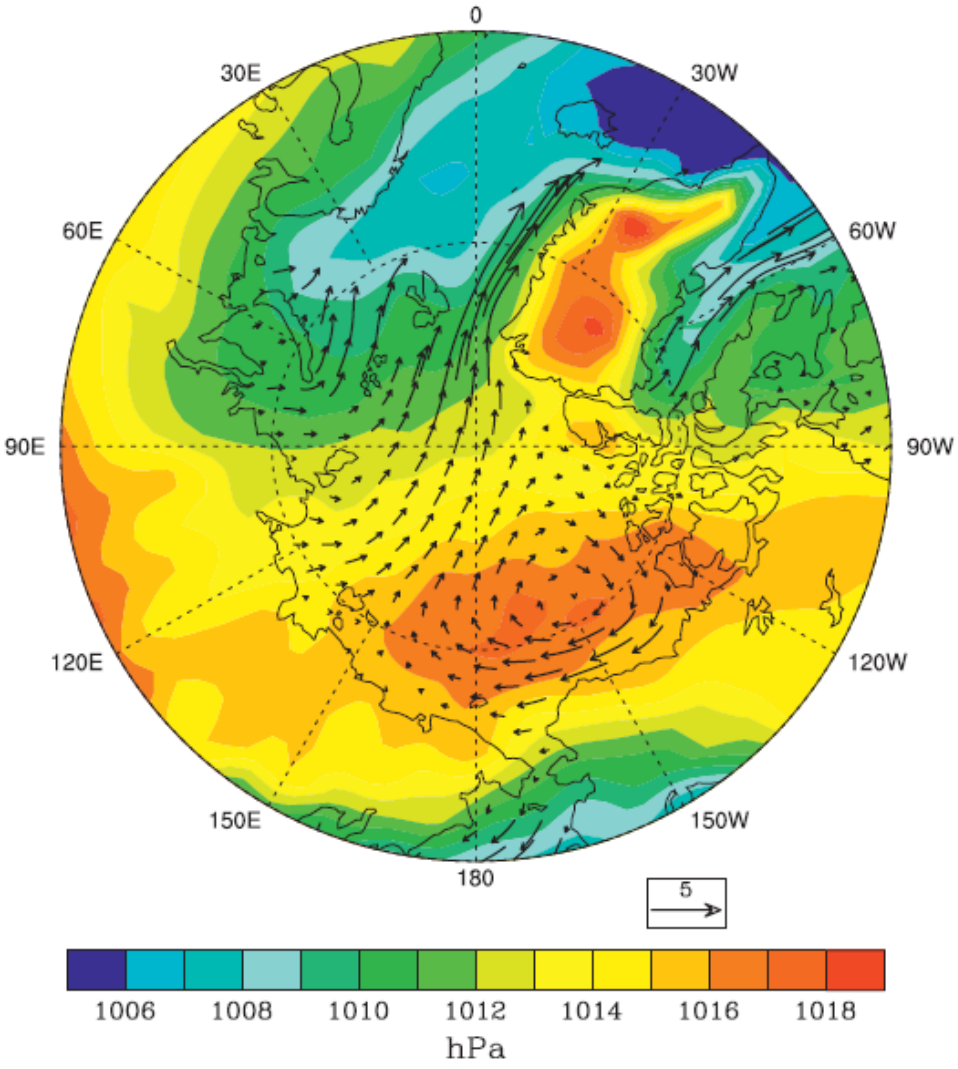

Figure 2.8. Annual mean SLP over the period 1979–2008 from the NCEP–NCAR reanalysis with overlay of mean sea ice velocity vectors for 1979–2006 based on a combination of satellite and buoy data (http://nsidc.org/data/nsidc-0116.html). Ice motion is cm s^{-1}. Source: (Serreze and Barrett, 2011)

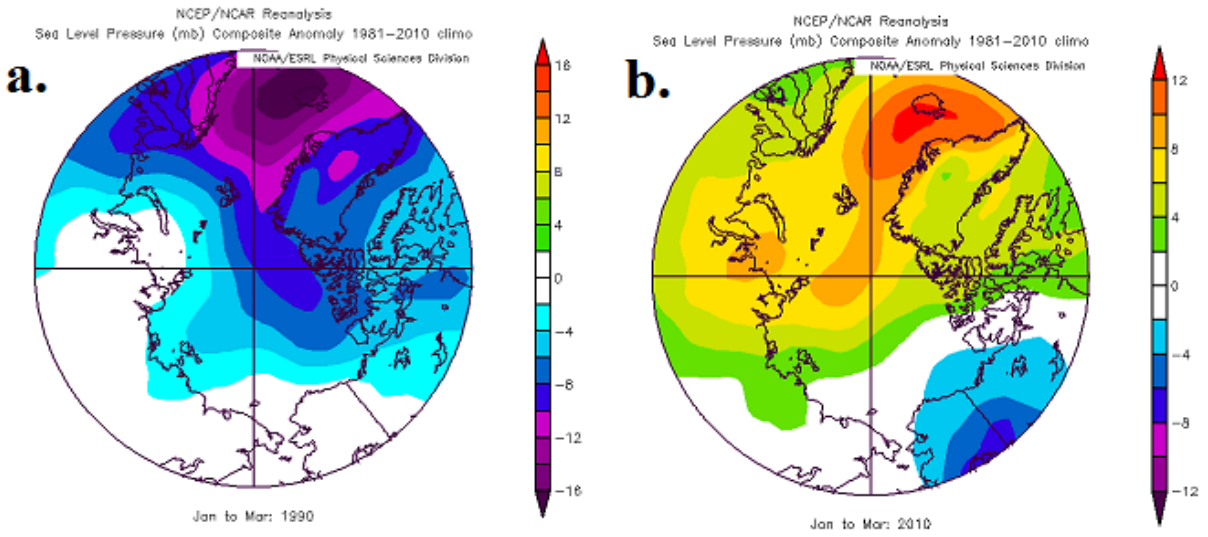

Figure 2.9. Composites of winter (JFM) sea level pressure anomaly showing a positive (a), and negative (b) phase Arctic Oscillation. Source: NCEP/NCAR ESRL PSD

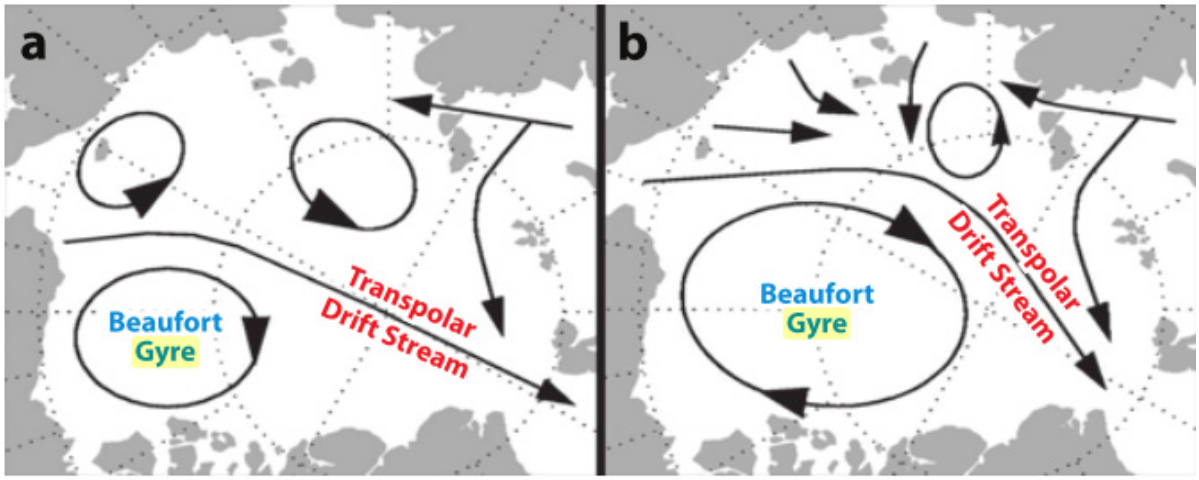

Figure 2.10. General drift pattern of Arctic sea ice for a (a) positive and (b) negative Arctic Oscillation. Source: (Perovich and Richter-Menge, 2009)

2.2.1. Trends and Variability

Sea ice in the Beaufort Sea ice has experienced considerable changes over the past several decades. Between 1968 and 2010, summer total sea ice area in the Beaufort Sea has decreased at a rate of -5.9% decade^{-1}, and -16% decade^{-1} when considering only MYI (Derksen et al., 2012). This represents an additional 0.7% loss rate in total sea ice area from the -5.2% decade^{-1} trend for the 1968-2008 time period reported by Tivy et al. (2011).

Daily average sea ice losses in the Beaufort Sea during July-August (Figure 2.11) show dramatic increases in loss rates during recent years (2007-2010) when compared to the 20-year climatology (1979-2000). These changes are especially evident during June with a loss rate of 7.2 x 10^3 km^2 day^{-1} in 2008 compared to the 20-year mean of less than 1.0 x 10^3 km^2 day^{-1} (Stroeve et al., 2012). The rapid retreat of MYI area in the Beaufort Sea in later years of the 2000-2010 period can be seen spatially in Figure 2.12.

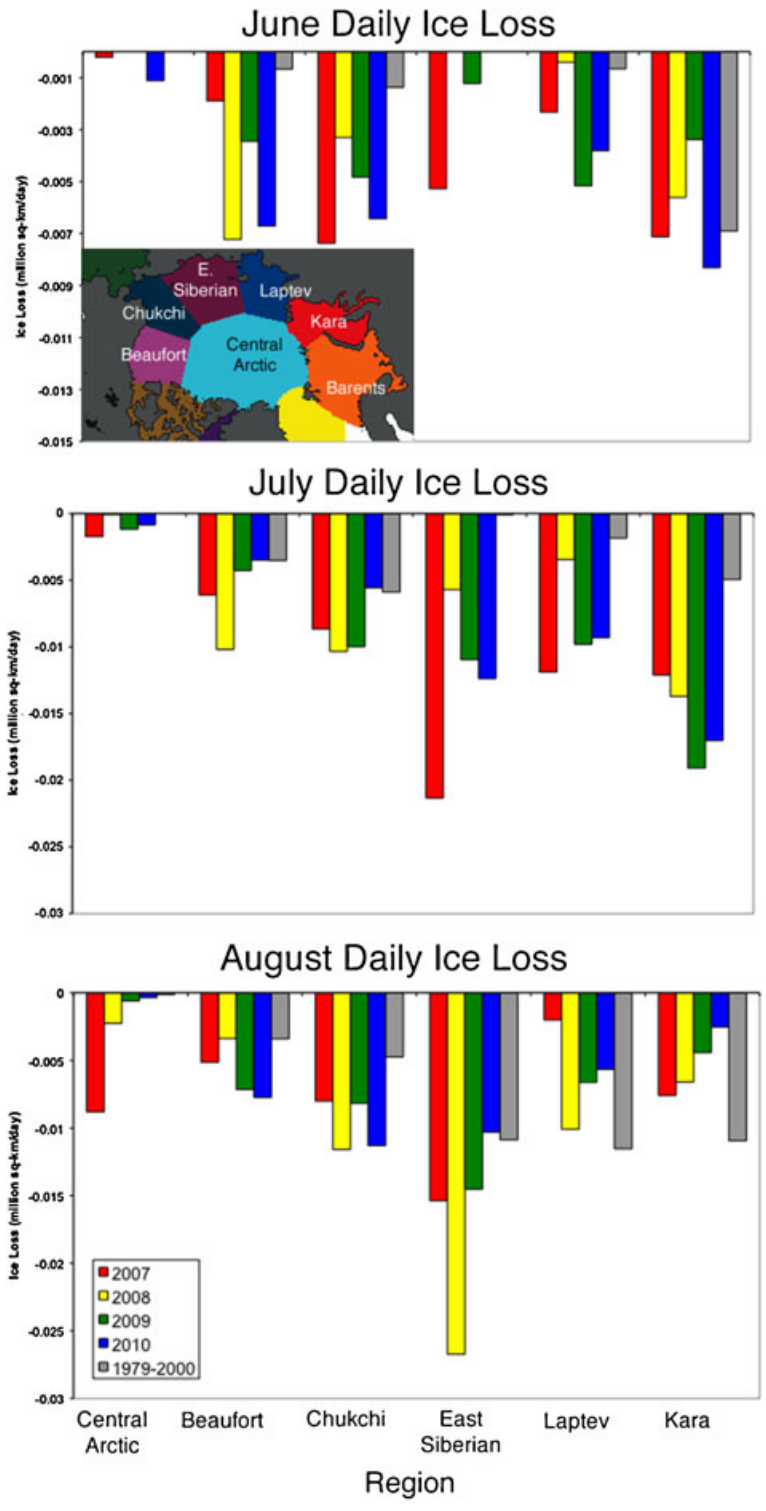

Figure 2.11. Monthly averaged daily ice loss rates for six regions (see inset) from June through August for 2007 through 2010 and for the 1979–2000 average. Source: (Stroeve et al., 2012)

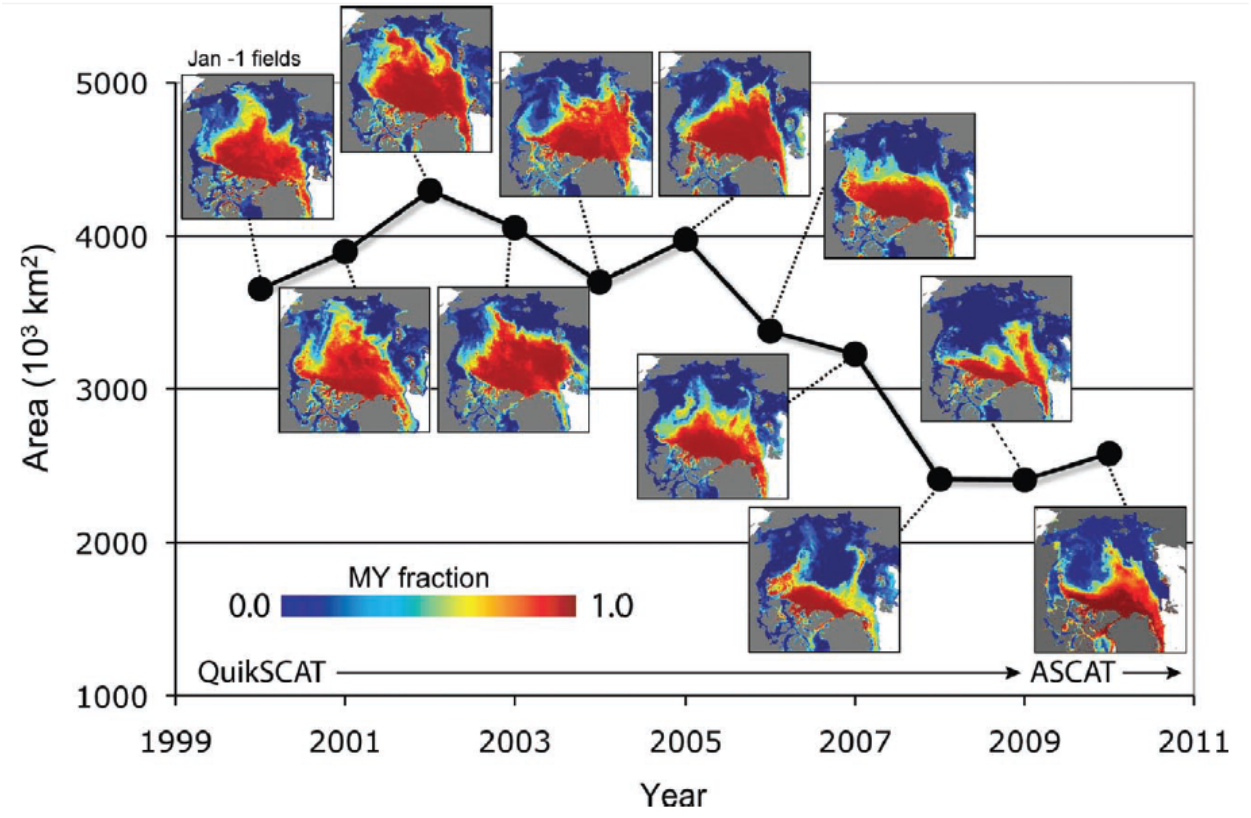

Figure 2.12. Satellite-based Arctic Ocean MYI coverage. Composite time series shows MYI area on 1 Jan each year. Maps show fraction (part of a unit) of MYI. Source: (Polyakov et al., 2012)

The mean overall thickness of sea ice in the Beaufort Sea from submarine sonar and airborne laser altimeter measurements from a series of studies between 1960 and 1982 was observed to be 3.2 m (±1.0 m) (Bourke and Garrett, 1987). Since then, further submarine-based thickness estimates by Rothrock et al. (1999) showed a declining trend between 1993 and 1997 in Beaufort Sea ice draft measurements of -0.14 m year^{-1} compared to an Arctic-wide trend of -0.10 m year^{-1}. Analysis of 1991-2003 ice draft variability in the Beaufort Sea by Melling and Riedel (2005) found that mean draft peaked in winter months with high variability, especially in March as shown in Figure 2.13. Kwok and Rothrock (2009) compared spaceborne laser altimeter measurements of ice thickness from Ice, Cloud and land Elevation Satellite (ICESat) to existing

submarine records, and found that while satellite altimeter measurements showed continuation of negative trends across the Arctic, the Beaufort Sea trend diminished from -0.15 m year^{-1} during 1993-1997 to -0.03 m year^{-1} during 2003-2007. This change in trend manifested in a negligible decrease in mean thickness in the Beaufort Sea between the two periods, as shown in Figure 1.2.

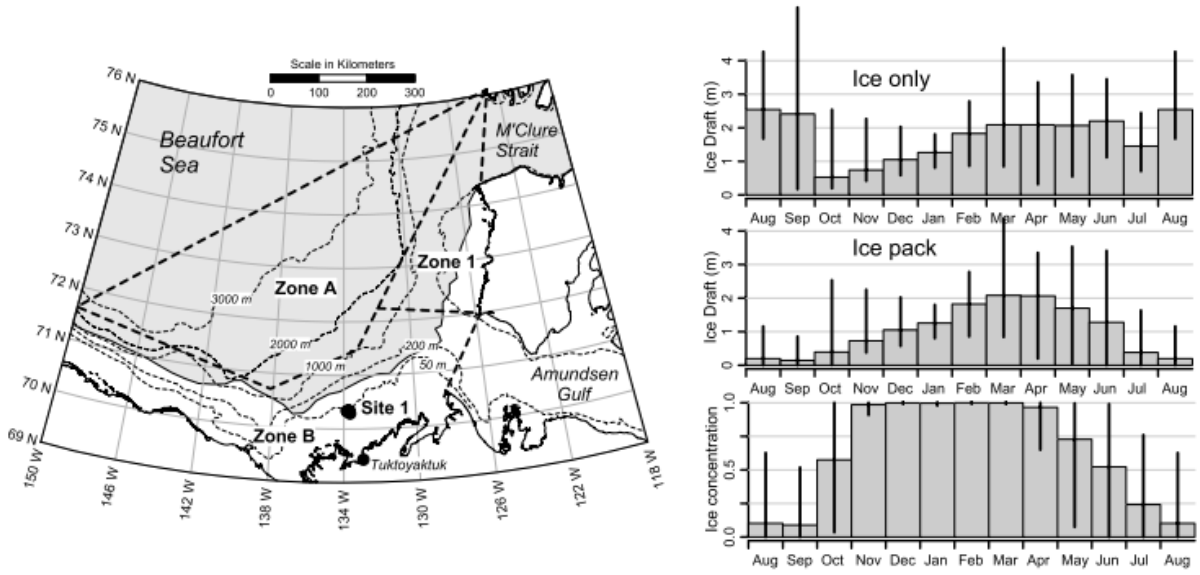

Figure 2.13. Left: Location of Site 1 for seasonal ice monitoring, 1991 to 2005. Shading: typical mid-summer ice extent. Thick dashed lines mark zone boundaries for ice-chart analysis. Right: Annual cycles in the pack ice at Site 1, 1991– 2003, based on monthly averages: draft of ice only (top), ice-pack draft (middle), ice concentration (bottom). Vertical lines span the observed range in monthly means. Source: (Melling and Riedel, 2005)

The survivability of MYI that enters the Beaufort Sea has decreased from 93% between 1981 and 2005 to 73% between 2006 and 2010 (Maslanik et al., 2011). This trend has resulted in a reduction in some of the oldest MYI in the Arctic (Figure 2.14). The recent shift in survival rate (Figure 2.15) has also caused the Beaufort Sea to become one of the primary contributors of summer MYI loss in the Arctic (Maslanik et al., 2011).

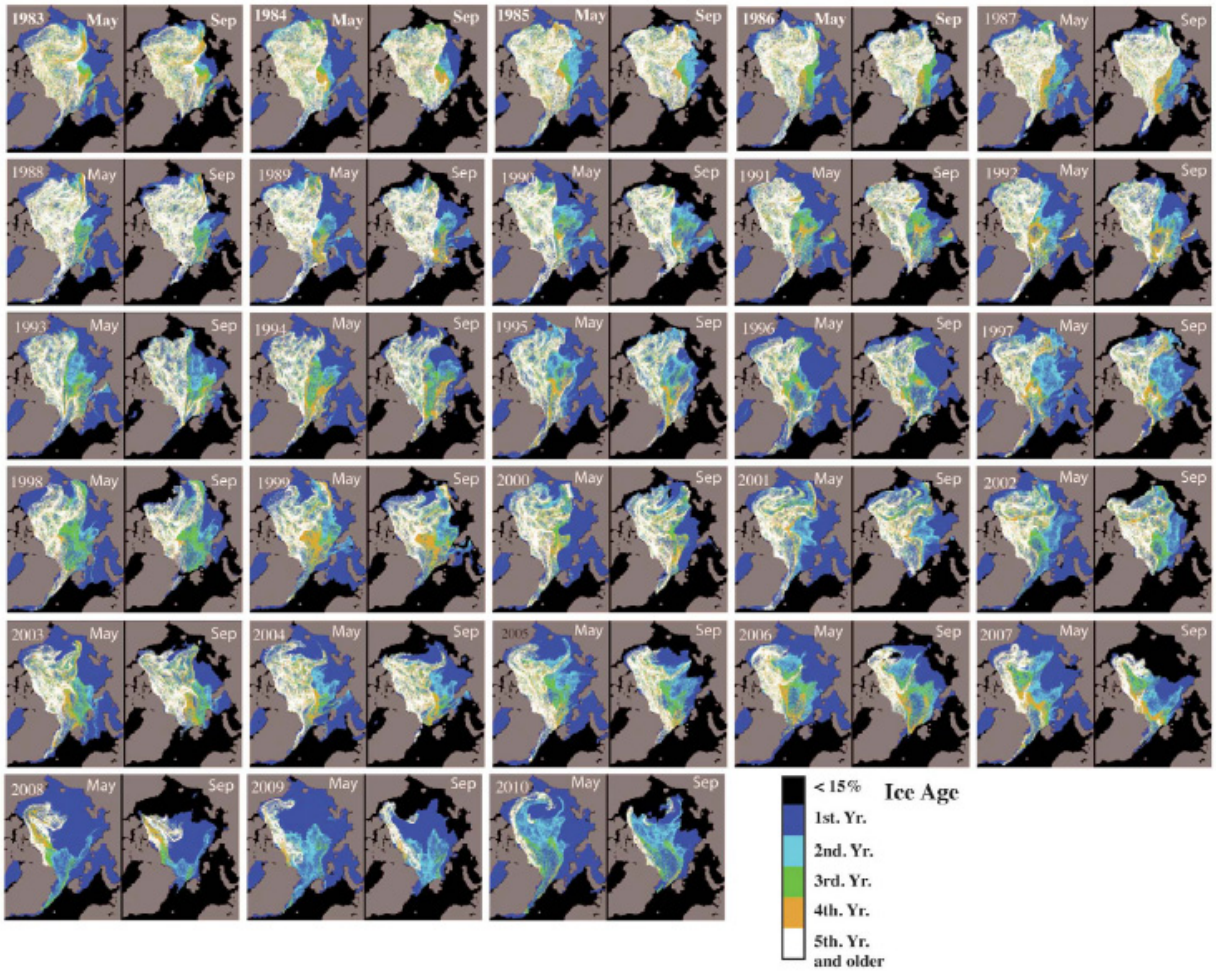

Figure 2.14. Sea ice age for mid-May and at the end of the melt season (September minimum ice extent) for 1983–2010 (with 1983 used as the first year with ice that has survived at least four melt cycles (i.e., "5+ ice"). Source: (Maslanik et al., 2011)

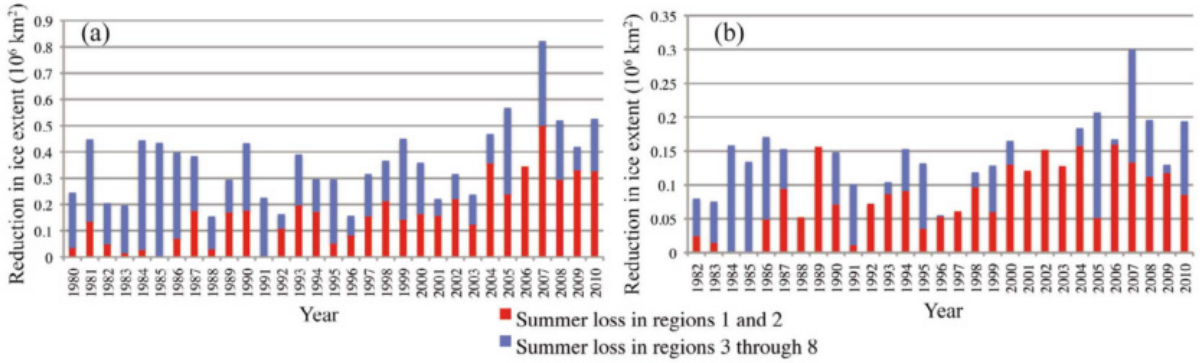

Figure 2.15. Comparison of ice extent loss due to summer melt or convergence within the Beaufort Sea and Canada Basin (regions 1 and 2; red) versus loss elsewhere in the Arctic Ocean (regions 3 through 8; blue) for (a) multiyear ice, and (b) 5+ ice. Source: (Maslanik et al., 2011)

The duration of the melt season in the Beaufort Sea has also been experiencing changes in recent years. Investigations by Stroeve et al. (2014) updating earlier work by Markus et al. (2009) show that the time difference between freeze onset (+6.4 days decade^{-1}) and melt onset (-2.7 days decade^{-1}) has been increasing at the rate of roughly +9.1 days decade^{-1} between 1979 and 2013. This lengthening of the melt season appears to be consistent with past work which showed a trend of +9.2 days decade^{-1} between 1979 and 2005 (Stroeve et al., 2006), although there are key changes from the prior freeze onset and melt onset trends (+4.9 days decade^{-1} and -4.7 days decade^{-1}, respectively; Stroeve et al., 2006).

Sea surface temperature (SST) in the Beaufort Sea has been experiencing warming in both ocean and atmosphere components. Ocean temperature anomalies in the western Beaufort Sea have been exhibiting a positive trend since the late 1960's (Figure 2.16b), while the eastern Beaufort showed somewhat negative temperature anomaly trends during the same period but stabilized in the 1990's before shifting towards positive trends in the early 2000's (Figure 2.16a) (Steele et al., 2008). Recent surface air temperatures for the September 2003-2011 time period show predominantly positive trending in the Beaufort Sea to the order of approximately +0.5ºC year^{-1} (Figure 2.17).

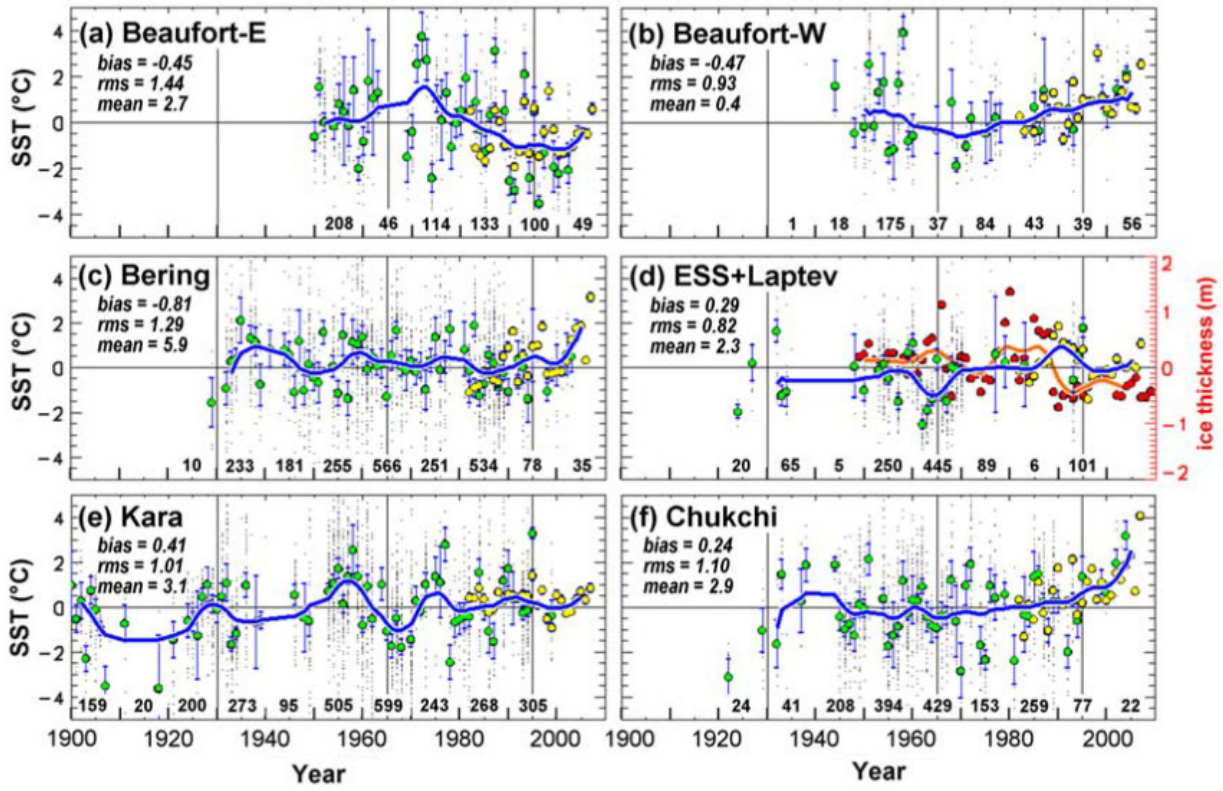

Figure 2.16. Mean summer SST anomalies for six shelf regions. Shown are the 50 km binned in situ input anomalies (gray dots), the regional means of these anomalies (green dots), 95% confidence range of these means (i.e., ±1.96 standard errors, vertical blue lines), and number of 50 km bins with in situ data in each decade (along the bottom axis of each panel). Also shown are the summer-mean satellite-derived SSTs (yellow dots) adjusted by the mean difference over the data record (i.e., bias) of the in situ summer means minus the satellite means. Smoothed regional means (blue curves) are computed from the average in each summer of the green and yellow dots by application of a 3-year running median filter followed by 2 passes of a 5-year running mean filter. Anomalies were computed relative to the mean spatial fields for 1965–1995, and the mean value over each region during this time period is noted in each panel. Vertical black lines indicate the periods 1930–1965 (i.e., ''AO-'') and 1965–1995 (i.e., ''AO+''). Source: (Steele et al., 2008)

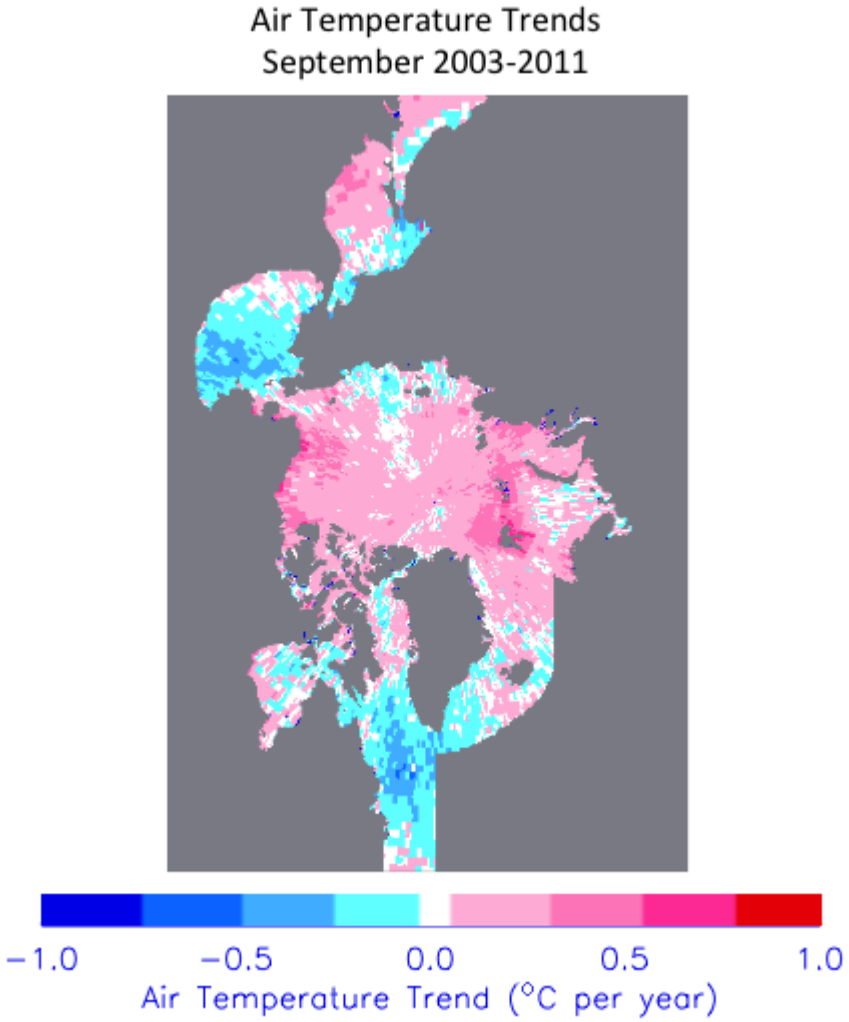

Figure 2.17. Arctic surface air temperature trends for September 2003-2011. Source: (Stroeve et al., 2014)

In recent years, the Beaufort Gyre has been becoming increasingly anti-cyclonic resulting in increases in freshwater accumulation due to influences from geostrophic winds between 1995 and 2010 (Giles et al., 2012). Summer (June-Sept) wind speed trends between 1982 and 2009 were shown to be neutral in the Beaufort Sea (Figure 2.18a), although more regional variability was apparent within the shorter time periods. Winter (Oct-May) wind speed trends during the same temporal range appeared slightly positive in the 1982-2009 time series (Figure 2.19a), with large variability evident at smaller temporal scales.

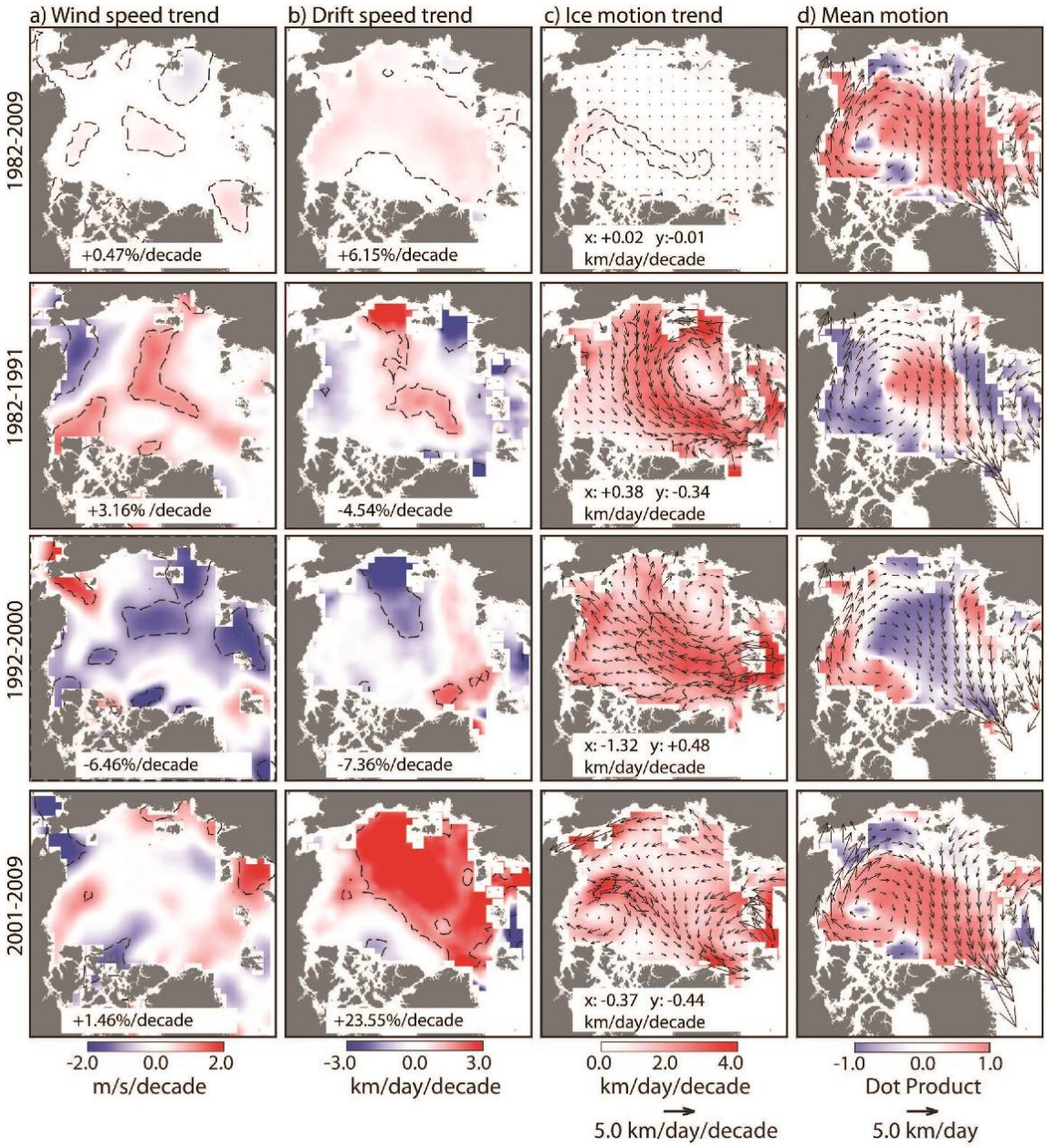

Figure 2.18. Summer (June-September) sea ice motion of the Arctic Ocean for four periods (1982–2009, 1982– 1991, 1992–2000, and 2001–2009). Trends in (a) wind speed, (b) drift speed, and (c) vector ice motion. Dashed lines in Figures (a)–(c) are the 5% significance contours (F-test) from regression analysis of the motion fields after removal of seasonal cycle. (d) Mean motion field. Numerical values are basin-wide spatial averages. Source: (Kwok et al., 2013)

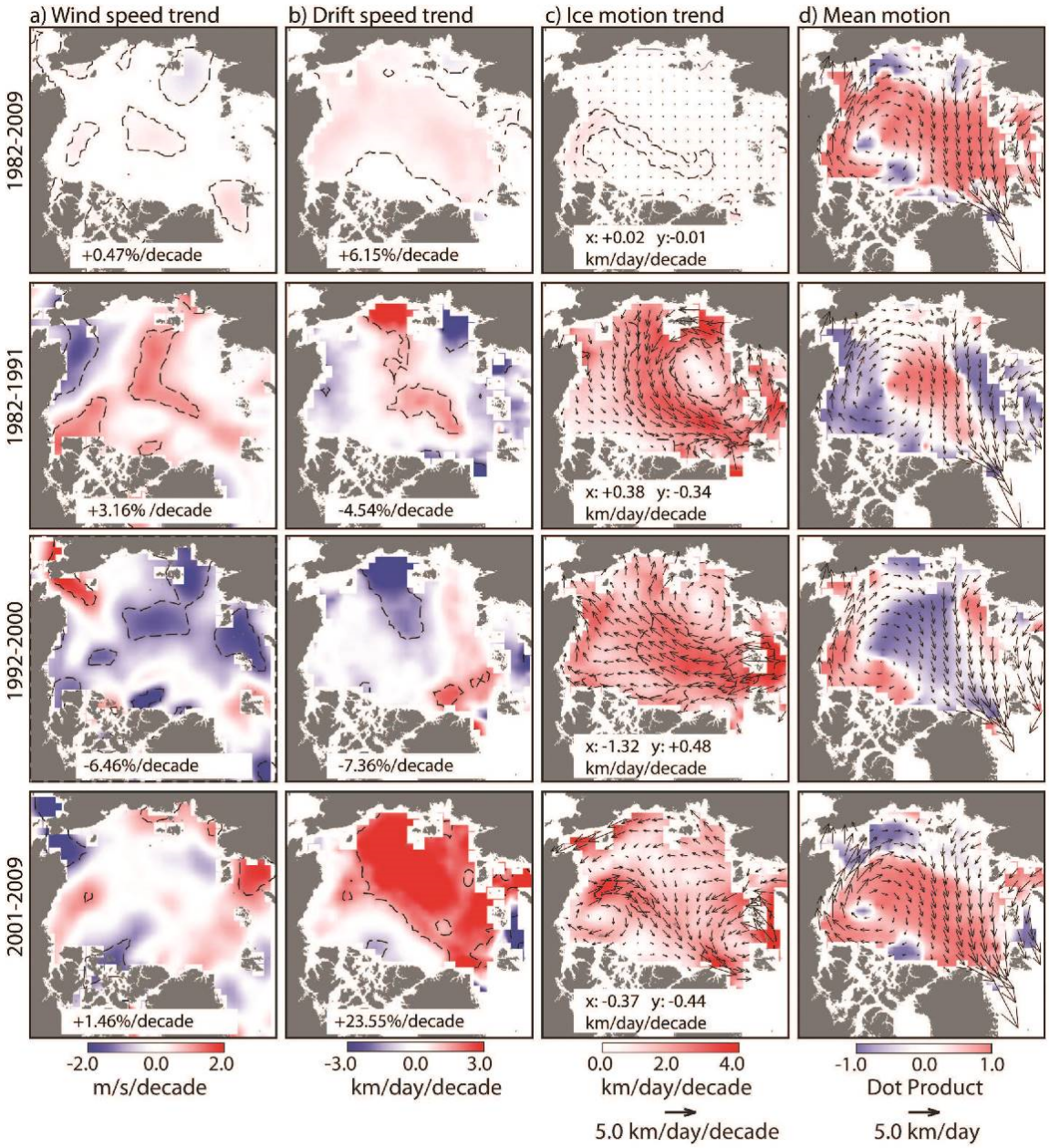

Figure 2.19. Same as in Figure 2.18, but for winter (October-May). Source: (Kwok et al., 2013)

2.2.2. Drivers of Change

2.2.2.1. Thermodynamics

Enhanced melt of MYI in the Beaufort Sea is becoming an increasingly powerful force in the overall reduction of Arctic perennial ice, contributing as much as 32% to the observed decline between 2005 and 2008 (Kwok and Cunningham, 2010). Annual and cumulative loss of MYI due to melt, shown in Figure 2.20, exhibits an extreme maximum of over 2.0×10^5 km^2 during 2008. The linkages between enhanced melt processes and a thinning ice cover are associated with the rapid increase in absorbed solar radiation between 2007 and 2011 (Figure 2.21), which in localised areas of the Beaufort Sea increased by as much as 500% in 2007 (Perovich et al., 2008). The sea-ice albedo feedback mechanism also seems to have an increasingly important role on the thinner ice regime in that it is instrumental in accentuating the effects of larger areas of open water and subsequent increases in surface absorption of solar radiation, causing further anomalies in melt (Perovich et al., 2007; Stroeve et al., 2012).

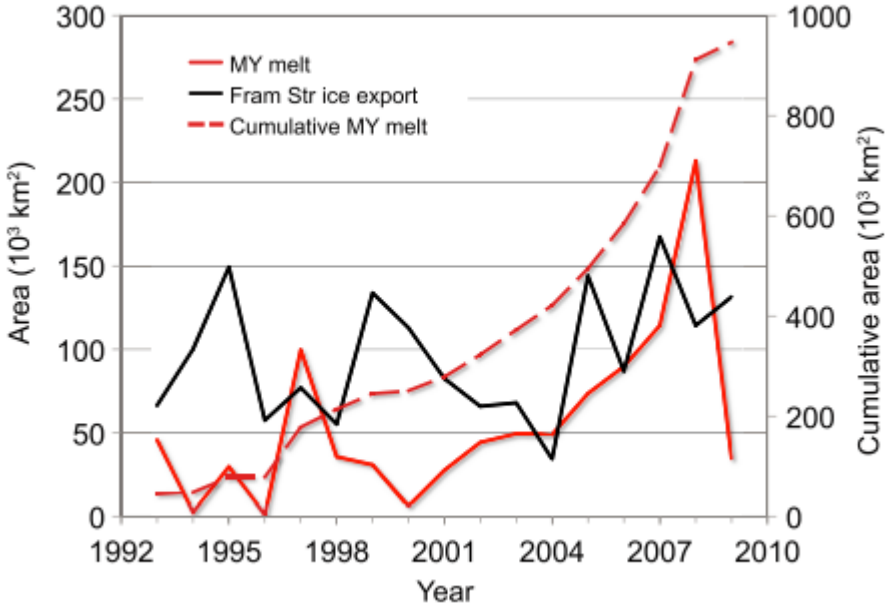

Figure 2.20. Comparison of loss of MYI in the Beaufort Sea (annual and cumulative) with summer Fram Strait ice area export (1993–2009). Source: (Kwok and Cunningham, 2010)

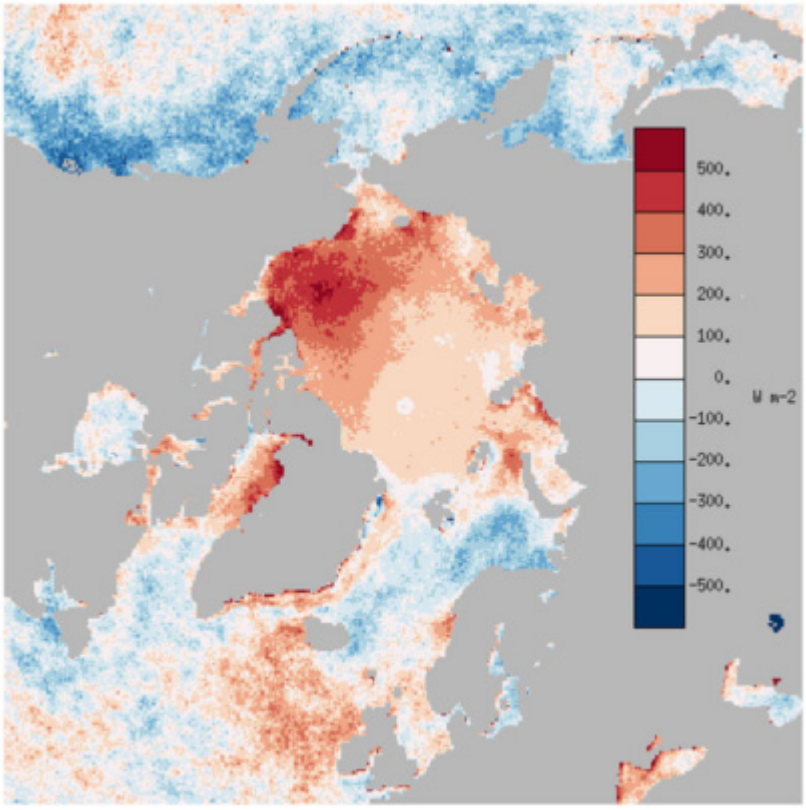

Figure 2.21. Cumulative anomalies in total absorbed solar radiation from 2007 to 2011 relative to 1982–2011. Cumulative solar radiation is summed from May through September based on surface albedo and incoming solar radiation data from APP-X. Source: (Stroeve et al., 2014)

2.2.2.2. Dynamics

Sea ice in the Beaufort Sea was also influenced by atmospheric circulation associated with the AO pattern, especially during the shift to a strongly positive-phase of the AO in 1989. Between 1989 and 1995, conditions brought about by the persistent positive AO served to reduce the amount of older (5+ year) MYI, thus shifting the age composition of Arctic sea ice to one of predominantly thinner and younger sea ice (Figure 2.22) (Rigor and Wallace, 2004). The consequences of this new thinner ice regime became apparent in the 2009/2010 winter season, where a strong negative AO enhanced the anticyclonic Beaufort Gyre rotation, increasing westward ice advection in the

Beaufort Sea to abnormally high levels (Figure 2.23). The vulnerable state of sea ice was further emphasized when after transport to the western Beaufort and Chukchi Seas, almost none of the ice survived the following 2010 melt season (Figure 2.24) (Stroeve et al., 2011).

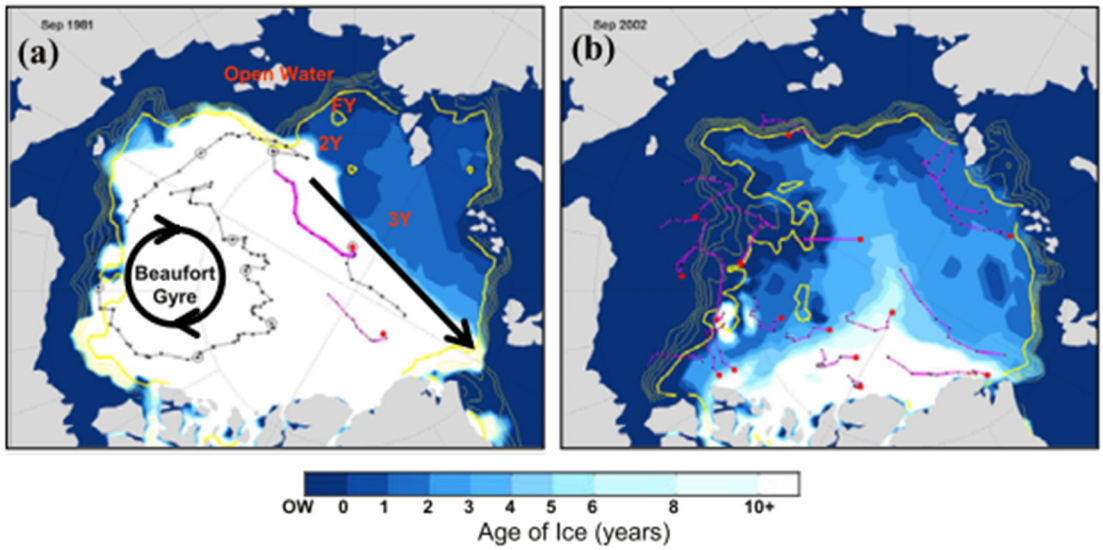

Figure 2.22. Age of oldest sea-ice in September 1981, and September 2002 based on the simulation. Open water (OW) is shown as dark blue, and the oldest ice is shown as white. The Beaufort Gyre and Transpolar Drift Stream are also shown (black arrows).Source: (Rigor and Wallace, 2004)

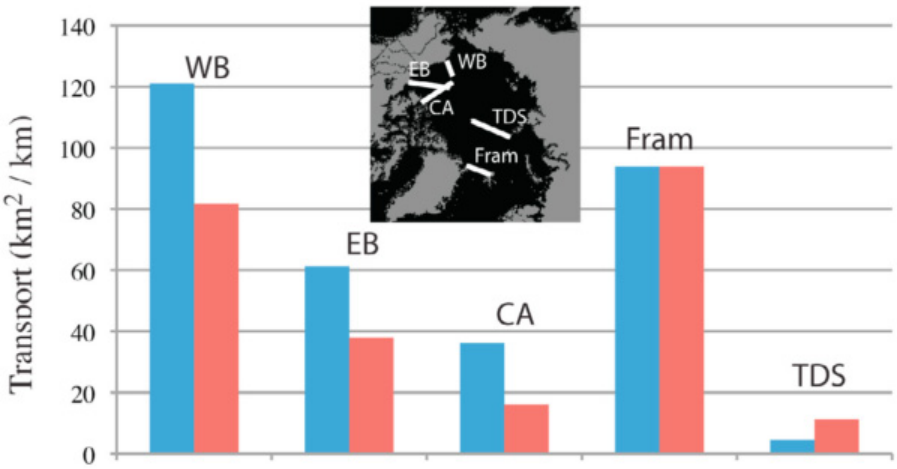

Figure 2.23. Total areal ice transport across gates (see inset map) in the western Beaufort (WB), eastern Beaufort (EB), western end of the region north of the Canadian Archipelago (CA) (all three positive for westward transport), Fram Strait (Fram) and the Transpolar Drift Stream (TDS) (both positive for transport towards the Atlantic) for October 2009 through March 2010 (blue). Climatological transport rates are computed from 1979 to 2009 (red). Source: (Stroeve et al., 2011)

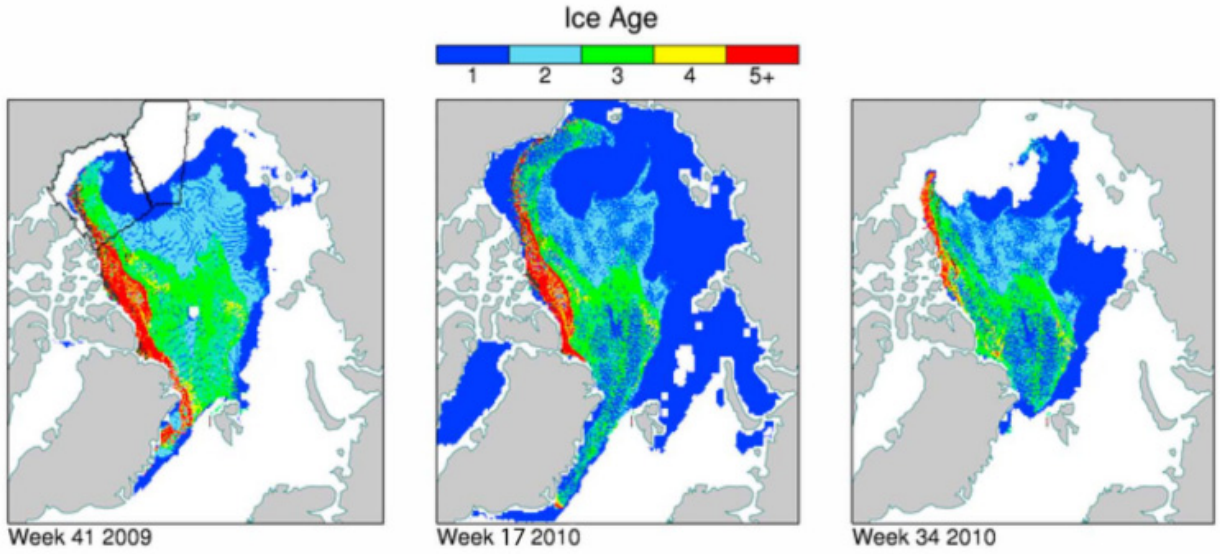

Figure 2.24. Ice age for (left) week 41 (mid-October) 2009, (middle) week 17 (end-of-April) 2010 and (right) week 34 (mid- August) 2010. Black lines delineate the Beaufort and Chukchi sea regions. Source: (Stroeve et al., 2011)

2.3. Microwave Remote Sensing of Sea Ice Dynamics

Satellite remote sensing can be used to quantify sea ice motion (Kwok et al., 1990; Emery et al., 1995; Hamidi et al., 2010; Komarov and Barber, 2012). Notable examples of sensors used for Arctic studies include SSM/I, AMSR-E and MODIS, AVHRR, QuikSCAT, RADARSAT, ERS SAR, and Envisat ASAR, among others. Passive microwave sensors are ideal because of their wide coverage and high temporal resolution, but suffer from coarse spatial resolution (≥25 km). Active microwave sensors have high spatial resolution which allows them to observe relatively local ice pack characteristics, however they are limited by narrow swath widths (poor repeat time) and a lack of confidence when identifying sea ice features brought about by wet surface conditions during the melt season.

2.3.1. Techniques for Estimating Sea Ice Motion from Satellite Imagery

Extracting ice motion information from passive or active imaging sensors typically consists of analysis of overlapping images over the same region which can be constructed into a time series. Sea ice motion products are typically produced in two distinct methods; the grid-based sampling approach of Eulerian motion and the continuous feature-tracking approach of Lagrangian motion. Eulerian sea ice motion products follow the more conventional notion of deriving oceanic transport mechanisms where a regularly-spaced grid is overlaid on the study area and samples of displacement vectors are taken for each grid cell over the desired temporal period (Figure 2.25). The result of this type of analysis is usually representative of an instantaneous estimate of either daily, 3-day, weekly, monthly or annual averages of sea ice motion. Conversely, Lagrangian ice motion datasets begin with a gridded ice motion product but evolve into continuous features for

unique ice floes rather than instantaneous estimates at a fixed location (Figure 2.26). As identifiable ice floes are discovered in the study area, a new displacement vector is produced and updated as the parcel of ice moves through time. This type of measurement can be more insightful as to how sea ice is displaced under real-world conditions (Lindsay and Stern, 2004; Kwok, 2006). Typical Lagrangian ice motion products are on the order of daily, weekly or monthly time scales (Kwok et al., 1990; Drobot, 2003; Lindsay and Stern, 2004). Results of Lagrangian ice motion analysis have been used in previous studies to determine the temporal and spatial evolution of sea ice age (Fowler et al., 2004; Maslanik et al., 2011), as shown in Figure 2.14.

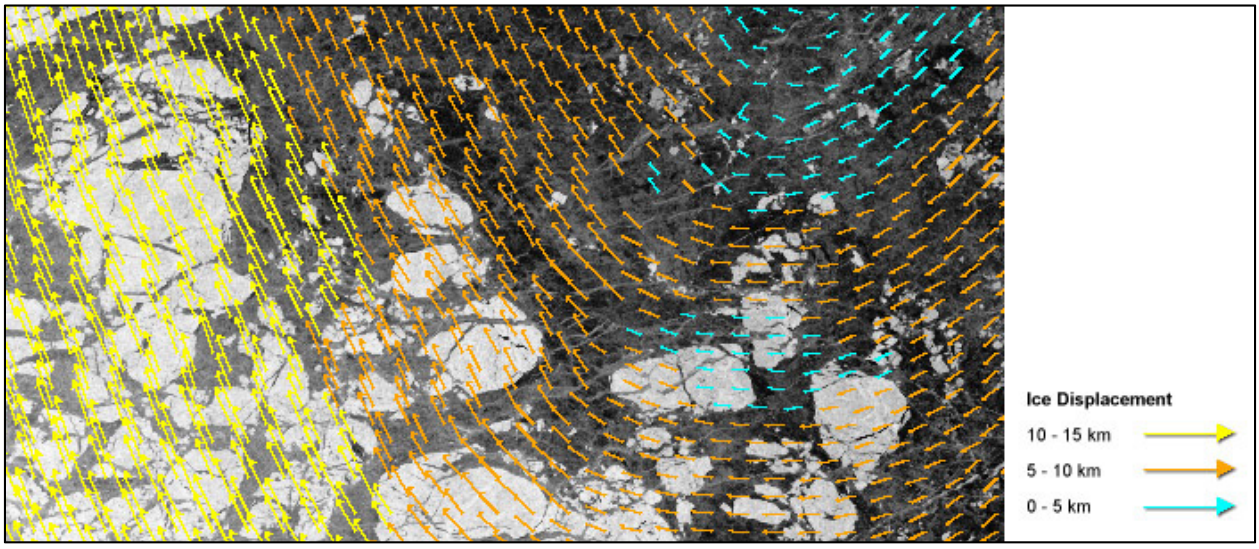

Figure 2.25. Eulerian gridded ice motion product from GlobICE system. Imagery used to derive ice motion information retrieved from Envisat ASAR. Retrieved from: www.globice.info/Section.php?pid=26

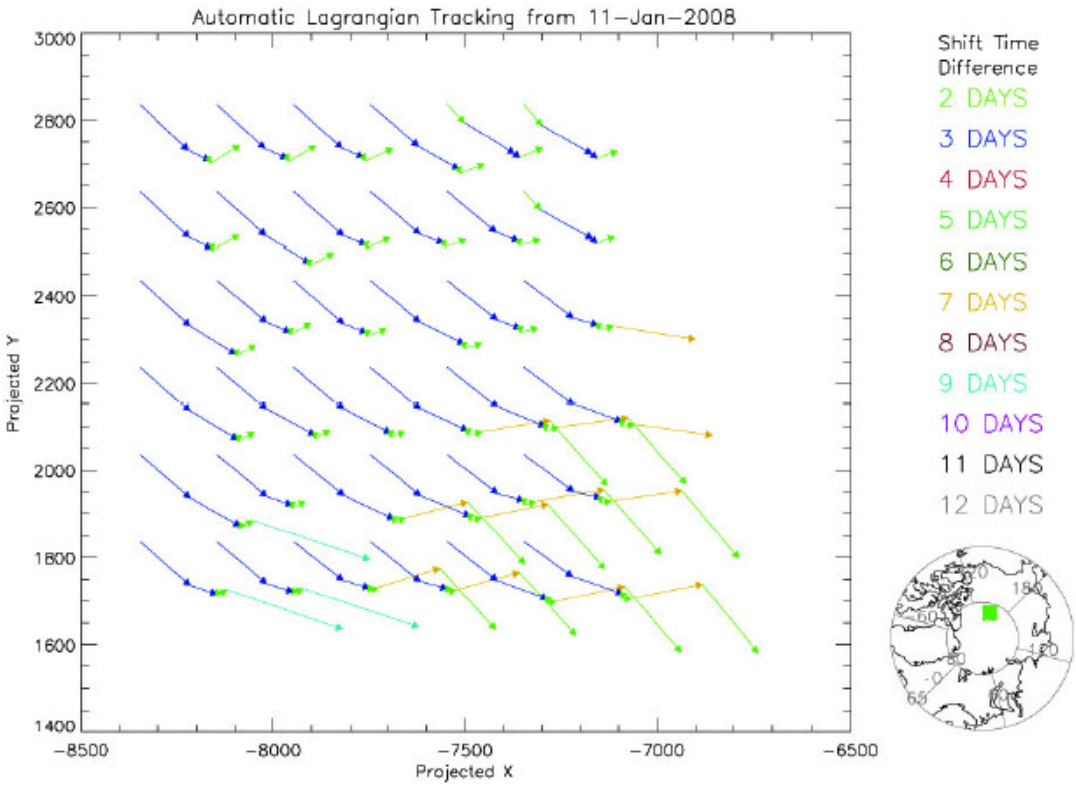

Figure 2.26. Lagrangian ice motion product from GlobICE system. Imagery used to derive ice motion information retrieved from Envisat ASAR. Retrieved from: www.globice.info/Section.php?pid=26

Past efforts into deriving ice motion estimates include analyzing sequential image pairs of comparable spatial and spectral characteristics to extract displacement vectors at varying spatial resolutions. Two computational systems for accomplishing this include the RADARSAT Geophysical Processor System (RGPS) described in Kwok (1998) and the Canadian Ice Service Automated Sea Ice Tracking System (CIS-ASITS) described in Komarov and Barber (2012) and Wohlleben et al. (2013). CIS-ASITS was used in this study, and is described further in section 2.3.1.1. These systems allow determination of displacement for identifiable ice parcels between image pairs and through further analysis can produce an estimate of the overall drift characteristics in the regions covered by overlapping images.

2.3.1.1. Canadian Ice Service – Automated Sea Ice Tracking System (CIS-ASITS)

The CIS-ASITS approach to estimating sea ice motion fields makes use of phase-correlation and cross-correlation techniques to produce a set of robust sea ice displacement vectors from co- and cross-polarised RADARSAT image swaths. The applicability of using either co-polarised or cross-polarised channels in CIS-ASITS processing has been shown to be dependent on spectral and spatial conditions within image pairs (Figure 2.27), thus both types are used in an effort to take advantage of each channel's individual strengths. Phase-correlation image registration using the Fast Fourier Transform (FFT) method can efficiently derive the translational and rotational components of ice motion from sequential SAR image pairs (Komarov and Barber, 2014). Multi-resolution pyramiding for each input swath of an image pair is performed during analysis to produce a series of resampled sub-images at low to high spatial resolution. Beginning at the lowest resolution, a baseline set of vector displacements are established before being progressively refined as analysis proceeds to higher resolution layers. Since the phase correlation does not provide an adequate measure of the similarity between two sub-images, multiple cross-correlation coefficients calculated between the sub-image from the first image swath and several possible matching sub-images from the second swath are used to identify the best-matched vector displacements. Each successive pass of analysis is followed by error filtering which is applied through forward and backward vector comparison between sub-images, discarding vectors where the sum in forward and backward displacement exceeds a predefined quantity. Cross-correlation is also applied by producing coefficients for determining a level of confidence associated with

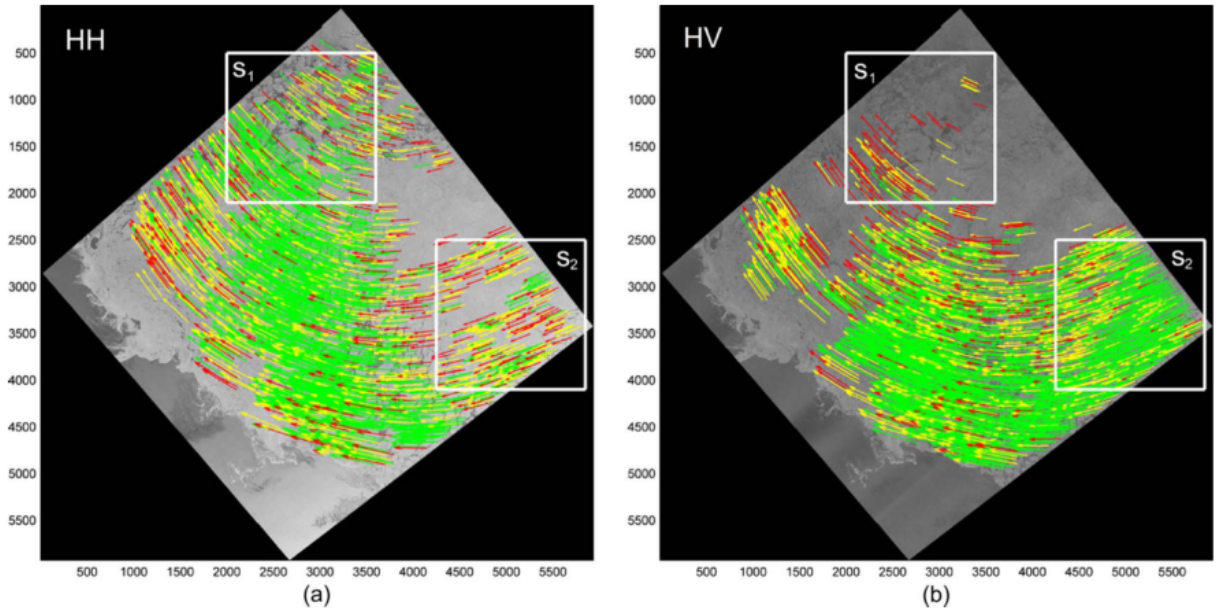

Figure 2.27. Ice motion tracking results from HH (a) and HV (b) channels. Two sequential images were taken on October 16, 2009, 15:59 and October 19, 2009, 16:12 over the southern Beaufort Sea. Vectors are plotted on the first SAR image. Green: high level of confidence, yellow: medium level of confidence, red: low level of confidence. For the image subset S_1 a larger number of ice motion vectors were derived from the HH channel compared to the HV one, while for S_2 more ice motion vectors were derived from the HV channel compared to the HH one. Source: (Komarov and Barber, 2012)

each displacement vector related to the spatial resolution of the sub-image it was derived from. Results of the CIS-ASITS approach consist of a set of displacement vectors with calculated confidence values similar to those shown in Figure 2.27. In previous studies, the results of the CIS-ASITS method as compared to *in situ* buoy observations have been favourable, showing a coefficient of determination (R^2) of 0.998 with associated Root-Mean-Square Error (RMSE) of 0.428 km (Komarov and Barber, 2014).

2.3.1.2. Combining Satellite-Derived Ice Motion Estimates with Observational Data

Further progression of detecting changes in ice drift include derived ice motion information being augmented with *a priori* drift estimates and model simulations to produce a more robust ice motion dataset (Kwok, 2010). These methods have been proven to be reliable in studies where variation in displacement and rotation is small, but with larger ranges of variation these methods seem to lose some of their ability to produce optimal results (Kwok, 2010). For example, the AVHRR Polar Pathfinder ice motion product combines passive microwave satellite remote sensing data with floating buoy observations and NCEP/NCAR vector wind data to produce a regularly-spaced grid of vectors showing displacement and direction (Figure 2.28). Degree of temporal resolution is integral to the applicability of satellite remote sensing information products due to the highly variable nature of sea ice motion. Conventional ice motion estimation methods of using overlapping image pairs are ideally purposed for areas where repeat passes of high resolution sensors occur on a regular basis (Kwok et al., 2003). This requirement presents a challenge to larger-scale studies since the availability of daily or near-daily swaths of high-resolution imagery over a large study area is not always guaranteed. Consequently, medium-to- low resolution images are typically used for Arctic-wide studies of ice motion at the cost of not capturing sea ice motion events at local scales. Systems that can produce timely, large-swath, high-resolution imagery could greatly improve the level of sea ice motion information across the Arctic.

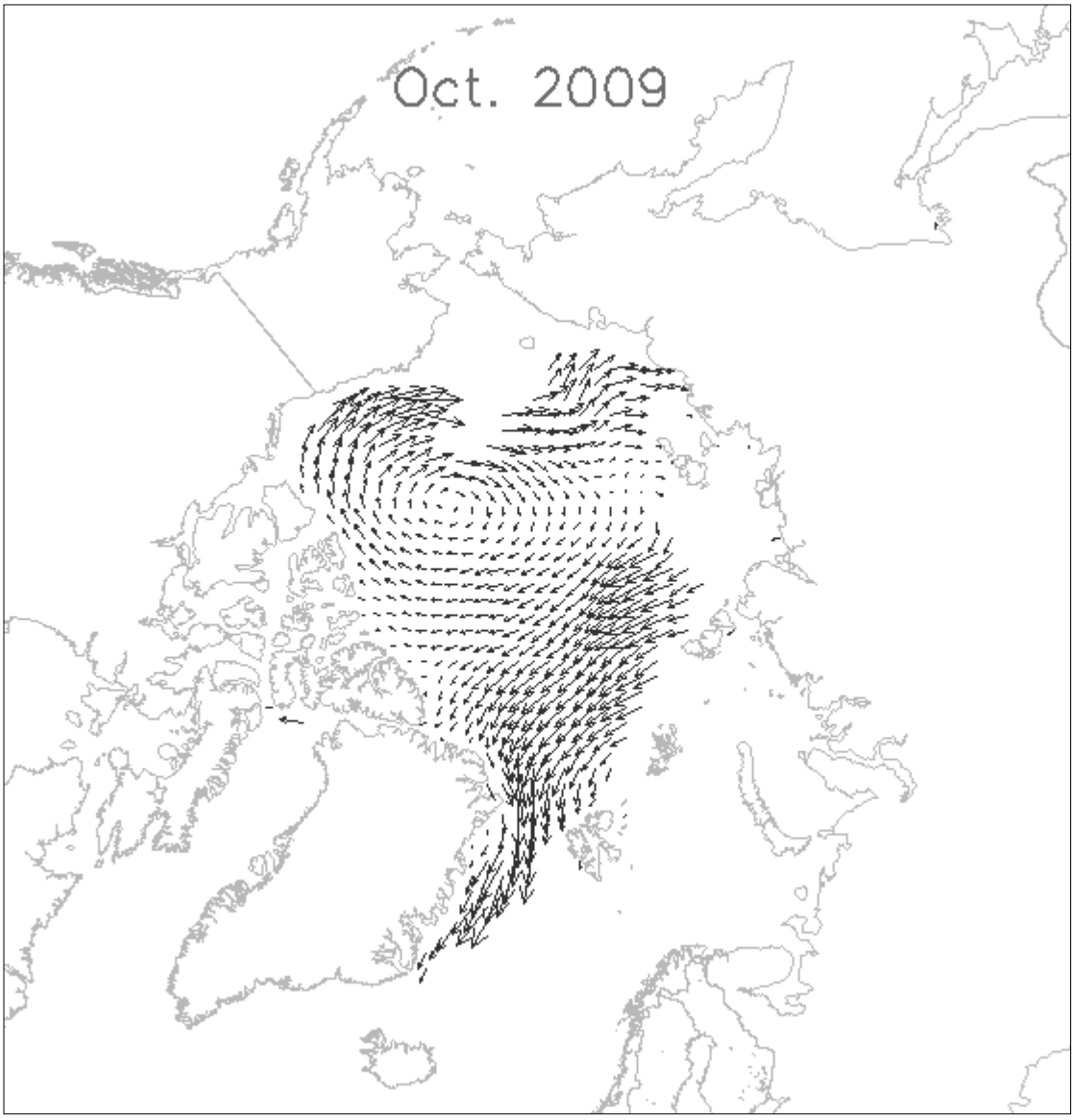

Figure 2.28. APP 25 km monthly mean ice motion product for October 2009. Every fourth grid vector is plotted. Data source: (Fowler et al., 2013)

2.4. Summary

This chapter has reviewed the literature regarding properties of Arctic sea ice and the processes which affect changes and variability in the ice cover. It has also discussed the recent trends and variability in sea ice cover for the Beaufort Sea, as well as potential drivers of these changes. Finally, microwave remote sensing of sea ice dynamics was also reviewed.

With persistent negative trends in sea ice extent and melt survivability in the Beaufort Sea (Tivy et al., 2011; Maslanik et al., 2011), it is necessary to develop further insight into recent changes in sea ice motion for this region through the most advanced active microwave satellite remote sensing platforms available. Interests in shipping navigation and natural resource extraction will also benefit from an increased understanding of ice dynamics by being better informed of the seasonal variability of ice motion in the Beaufort Sea region.

Current efforts in the development of ice motion datasets, including those generated for this study, are moving towards using high-resolution active microwave sensors such as those aboard the RADARSAT platforms. Extrapolating the near-daily coverage from these active sensors to produce climatological datasets of ice motion for use in future studies of the Arctic system is a key goal for current research (Hamidi et al., 2010; Komarov and Barber, 2014). Future projects that aim to address the satellite component of this goal include the RADARSAT Constellation (RCM) mission in development by the Canadian Space Agency (Thompson, 2010), the European Space Agency's Sentinel-1 mission of the Copernicus program (Malenovský et al., 2012), and the Deformation, Ecosystem Structure and Dynamics of Ice (DESDynI) mission proposed by NASA Jet Propulsion Laboratory (Rosen et al., 2010).

In the next chapter, a methodology for estimating monthly sea ice motion and area flux from satellite imagery is detailed, followed by the results and evaluation of these products as compared to existing methods.

Chapter 3. Data and Methods

3.1. Datasets

3.1.1. RADARSAT

RADARSAT-1 ScanSAR images over the Beaufort Sea from 1997-2007 were acquired from the Alaska Satellite Facility (ASF) User Remote Sensing Access Distributed Active Archive Center (URSA-DAAC). RADARSAT-1 has a 24-day repeat cycle with a sun-synchronous, circular, near-polar orbit transmitting and receiving horizontally polarised (HH) electromagnetic energy at a frequency of 5.3 GHz (C-band). The onboard SAR is right-looking and has 7 beam modes that image the Earth's surface at incident angles ranging from 20 to 49º off nadir. The ScanSAR Wide beam mode consists of a combination of Wide beam modes 1, 2 and 3 in addition to Standard beam modes and have a swath width of ~500 km. Table 3.1 contains a condensed summary of RADARSAT-1 characteristics.

Table 3.1. RADARSAT-1 ScanSAR Wide image data description

Active Antenna	C-Band
Frequency	5.3 GHz
Beam Mode	ScanSAR Wide
Nominal Resolution	ScanSAR Wide: 100 m
Nominal Swath Width	ScanSAR Wide: 500 km
Bit Depth	8-bit Unsigned
Polarisation	HH
Nominal Look Direction	Right
Incidence Angle	ScanSAR Wide: 20-49 degrees
Ascending/Descending Capture	Ascending at Night, Descending in Daytime
Repeat Cycle	24 days

RADARSAT-2 ScanSAR images over the Beaufort Sea from 2008-2012 were acquired from the Natural Resources Canada (NRCan) National Earth Observation Data Framework Catalog (NEODF-Cat). RADARSAT-2 has a repeat cycle of 24 days with a sun-synchronous, circular, near-polar orbit transmitting and receiving co- and cross-polarised (HH/VV, HV/VH) electromagnetic energy at a frequency of 5.405 GHz (C-band). The onboard SAR is left- and right-looking and has 11 beam modes that image the Earth's surface at incident angles of 20 to 46º off nadir. Table 3.2 shows a brief summary of the characteristics of RADARSAT-2 images used for this study.

Table 3.2. RADARSAT-2 ScanSAR Wide image data description

Active Antenna	C-Band
Frequency	5.405 GHz
Beam Mode	ScanSAR Wide
Nominal Spatial Resolution	ScanSAR Wide: 100 m*
Swath Width	ScanSAR Wide: 500 km
Bit Depth	8-bit Unsigned
Polarisation	HH
Nominal Look Direction	Left and Right
Incidence Angle	ScanSAR Wide: 20-46 degrees
Ascending/Descending Capture	Ascending at Night, Descending in Daytime
Repeat Cycle	24 days

**as acquired from Natural Resources Canada*

All RADARSAT-1 and RADARSAT-2 ScanSAR Wide swaths were resampled to 200 m spatial resolution. Previous studies have shown that 200 m spatial resolution was ideal for optimizing the process of ice object tracking via SAR image pairs without sacrificing subsequent ice motion vector quality or density (e.g. Wohlleben et al., 2013).

3.1.2. Sea Ice Concentration

Sea ice concentration, type and area data for the Beaufort Sea region (Figure 3.1) were obtained from the Canadian Ice Service Digital Archive (CISDA) for the 1997-2012 time period. These weekly ice charts are produced using multiple input data including satellite imagery, weather and oceanographic information, aircraft and ship observations, and expert analysis (Canadian Ice Service, 2005). The CISDA contains a technological bias (attributed to changes in source data and shifts in regional focus), although Tivy et al. (2011) report that there is no evidence of time-varying bias in data records following 1979. Since this study concerns CISDA datasets from between 1997-2012, the effects of the aforementioned bias are negligible. The CISDA datasets are considered more accurate than passive microwave estimates of sea ice concentration which suffer from underestimation during the melt season (Agnew and Howell, 2003).

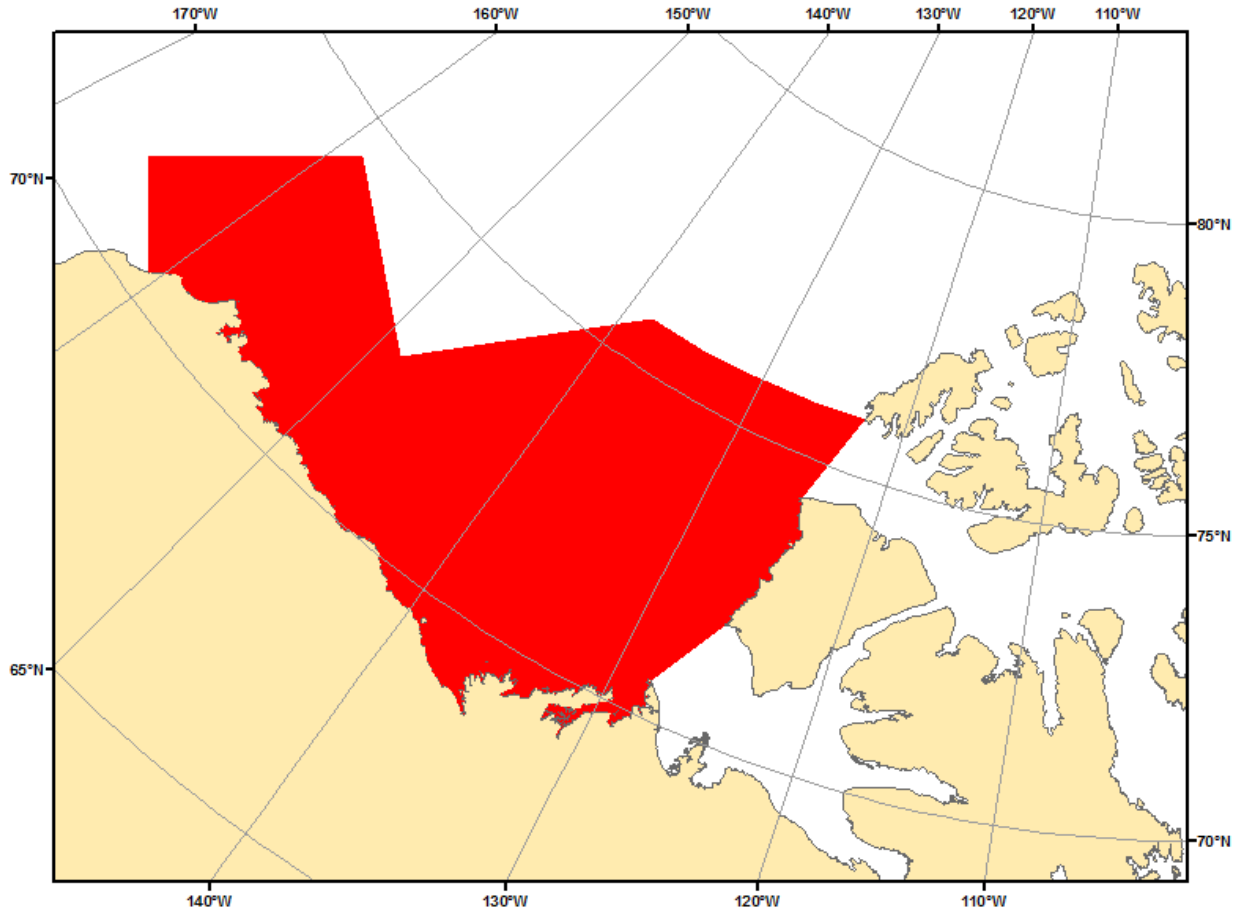

Figure 3.1. Boundaries of 1968-2012 CIS ice extent archive for the Beaufort Sea region.

3.1.3. NCEP/NCAR Reanalysis Sea Level Pressure

Mean SLP anomaly data from 1997 to 2012 were acquired from National Oceanic and Atmospheric Administration's (NOAA) Earth System Research Laboratory's Physical Sciences Division (ESRL-PSD). Produced during the 40-year reanalysis project described in (Kalnay et al., 1996), the National Centers for Environmental Protection/National Center for Atmospheric Research (NCEP/NCAR) SLP data is a subset of the continually-updated inventory provided by

NOAA ESRL-PSD. The reanalysis dataset assimilates multiple observational and model-based datasets to produce weather and climate-related variables useful for driving model studies.

3.1.4. APP-x Surface Parameters

Monthly average surface air temperature (SAT), incoming shortwave radiation at the surface (F ↓), and broadband albedo (α) datasets were acquired from the Extended AVHRR Polar Pathfinder (APP-x) dataset through NOAA covering 1997-2012. The APP-x dataset is an extension of the APP project (Fowler et al., 2000) and offers a variety of surface, cloud and radiation parameters over the Arctic at a 25 km spatial resolution. The parameters are retrieved using the Cloud and Surface Parameter Retrieval (CASPR) system, described in Key et al. (2001) and Key (2002b). Radiative fluxes are calculated in CASPR using FluxNet (Key and Schweiger, 1998), which is a neural network version of the radiation transfer model Streamer (Key, 2002a). Streamer uses NCEP/NCAR reanalysis data (Kalnay et al., 1996) for atmospheric profiles of temperature and humidity. The data has been validated with *in situ* data from the Surface Heat Budget of the Arctic Ocean (SHEBA) field experiment (Maslanik et al., 2001) and used to asses trends and spatio-temporal variability in the aforementioned parameters for Arctic regions (Wang and Key, 2003; Wang and Key, 2005). Error estimates for SAT, F↓ and α are 1.98 K, 34.4 W m^{-2}, and 0.10, respectively (Wang and Key, 2005). Total absorbed solar radiation (Q_{total}) was calculated for May through September from APP-x F↓ and α using the following equation:

$$Q_{total} = \sum_{i=5}^{9} (1 - \alpha_i) F\downarrow_i \tag{3.1}$$

where i corresponds to the month (i.e. 5 = May, 6 = June, …, 9 = September).

3.1.5. IABP Sea Ice Motion

Twice-daily interpolated ice velocity data were acquired for between 1997 and 2011 from the International Arctic Buoy Programme (IABP) via the Polar Science Center (PSC) at the University of Washington's Applied Physics Laboratory (APL-UW). These data are processed to a 2º latitude by 10º longitude circumpolar (70N to 90N) grid from the network of ~25 drifting buoys which record position and ice velocity as well as atmospheric pressure and temperature. Positional errors for the IABP buoy network are estimated to be less than 100 m for the GPS-equipped buoys, and less than 300 m for buoys which operate using the Argos system (Rigor, 2002). The acquired IABP buoy data were used to produce monthly mean ice velocities for the purpose of comparing with the results of the CIS-ASITS procedure used in this study.

3.1.6. APP Sea Ice Motion

Monthly sea ice motion vectors were acquired from the AVHRR Polar Pathfinder (APP) dataset from 1997-2012 via the National Snow and Ice Data Center (NSIDC). This dataset was created through producing monthly mean 25 km Equal Area Scalable Earth (EASE) grids of daily ice motion which was generated by interpolating SMMR, SSM/I-SSMIS and AMSR-E passive microwave remote sensing products, AVHRR visible-to-infrared remote sensing, IABP buoy observations, and NCEP/NCAR reanalysis data. Further details of the APP monthly ice motion fields are described in Fowler et al. (2013). Estimates of RMSE were produced for several years of daily ice motion vectors that did not use the IABP buoy data for interpolation. When compared with the IABP buoy vectors, these RMSE estimates were shown to be 2.91 km day^{-1} for the u

(zonal) component and 2.94 km day^{-1} for the v (meridional) component of the APP interpolated ice motion vectors (Fowler et al., 2013).

3.1.7. PIOMAS Sea Ice Motion

Simulated sea ice motion vectors were retrieved from the Pan-Arctic Ice-Ocean Modeling and Assimilation System (PIOMAS) dataset from 1997-2012 via PSC at APL-UW. PIOMAS parameters are gridded in 25 km intervals using a Generalized Curvilinear Coordinate System (GCCS) with the origin adjusted to be over Greenland. The ice motion component of the PIOMAS model is described in Zhang and Hibler (1997), while further information on the details of the model is given in Zhang and Rothrock (2001) and Zhang and Rothrock (2003). PIOMAS sea ice motion has been shown in previous studies to be able to adequately simulate variability in ice motion at a large scale (Zhang et al., 2000a), and correlates well with *in situ* buoy-based ice motion data at daily ($R = 0.80$) and annual ($R = 0.76$) time scales (Zhang et al., 2012).

3.1.8. RIPS Sea Ice Motion

The Regional Ice Prediction System (RIPS) dataset produced by Environment Canada's Canadian Meteorological Centre (CMC) assimilates a variety of modeled and observational data including CIS ice charts, CIS image analysis, and passive microwave satellite imagery to produce short-term (48 h) forecasts of sea ice concentration on a 1/12º ORCA grid. The details of this system and discussion of accuracy and validation are summarized in Buehner et al. (2013), Buehner et al. (2014) and Lemieux et al. (in press). An ice drift parameter is in development for a future version of RIPS. Ice drift is derived by solving for the 2D sea ice momentum equation in the Los Alamos sea ice model (CICE) described in Hunke and Lipscomb (2010). For comparison

with the CIS-ASITS output used in this study, RIPS monthly mean ice drift was acquired for January to December 2011.

3.2. Sea Ice Motion

Ice object identification and tracking on overlapping RADARSAT image swaths was conducted using CIS-ASITS (see section 2.3.1.1) to produce a series of ice motion vectors, which were then processed into gridded ice motion on monthly time scales from which 16-year averages of monthly ice motion were generated. The ice motion vectors were also used to establish estimates of sea ice area exchange across three predefined gates. Additional detail on these steps is contained in the following sections.

3.2.1. Ice Object Tracking via SAR Image Analysis

Sea ice motion estimates were produced by applying the CIS-ASITS procedure (section 2.3.1.1) to a large volume of RADARSAT image pairs. In an attempt to introduce optimization through parallel processing of the ice object tracking procedure, the study area was segmented into 5 sub-regions (Figure 3.2). The boundaries between these sub-regions were drawn to align with the satellite overpasses to maximize the usefulness of each individual swath. Additionally, in an attempt to retain only the most useful image swaths and further minimize the chance for sequential swaths experience zero overlap, the image inventory was filtered to remove any image where >70% of the swath's coverage was outside a given sub-region. After this filtering process, image swaths were assessed for quality and errors in preprocessing before being retained for ice tracking analysis. In all, ~30,000 RADARSAT-1 and RADARSAT-2 images (Table 3.3) were considered usable for subsequent ice motion and area exchange analysis. The filtering process occasionally

produced duplicate results where the same image pairs were used for multiple sub-regions. Thus, a duplicate removal process was added after the ice motion vector extraction process to minimize any errors associated with duplicate ice displacement vectors.

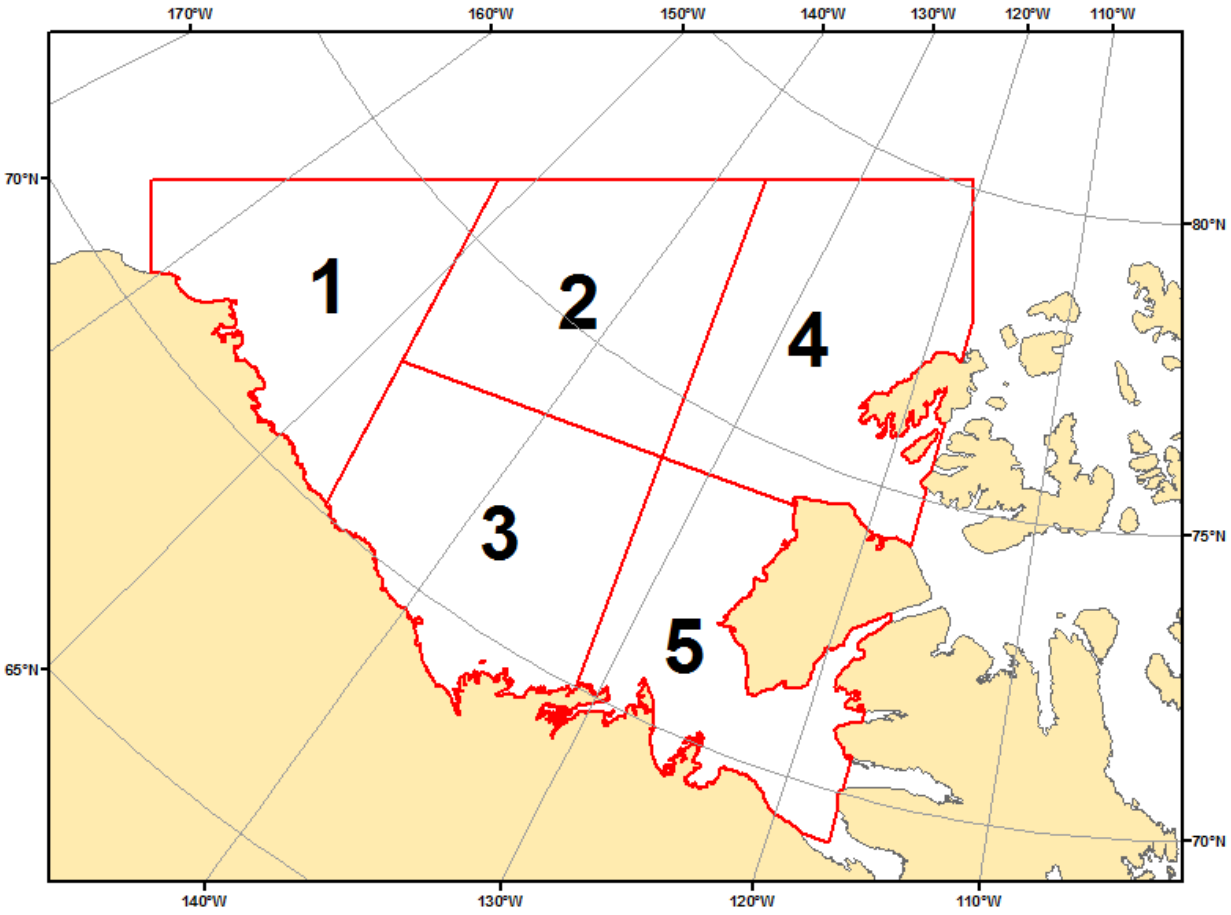

Figure 3.2. Study area boundaries split into sub-regions (1-5) for optimization of ice object tracking computational efficiency and maximization of sequential SAR image overlap.

Table 3.3. Summary of RADARSAT-1 & RADARSAT-2 ScanSAR image swaths used for CIS-ASITS processing (Imagery acquired from ASF URSA-DAAC/NRCan NEODF-Cat).

	Jan	Feb	Mar	Apr	May	Jun	Jul	Aug	Sep	Oct	Nov	Dec	Year Total
1997	114	81	104	90	119	125	189	177	52	14	171	120	**1,356**
1998	86	124	137	129	128	141	164	171	144	151	149	137	**1,661**
1999	132	125	144	147	173	185	189	188	172	187	176	185	**2,003**
2000	187	164	139	168	164	168	188	193	204	155	143	174	**2,047**
2001	162	166	184	176	194	183	246	239	211	224	218	208	**2,411**
2002	189	174	172	159	177	180	194	243	223	192	166	47	**2,116**
2003	215	171	199	165	182	218	256	257	259	256	234	230	**2,642**
2004	234	235	246	202	212	165	234	251	238	256	228	232	**2,733**
2005	234	186	198	176	186	157	182	221	217	200	233	242	**2,432**
2006	222	180	234	212	194	180	208	214	232	255	234	239	**2,604**
2007	292	246	293	292	282	278	297	294	295	273	214	188	**3,244**
2008	142	119	129	160	11	1	10	144	83	26	58	35	**918**
2009	23	20	25	26	43	34	75	99	102	75	34	32	**588**
2010	10	12	5	46	48	39	97	181	149	110	35	31	**763**
2011	27	19	20	46	45	32	81	155	170	160	73	45	**873**
2012	73	58	63	71	54	60	78	142	152	147	101	77	**1,076**
											Total Images		**29,467**

The results of the CIS-ASITS procedure consist of tabulated ice motion vectors generated from sequential image pairs. Confidence values associated with each vector were assigned based on the cross-correlation coefficient determined within the CIS-ASITS algorithm. Output vectors were examined for erroneous and spurious estimates of ice motion before being gridded to 25 km monthly sea ice velocity datasets. The CIS-ASITS method of ice object tracking and vector extraction was chosen based on the proven applicability for analysis of sea ice dynamics (e.g. Wohlleben et al., 2013; Howell et al., 2013b), ready availability of input imagery from the same sources that make operational use of the CIS-ASITS algorithm, and pre-existing hardware configurations that were optimized for CIS-ASITS processing. For ice velocities produced as part of its procedure, the CIS-ASITS algorithm assumes an error of ~0.43 km day^{-1} (Komarov and Barber, 2014). Further discussion on the procedures and error analysis used in the development of this procedure are given in (Wohlleben et al., 2013; Komarov and Barber, 2014).

3.2.2. Ice Motion Grid Interpolation

Outputs from CIS-ASITS were used to produce monthly ice motion composites over a 1638-point grid spanning the study area with 25 km spacing (Figure 3.3). In an effort to combat spurious ice motion values having too large an effect on the gridded averages, or a lack of monthly ice motion information, input gridded data were first filtered to remove spurious or invalid values before being optimally interpolated using surrounding ice motion grid points in a fixed 50 km radius. Interpolated ice motion was then re-gridded to the same dimensions as the original 25 km spacing. Boundaries of regions known to contain greater than 1/10 total ice concentration were then used to restrict the interpolated ice motion results in order to avoid introducing erroneous ice motion estimates to areas with a lack of sea ice presence.

Long-term averages of monthly ice motion were also produced for 2 subsets of the 1997-2012 time series through an equal-weighting approach on the gridded monthly composites. The first period was all months (January to December) for 1997-2007 where SAR image inventory was extensive for the entire month range. The second subset was restricted to the months of July to October (JASO) for 1997-2012 due to reduced image availability outside the summer melt season (Table 3.3).

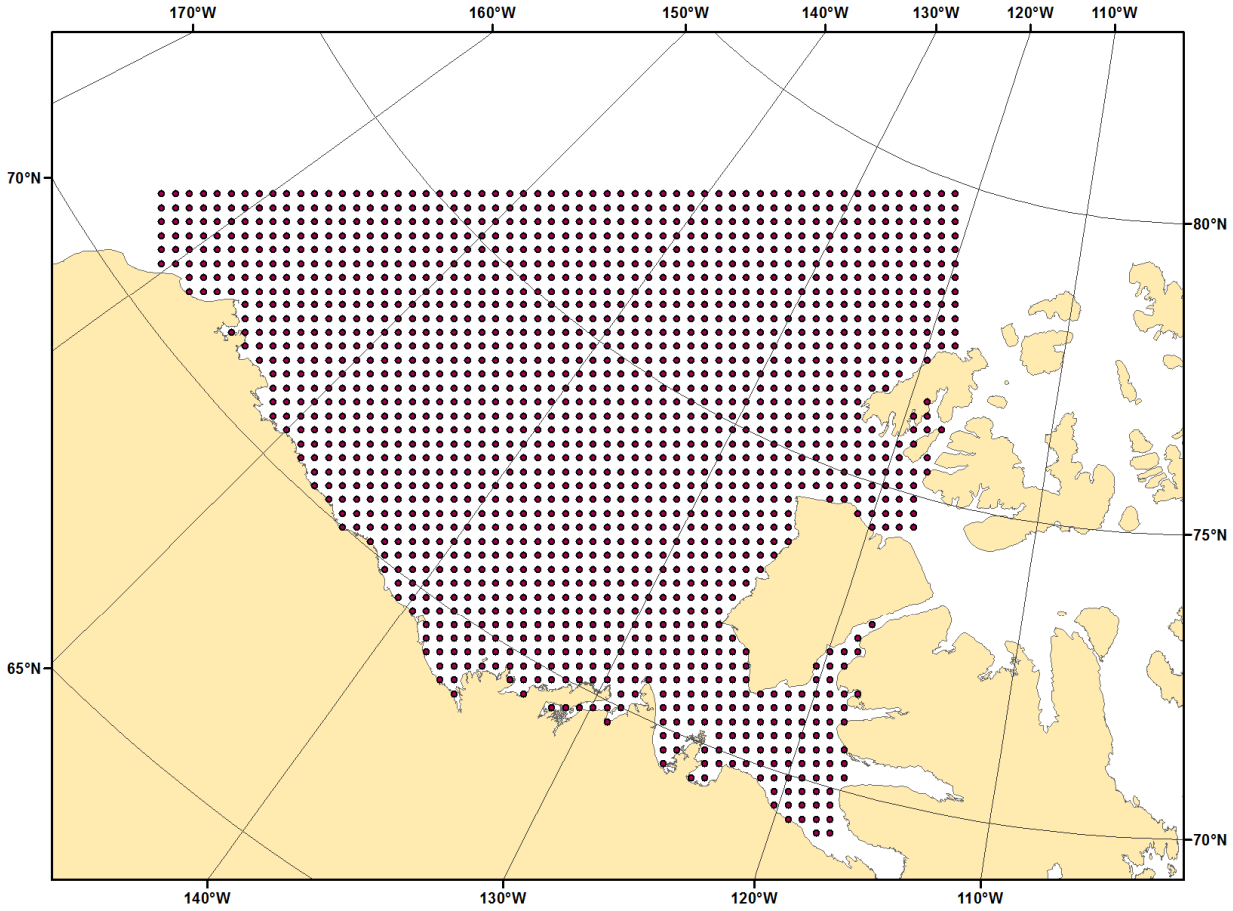

Figure 3.3. 25 km grid spacing of CIS-ASITS ice motion interpolation procedure.

3.3. Sea Ice Area Flux

Sea ice flux was estimated at three predefined exchange gates in the Beaufort Sea in order to better understand sea ice dynamics in the region. The Prince Patrick, Southeast (SE) Beaufort and Barrow gates were selected in order to provide a semi-closed system estimate on sea ice area exchange specific to the Beaufort Sea (Figure 3.4). Sea ice motion for each image pair was then interpolated to each exchange gate that includes a 30 km buffer region on each side of the gate and

sampled at 5 km intervals along the gate. From these samples, sea ice flux (F) was calculated via the following equation from (Howell et al., 2013a):

$$F = \sum c_i u_i \Delta x \tag{3.2}$$

where, c_i is the sea ice concentration retrieved from the closest CIS ice chart to the RADARSAT image acquisition time (typically within 4 days), u_i is the CIS-ASITS ice motion normal to the exchange gate, and Δx is the sampling interval along the length of the gate (5 km). Uncertainty was quantified, assuming that errors in sampling were additive, unbiased, uncorrelated and normally distributed, by applying the following equation from (Kwok and Rothrock, 1999):

$$\sigma_f = \frac{\sigma_e}{\sqrt{N_s}} L \tag{3.3}$$

where, σ_e is the associated error assumed for CIS-ASITS velocities (~0.43 km day^{-1}), L is the length of the gate in km, and N_s is the number of sampling points along the length of the gate. The estimated uncertainties of the three exchange gates under consideration are ~805.8 km^2 month^{-1}, ~890.9 km^2 month^{-1}, and ~680.3 km^2 month^{-1} for the Prince Patrick, SE Beaufort, and Barrow gates, respectively.

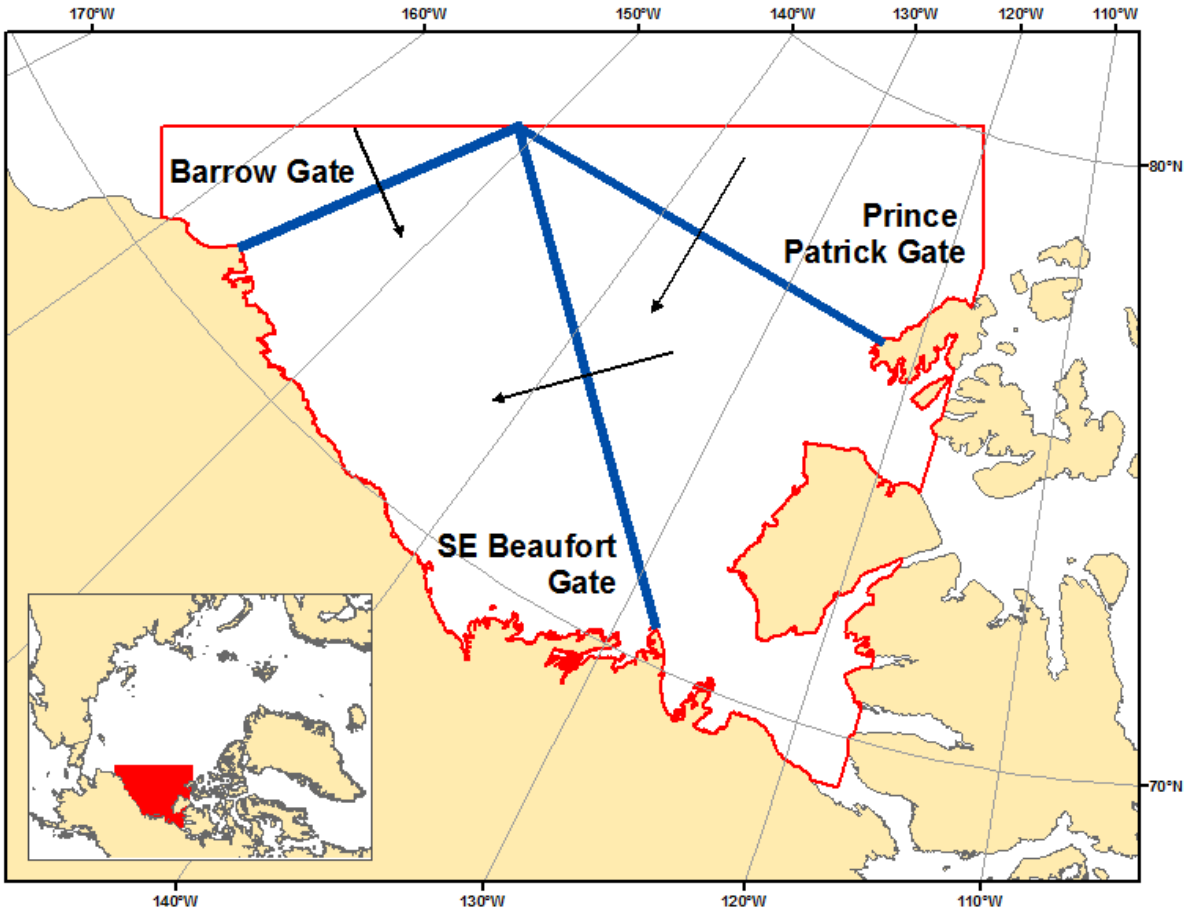

Figure 3.4. Sea ice flux gate diagram for the Prince Patrick, SE Beaufort, and Barrow gates. Positive inflow direction is shown for each gate (arrows). Study area boundaries relative to the rest of the Arctic are shown inset.

3.4. Statistical Comparisons

In determining the factors that may influence recent changes in sea ice dynamics, a series of correlation analyses were conducted between CIS-ASITS ice motion estimates and a variety of dynamic and thermodynamic surface processes. To remove the effects of shared trends, all datasets were detrended before correlation analysis was performed. Trends were calculated using the Theil-Sen approach and the Mann-Kendall test for trend was applied to the JASO time series of ice

motion and area flux based on the methods described in Zhang et al. (2000b) and Wang and Swail (2001).

Chapter 4. Results and Discussion

Objective i) Estimate monthly sea ice motion for the Beaufort Sea using RADARSAT from 1997-2012 and compare the results with previous methods.

4.1.1. Sea Ice Motion in the Beaufort Sea

Monthly sea ice motion was estimated for the 1997-2012 time series for summer (JASO) months and for the 1997-2007 time series for all months based on available satellite imagery. The following sections summarize and discuss these results, and provide a comparison with 4 additional independent ice motion datasets.

4.1.2. Monthly Characteristics

From July to the end of October over the period of 1997 to 2012, the highest mean ice motion occurred in October at 6.5 km day^{-1} (Table 4.1). An increase in mean ice motion begins in August and continues to rise into October (Table 4.1). The directional means of ice motion are strongly reflected in the anti-cyclonic circulation shown in August and September sea level pressure fields (Figure 4.3a, b). Although, the sea ice drift direction in September (Figure 4.1c) is somewhat more consistent with the development of low pressure anomalies shown in Figure 4.3c. Close to the Alaskan coastline, ice motion appears to flow eastward in the majority of months.

Table 4.1. Summary statistics of 1997-2012 time series.

Month	n	x_{min}	$\bar{x}$	x_{max}	σ_x
01	n/a	n/a	n/a	n/a	n/a
02	n/a	n/a	n/a	n/a	n/a
03	n/a	n/a	n/a	n/a	n/a
04	n/a	n/a	n/a	n/a	n/a
05	n/a	n/a	n/a	n/a	n/a
06	n/a	n/a	n/a	n/a	n/a
07	1312	0.0	3.5	11.2	2.6
08	1114	0.0	4.1	19.6	4.5
09	902	0.0	5.0	29.0	4.0
10	1211	0.0	6.5	17.7	3.6
11	n/a	n/a	n/a	n/a	n/a
12	n/a	n/a	n/a	n/a	n/a

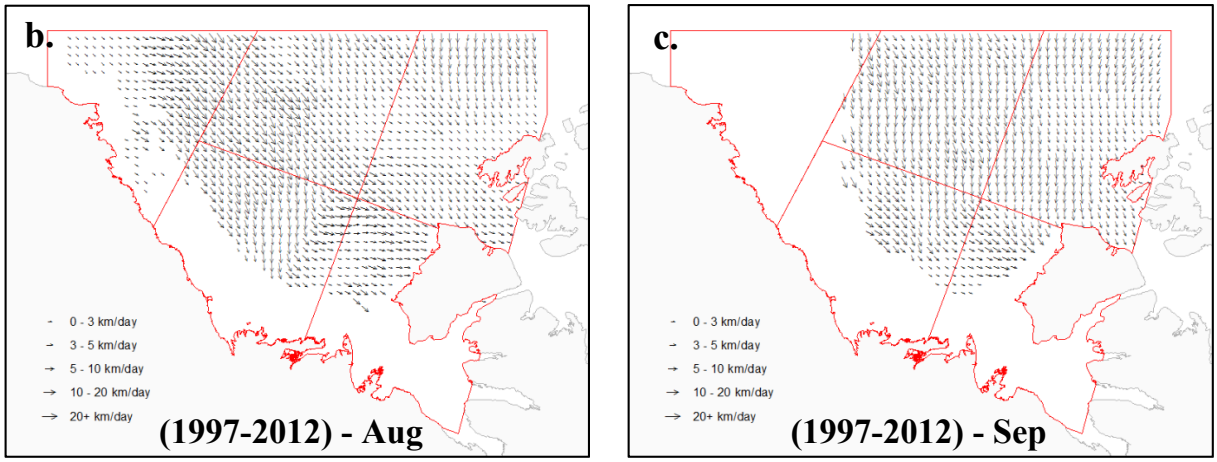

Figure 4.1. Summary statistics table for 1997-2012 monthly time series of ice motion (x) in km day^{-1} (Table 4.1), accompanied by July (a), August (b) and September (c) ice motion maps.

Table 4.2. Summary statistics of 1997-2007 time series.

Month	n	x_{min}	$\bar{x}$	x_{max}	σ_x
01	1621	0.0	3.4	7.7	2.0
02	1624	0.0	2.7	6.3	1.6
03	1625	0.0	2.0	5.0	1.4
04	1624	0.0	2.5	5.5	1.5
05	1624	0.0	3.2	7.1	1.8
06	1505	0.0	2.8	6.9	1.8
07	1418	0.0	2.7	6.4	1.7
08	1232	0.0	2.2	7.2	1.8
09	1006	0.0	4.0	11.5	2.6
10	1307	0.0	4.7	11.8	2.8
11	1612	0.0	5.0	11.3	2.7
12	1621	0.0	4.3	10.9	2.4

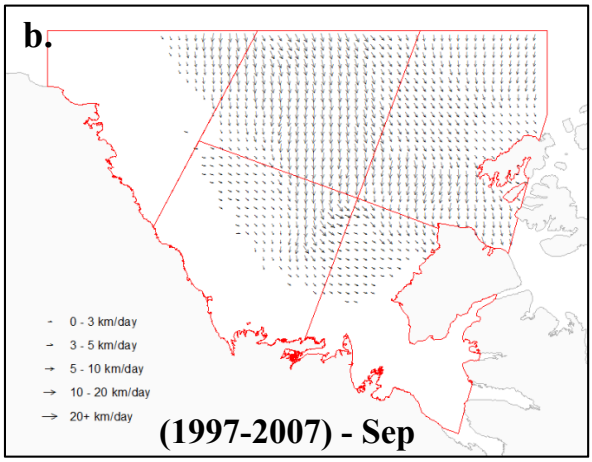

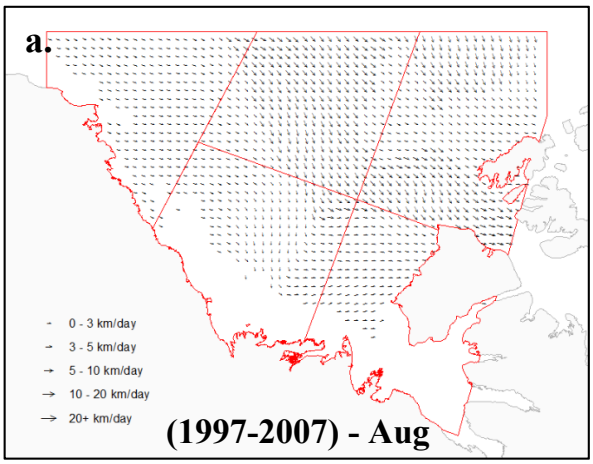

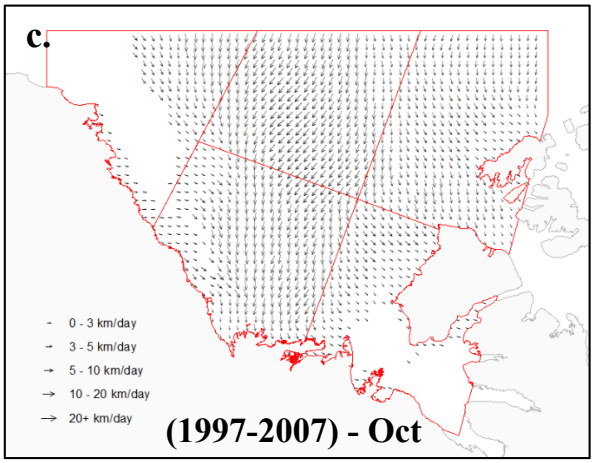

Figure 4.2. Summary statistics table for 1997-2007 monthly time series of ice motion (x) in km day^{-1} (Table 4.2), accompanied by August (a), September (b) and October (c) ice motion maps.

Mean October drift speeds during the 1997-2007 time series are nearly 30% lower than in the 1997-2012 time series (Table 4.2). The same southward mean direction of ice motion is evident in most months of the 1997-2007 average except during August where a cyclonic circulation appears to drive ice motion into the CAA via M'Clure Strait (Figure 4.2a). Spatial patterns of sea ice displacement in the 1997-2007 time series are similar to 1997-2012, although there appear to be localised areas in the 1997-2007 monthly climatologies that seem to show a more anti-cyclonic curl to ice drift. This may be the result of the shorter time series having a greater number of high-confidence ice drift estimates due to a more extensive ice cover compared to the longer time series. The direction of sea ice motion in September (Figure 4.2b) appears to follow the isobars of the negative sea level pressure anomaly shown in Figure 4.3d. October sea ice drift direction (Figure 4.2c) also appears to be aligned with the slight positive sea level pressure anomaly seen in Figure 4.3f. Since the 1997-2007 subset accounts for all 12 months of the year, the remaining months that are not represented in the 1997-2012 time series show distinct temporal variability. March mean ice drift is among the lowest of the months, and a slight increase is seen in May before incremental decreases in June, July and August (Table 4.2).

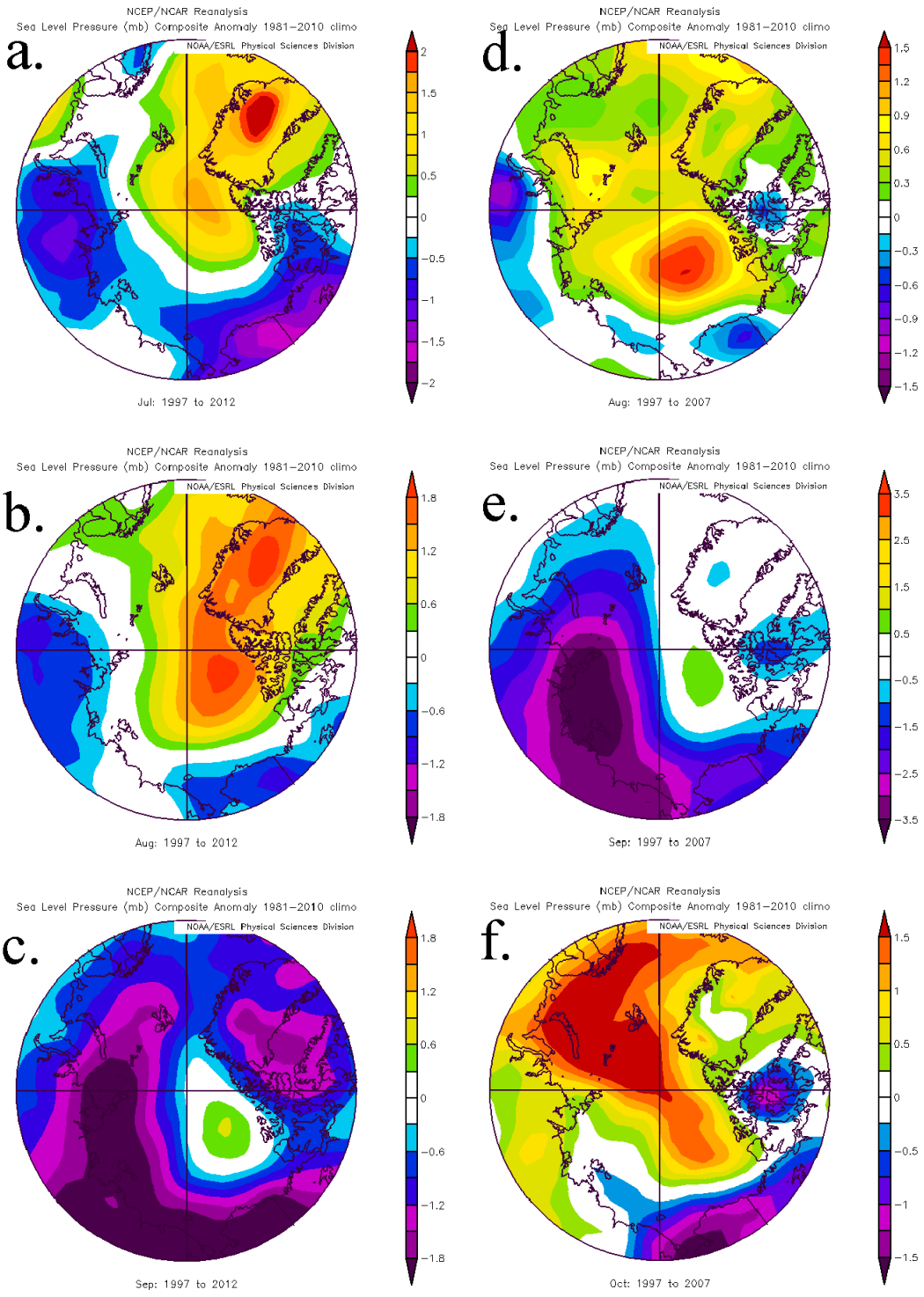

Figure 4.3. NCEP/NCAR sea level pressure anomalies for 1997-2012 (left) and 1997-2007 (right) climatologies. 1997-2012 series includes July (a), August (b) and September (c). 1997-2007 series includes August (d), September (e) and October (f). Source: NOAA ESRL-PSD

4.1.3. Comparisons with Existing Ice Motion Datasets

Results from the CIS-ASITS estimates were compared to 4 independent ice motion products to examine the relationships between alternate methodologies: the IABP interpolated ice motion product, the multiple dataset-based estimate from the APP dataset, ice drift from PIOMAS, and simulated ice motion from the RIPS model. The following sections discuss each quantitative comparison in further detail, and provide a comparison of drift vectors.

4.1.3.1. IABP Interpolated Ice Motion

From the sampled IABP interpolated dataset (Figure 4.4a), the closest CIS-ASITS results were compared on a monthly basis for the 1997-2011 time series. The comparison for July 2008 was omitted due to a lack of CIS-ASITS results for that month. Long-term average ice drift speeds for the CIS-ASITS results were 4.12 km day^{-1} (±4.10 km day^{-1}) compared to 2.25 km day^{-1} (±1.19 km day^{-1}) for the IABP grid points. The mean bias of +1.87 km day^{-1} indicated that the CIS-ASITS estimates usually favoured higher drift speeds than the IABP product. A significant (at 95% confidence interval) although weak positive correlation coefficient of 0.15 was calculated between the two datasets, indicating that little to no relationship exists between motion estimates for the two products. It is clear that the relatively small quantity and large spatial distribution of IABP buoy samples provided interpolated ice motion estimates at too coarse a spatial resolution to be adequate for comparing with high-resolution SAR-derived ice velocities. Normalized RMSE between CIS-ASITS and IABP samples was shown to be 4.49 km day^{-1}, which was higher than all other dataset comparisons. With so few monthly grid points in the IABP dataset to use in visual

comparison with results from the CIS-ASITS approach, monthly composites were not constructed for qualitative analysis.

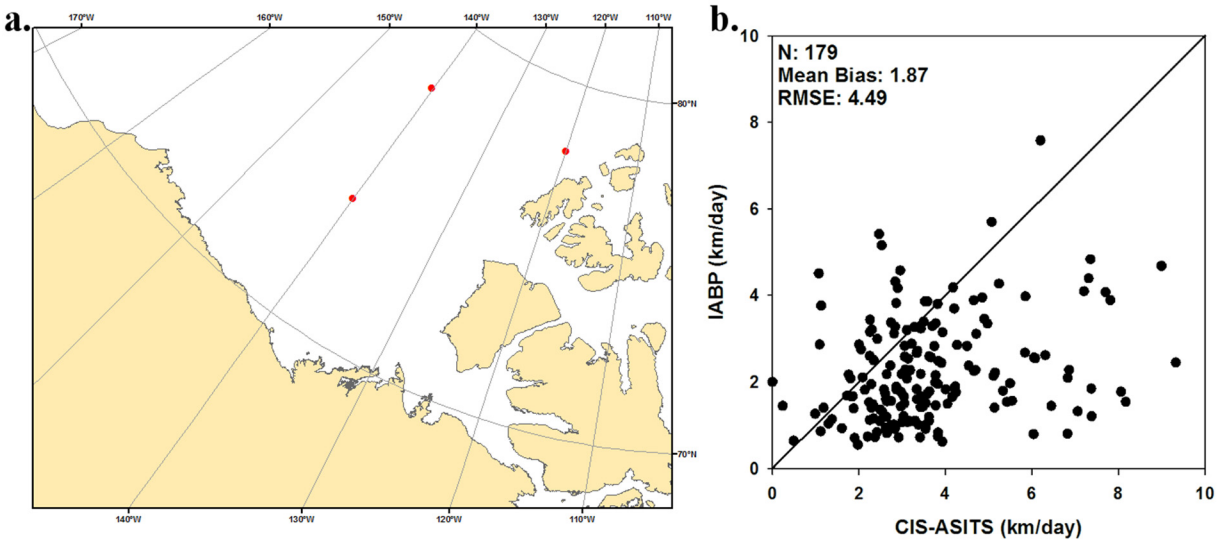

Figure 4.4. Comparison of CIS-ASITS ice motion estimates with IABP interpolated ice motion product. Location of sampled IABP interpolated data points in red (a). Comparison of CIS-ASITS monthly mean ice motion estimates to IABP mean interpolated ice motion from January to December 1997-2011 (b).

4.1.3.2. APP Gridded Ice Motion

Comparing CIS-ASITS estimates to the APP ice motion product produced a much larger sample size of points due to the relatively high resolution of the 25 km EASE-grid projection (Figure 4.5a). However, not all grid points had valid drift speed values for the APP dataset due to a lack of daily gridded source data. For the 1997-2012 time series, an average of 1,177 grid point samples were taken each month to be compared with CIS-ASITS results. Figure 4.5b shows the comparison of mean speeds from each month's combined sample points. For the entire 16-year time series, mean ice drift speed was 4.51 km day^{-1} (±2.49 km day^{-1}) and 2.91 km day^{-1} (±1.70 km

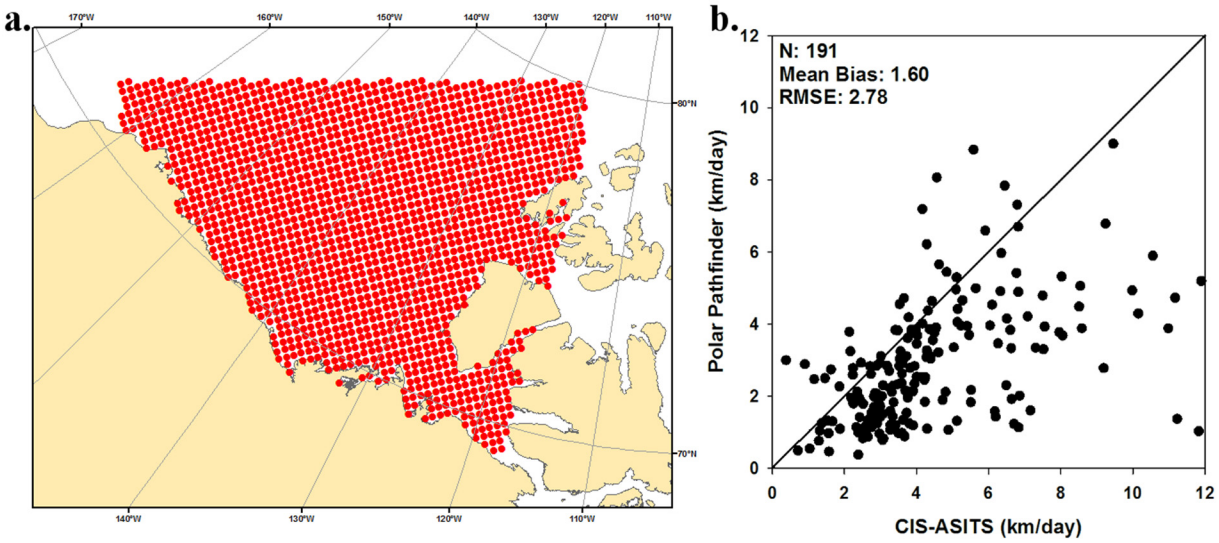

Figure 4.5. Comparison of CIS-ASITS ice motion estimates with APP ice motion product. Location of sampled APP grid points in red (a). Comparison of CIS-ASITS monthly mean ice motion estimates to APP mean ice motion from January to December 1997-2012 (b).

day^{-1}) from CIS-ASITS and APP datasets, respectively. A positive correlation coefficient of 0.46 (significant at 99% confidence interval) was calculated between the two datasets, indicating a weak-moderate relationship between CIS-ASITS estimates and the APP dataset. Similar to the IABP comparison, the CIS-ASITS sampled points generally estimated higher drift than what was found in the APP product.

4.1.3.3. PIOMAS Modeled Ice Motion

PIOMAS ice motion estimates offered valid samples for comparison with each individual CIS-ASITS estimate with an average of 1,429 samples per month. A subset of the regularly-spaced grid used for PIOMAS is shown in Figure 4.6a. Similar to previous comparisons, monthly mean ice drift speed was extracted from a given month's sampled grid points and was then plotted against CIS-ASITS results (Figure 4.6b). Mean monthly speed values for the 1997-2012 time series were

4.17 km day^{-1} (±2.51 km day^{-1}) for CIS-ASITS samples, and 3.54 km day^{-1} (±1.94 km day^{-1}) for PIOMAS samples. The mean bias of +0.63 indicated that in general, results from CIS-ASITS analysis estimated higher drift speeds relative to the PIOMAS ice motion product. A low positive correlation of 0.40 (significant at 99% confidence interval) between the CIS-ASITS estimates and PIOMAS data indicate a weak relationship between the two variables. RMSE for the CIS-ASITS and PIOMAS comparison was calculated to be 2.56 km day^{-1}, which represented the lowest RMSE of all comparisons undertaken.

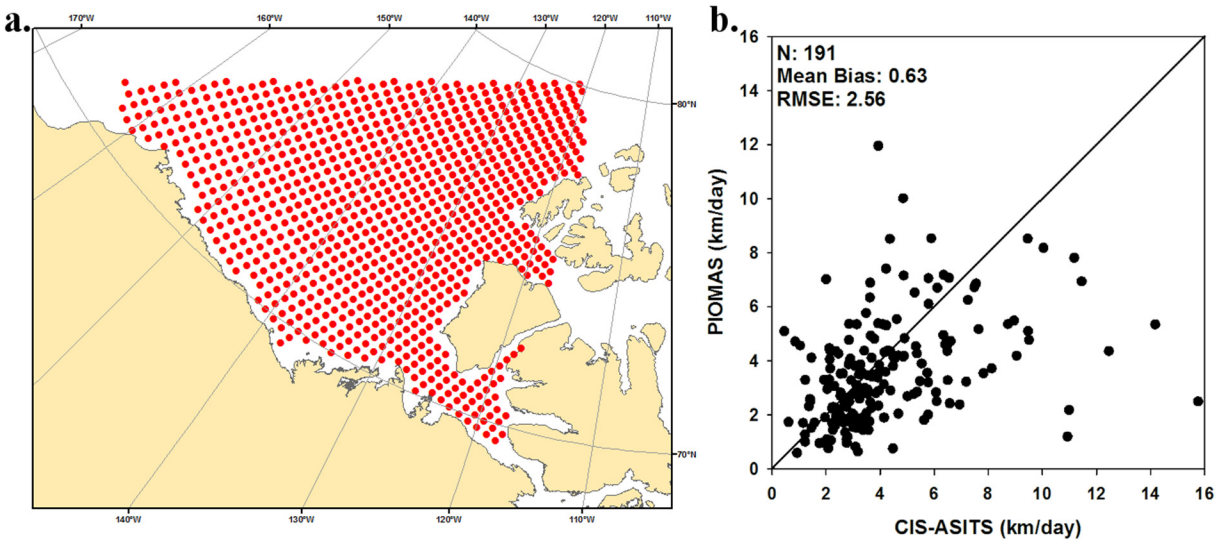

Figure 4.6. Comparison of CIS-ASITS ice motion estimates with PIOMAS modeled ice motion. Location of sampled PIOMAS model grid points in red (a). Comparison of CIS-ASITS monthly mean ice motion estimates to PIOMAS mean modeled ice motion from January to December 1997-2012 (b).

4.1.3.4. RIPS Modeled Ice Motion

The high resolution spacing of the RIPS ice drift parameter (Figure 4.7a) allowed for minimization of distance between CIS-ASITS results and the modeled ice drift parameter. Mean ice drift speed for 2011 was 5.60 km day^{-1} (±3.08 km day^{-1}) for CIS-ASITS results and 3.58 km day^{-1} (±1.24 km day^{-1}) for the RIPS modeled ice drift. Shown in Figure 4.7b, monthly CIS-ASITS estimates that were compared with RIPS ice drift exhibited a positive average bias of +2.02, indicating that the CIS-ASITS approach estimates higher mean drift speeds than the RIPS data assimilation approach. Calculated RMSE of the comparison between RIPS and CIS-ASITS ice motion was 3.11 km day^{-1} which was higher than the comparisons with APP and PIOMAS datasets but lower than with the IABP buoy observations. A moderate correlation between the CIS-ASITS and RIPS datasets of 0.65 was found to be significant at the 95% confidence interval, indicating a mild relationship between the two sets of ice drift estimates.

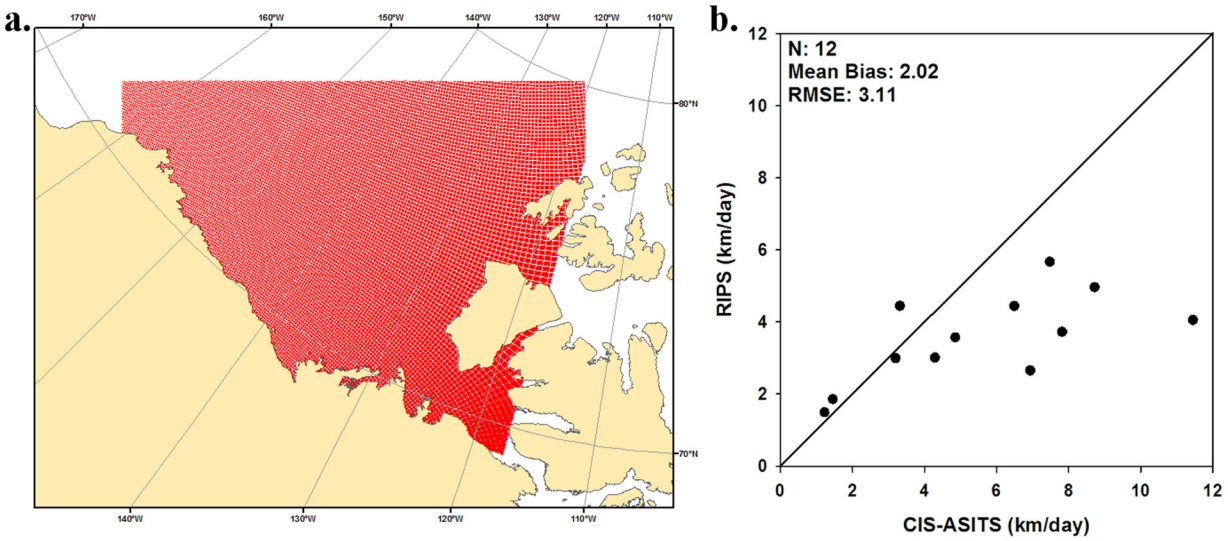

Figure 4.7. Comparison of CIS-ASITS ice motion estimates with RIPS modeled ice motion. Location of sampled RIPS model grid points in red (a). Comparison of CIS-ASITS monthly mean ice motion estimates to RIPS mean modeled ice motion from January to December 2011 (b).

The comparison for each of the independent datasets is partially contingent on how each dataset's spatial resolution relates to the CIS-ASITS monthly composites. The most favourable comparisons are expected to be made when the independent dataset has a similar original temporal period and spatial resolution as the CIS-ASITS composites (i.e. monthly mean, 25 km grid). When compared visually, the PIOMAS model output drift vectors show smooth progressions in direction and speed (Figure 4.8c, Figure 4.9c). This contrasts with the CIS-ASITS monthly composites which appear to be more affected by local-scale variability (Figure 4.8a, Figure 4.9a). Comparison of APP ice motion vectors with CIS-ASITS results (Figure 4.8a, b; Figure 4.9a, b) indicate that considerable variation exists. There were some cases where ice drift was quite similar, as evident in the October 2009 composites shown in Figure 4.8a and Figure 4.8b where good agreement is seen in terms of drift direction and speed. However, results for September 2007 (Figure 4.9a, b) indicate that there is minimal agreement in both direction and speed estimates.

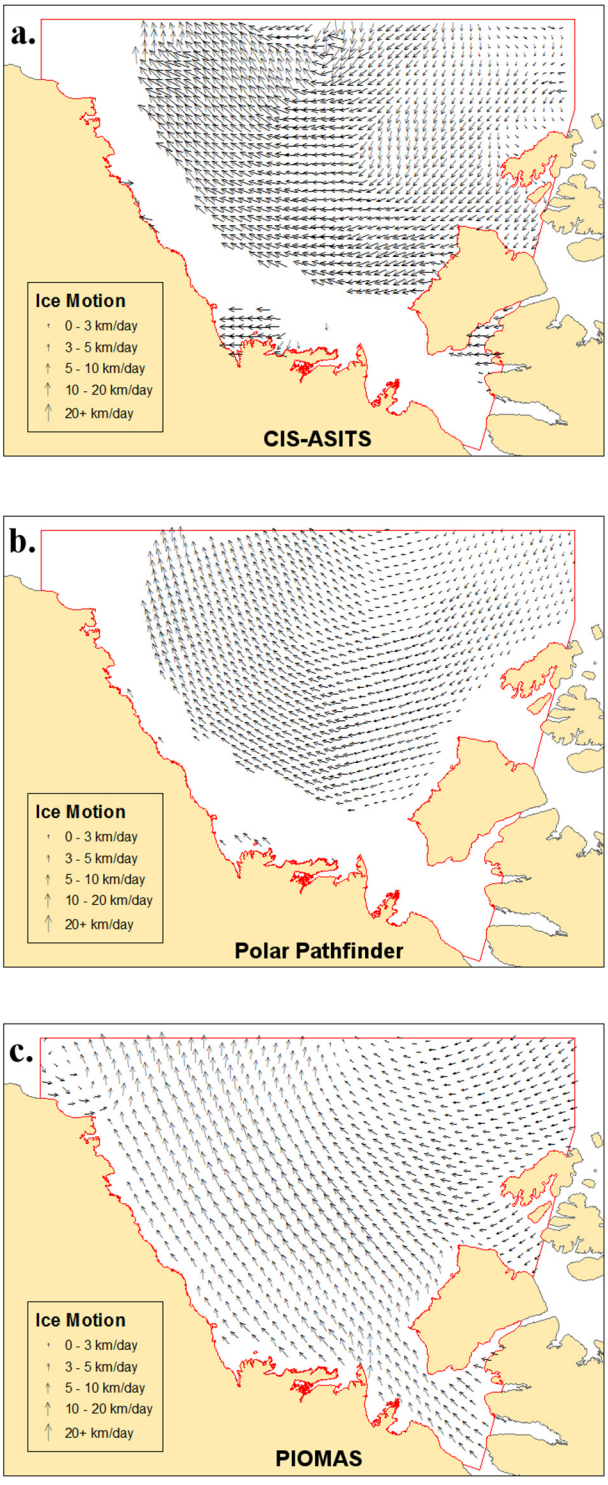

Figure 4.8. Monthly composites of gridded ice motion estimates for October 2009: CIS-ASITS (a), APP (b), and PIOMAS (c).

Figure 4.9. Monthly composites of gridded ice motion estimates for September 2007: CIS-ASITS (a), APP (b), and PIOMAS (c).

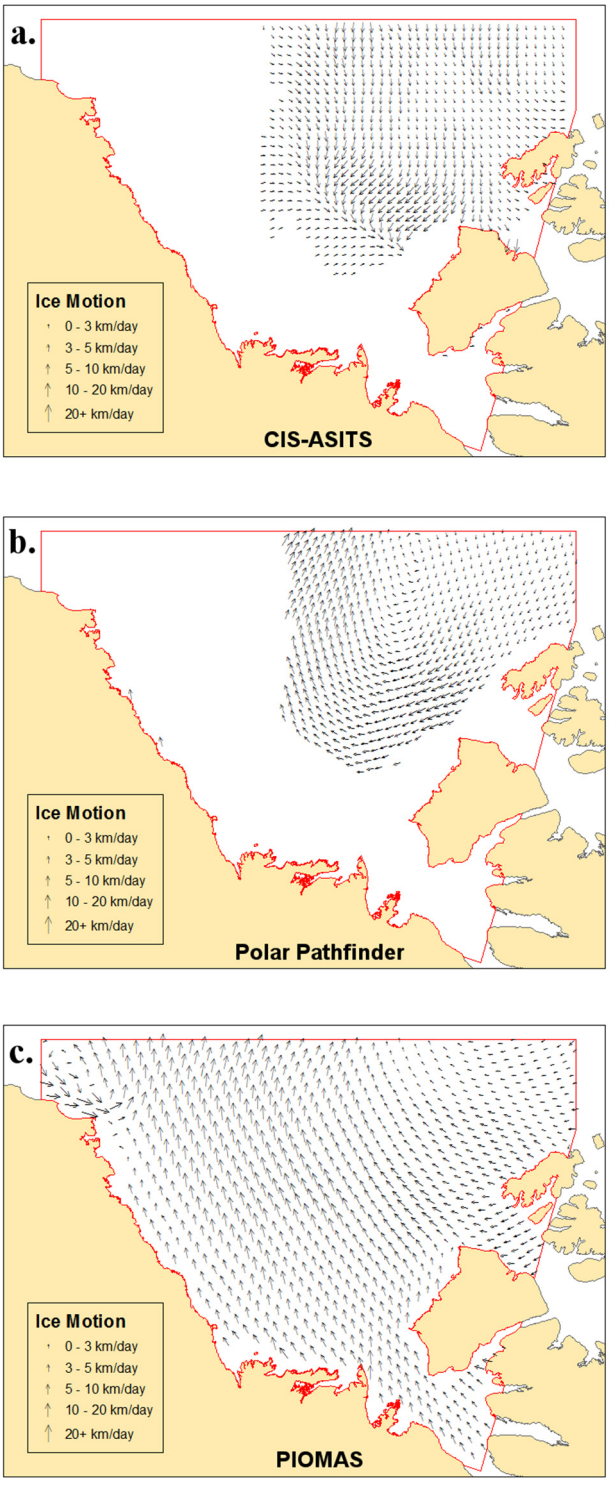

Objective ii) Estimate the sea ice area flux between the Beaufort Sea and its surrounding regions from 1997-2012.

4.2. Sea Ice Area Flux in the Beaufort Sea

Ice area exchange between the Beaufort Sea and surrounding regions was estimated for the 1997-2012 time series for the months of July to the end of October and for the 1997-2007 time series for all months using CIS-ASITS ice motion results from section 4.1.1. To determine net inflow and outflow for the Beaufort Sea, 3 gates were selected; Prince Patrick, SE Beaufort, and Barrow. In the following sections, the results of ice area exchange analysis for each date range and exchange gate are discussed. For all figures, positive flux values represent inflow relative to the Beaufort Sea and negative flux values represent outflow to surrounding waters.

4.2.1. Prince Patrick Gate

1997-2007

Ice area flux estimates for the Prince Patrick gate were positive for most months of 1997-2007, with a mean inflow of $+4.1 \times 10^4$ km^2 ($\pm 5.9 \times 10^4$ km^2) (Figure 4.10a). Monthly interannual variability in the 1997-2007 time series was lowest in May with mean net flux of $+4.6 \times 10^4$ km^2 and standard deviation of $\pm 2.9 \times 10^4$ km^2, contrasting with the highest variability in November with mean net flux of $+5.7 \times 10^4$ km^2 and standard deviation of $\pm 9.5 \times 10^4$ km^2 (Figure 4.11a). Overall, sea ice flowing into the Beaufort Sea via the Prince Patrick gate appears to be increasing slightly in the latter half of the 1997-2007 time series, especially in 2004 and 2005 where few

months experienced net outflow (Figure 4.10a). The source of this influx is primarily the Canada Basin, although a fraction may also originate from the northern straits of the CAA.

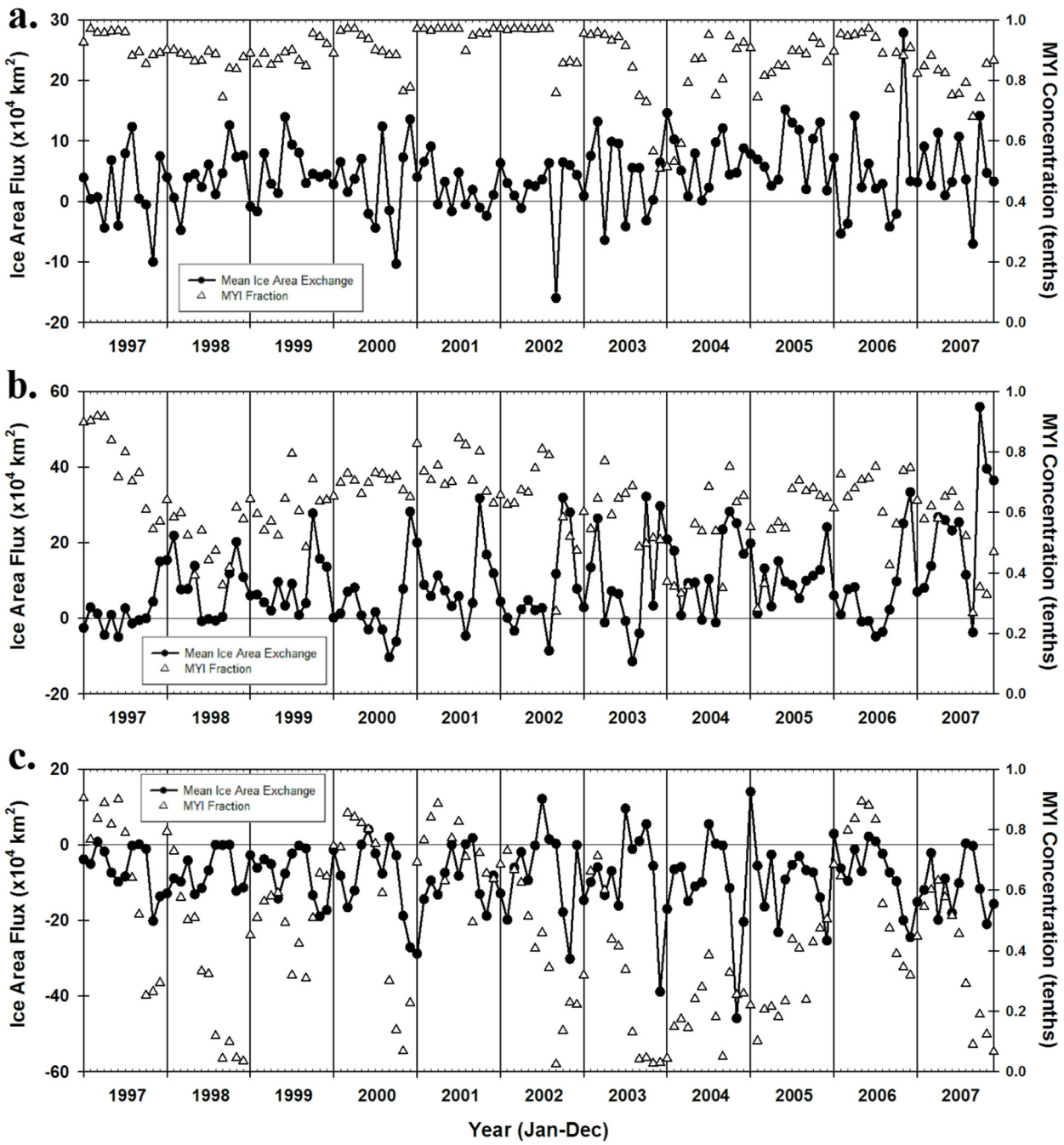

Figure 4.10. Time series of 1997-2007 intermonth mean sea ice exchange for the Prince Patrick (a), SE Beaufort (b), and Barrow (c) gates.

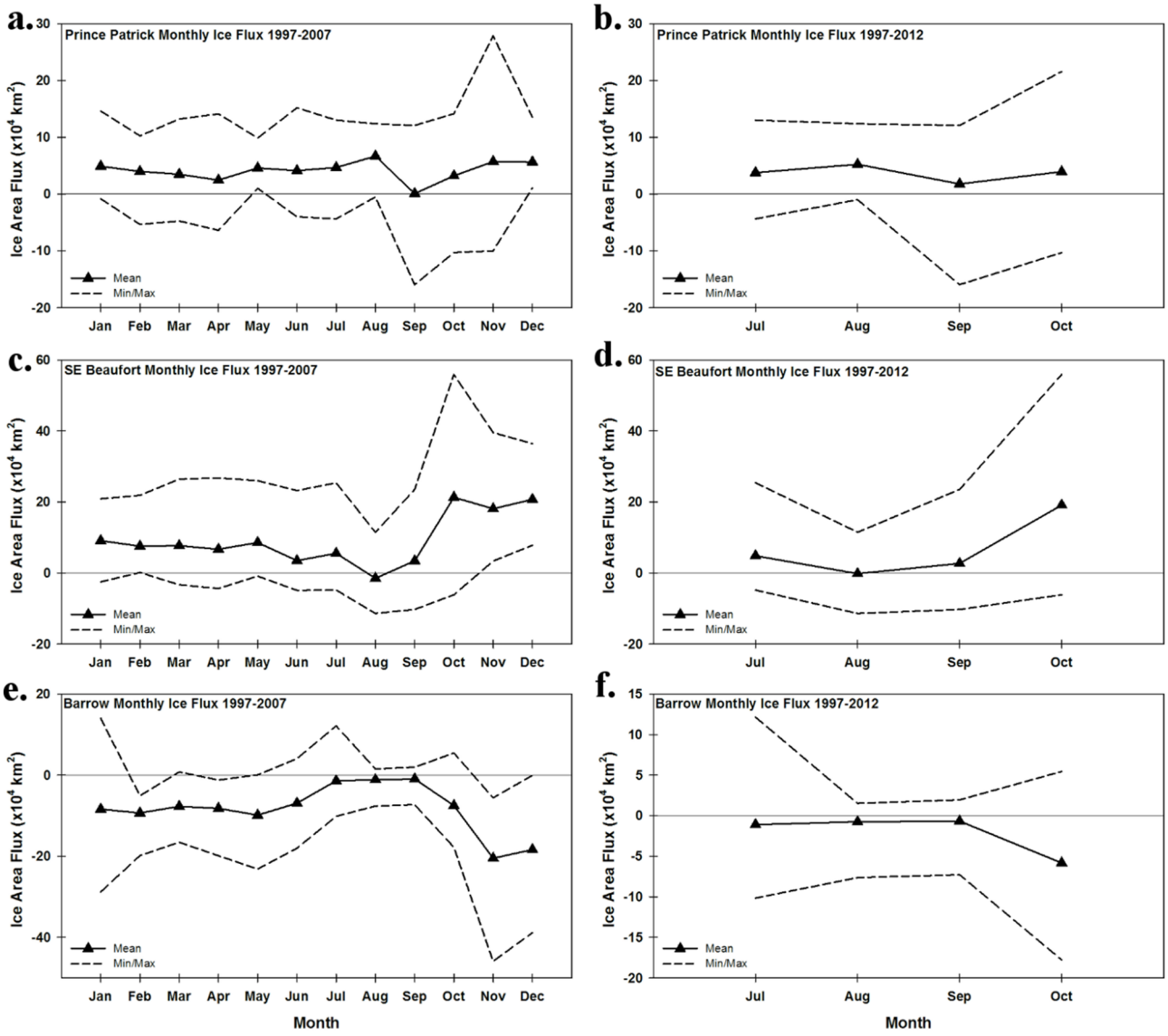

Figure 4.11. Multi-annual mean monthly net exchange for 1997-2007 January-December (left) and 1997-2012 JASO (right) time series.

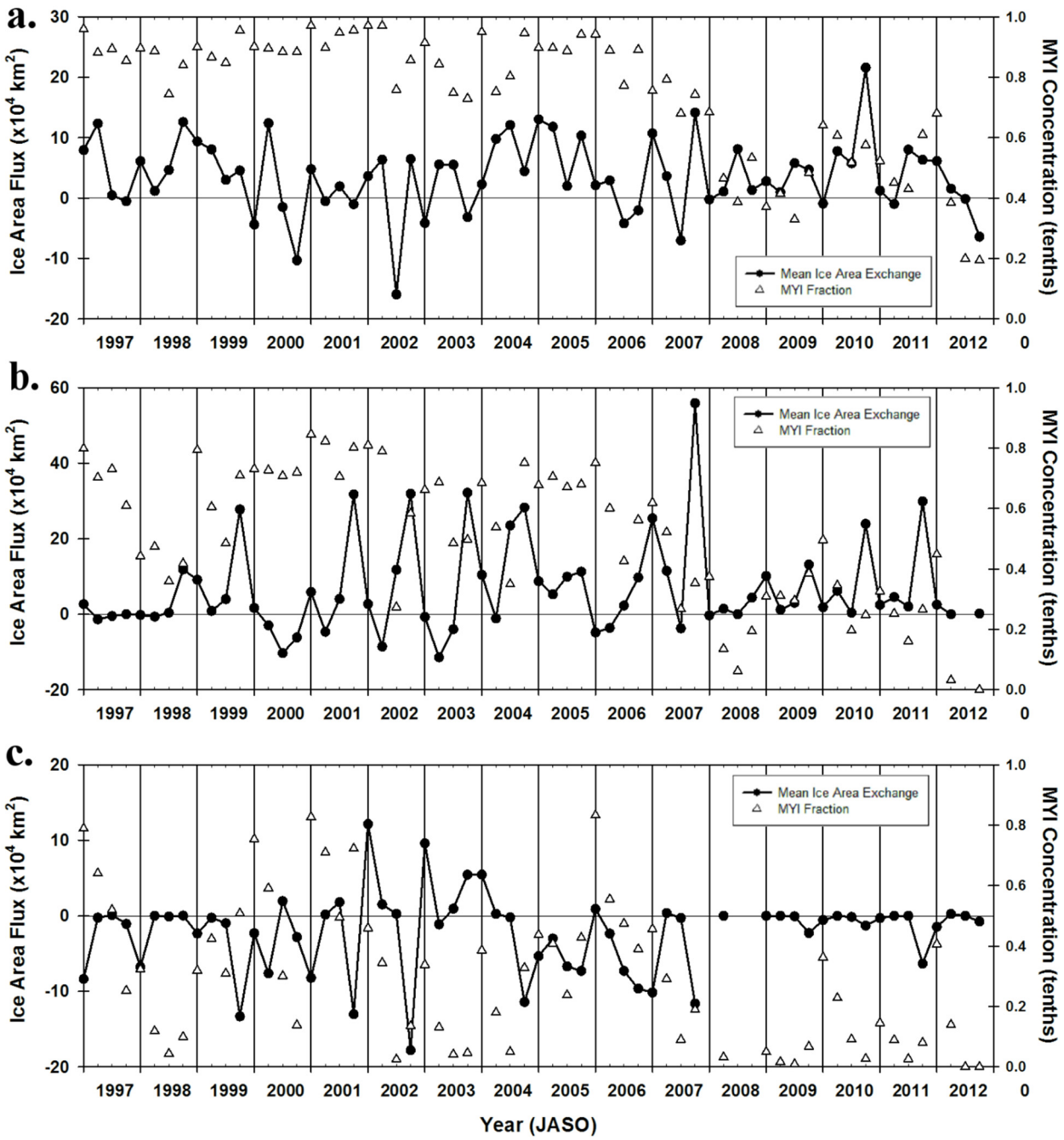

Figure 4.12. Time series of 1997-2012 intermonth mean sea ice exchange for the Prince Patrick (a), SE Beaufort (b), and Barrow (c) gates.

October experienced the highest variability with a mean net flux of +3.2 x 10^4 km^2 and standard deviation of ±7.4 x 10^4 km^2, and August was the least variable month with a mean net flux of +6.6 x 10^4 km^2 and standard deviation of ±4.6 x 10^4 km^2 (Figure 4.11a). Intermonth net exchange variability was also evident, with a net flux of -4.2 x 10^4 km^2 in September 2006 following the positive net flux of +2.9 x 10^4 km^2 seen during August (Figure 4.10a). MYI concentration remained high between 1997 and 2002 before experiencing a slight decline beginning in August 2003 and reaching a time series minimum of ~51% in December 2003 (Figure 4.10a). This decline ends in early 2004 and MYI concentration appears to recover before beginning another slight downward trend in 2007 (Figure 4.10a).

1997-2012

The 1997-2012 JASO time series of sea ice area flux for the Prince Patrick exchange gate is shown in Figure 4.12a. Variability in monthly ice exchange across the 1997-2012 time period appears to peak in October with mean monthly net flux of +3.9 x 10^4 km^2 and standard deviation of ±8.1 x 10^4 km^2 and reaches a minimum in August with mean monthly net flux of +5.2 x 10^4 km^2 and standard deviation of ±4.6 x 10^4 km^2 (Figure 4.11b). No discernable deviation from earlier years can be seen in more recent years, which would suggest that the net quantity of sea ice area transiting the Prince Patrick gate remains unchanged. However, MYI concentration begins decreasing during the 2007 season and continues to decrease in 2008 before plateauing in 2009 (Figure 4.12a). This decline is consistent with the results shown by Maslanik et al. (2011) who report a >50% decrease in September MYI extent in the Beaufort Sea between 2006 and 2008. Increases in MYI concentration appear to occur in 2010 and 2011 before dropping precipitously

in 2012. Despite the decreases in MYI concentration shown in Figure 4.12a, the net amount of sea ice crossing the Prince Patrick gate shows little evidence of significant change or trend, indicating that MYI fraction of the ice pack may not play a dominant role in regulating the exchange of sea ice between the Beaufort Sea and neighbouring regions.

4.2.2. Southeast Beaufort Gate

The SE Beaufort gate was selected in an effort to capture variability in sea ice exchange within the Beaufort Sea. On the eastern side of the SE Beaufort gate, sources of sea ice include the greater Canada Basin as well as the CAA via M'Clure Strait and Amundsen Gulf, while western sources of ice were expected to originate mostly from the Chukchi Sea.

1997-2007

Similar to the Prince Patrick gate, most of the intermonth net flux estimates across the SE Beaufort gate in the 1997-2007 time series were positive (Figure 4.10b). The only net outflow occurred during the melt season during 2000. In most years, monthly net fluxes reach peak values during autumn months. This is especially evident in October 2007, when the maximum single-month net inflow was estimated at $+55.9 \times 10^4$ km^2. The record maximum single-month net negative flux occurred in August 2003 with an estimated outflow of -11.8×10^4 km^2. Monthly average net flux across all months for the 1997-2007 period peaks in October with mean influx of $+21.3 \times 10^4$ km^2 and $\pm 17.8 \times 10^4$ km^2 standard deviation, and reaches a minimum in August with mean outflow of -1.5×10^4 km^2 and $\pm 6.2 \times 10^4$ km^2 standard deviation (Figure 4.11c). MYI fraction of net monthly ice flux appears to oscillate between ~30% and ~80% between 1997 and 2007 before reaching ~50% in December 2007 (Figure 4.10b). In terms of the changes in net total sea

ice area flux between 1997 and 2007, considerable increases are seen as the time series progresses. In 1997, net inflow was relatively low at +13.4 x 10^4 km^2 and MYI concentrations were high, whereas during 2004 and 2007 net inflow was much higher at +16.1 x 10^5 km^2 and +27.0 x 10^5 km^2, respectively, with MYI concentrations lower than earlier in the record.

1997-2012

Looking at the 1997-2012 period for JASO sea ice area exchange across the SE Beaufort gate shows a clear decline in MYI concentration similar to the Prince Patrick time series following 2007 (Figure 4.12b). The maximum inflow in October 2007 and maximum outflow in August 2003 mentioned in the previous section remain the dominant single-month peak flux estimates, which indicates that ice exchange across the SE Beaufort gate in recent years has not experienced any flux extremes.

Sea ice flux estimates for September 2012 in Figure 4.12b could not be completed with an acceptable degree of confidence owing to a lack of resolvable sea ice available to estimate motion across the SE Beaufort gate. This is likely due to the generally ice-free conditions seen during September 2012 (Figure 4.13) following the effects of cyclone activity in August 2012 (Simmonds and Rudeva, 2012). Mean monthly net flux for JASO during 1997-2012 was most variable in October with a mean influx of +19.1 x 10^4 km^2 and standard deviation of ±16.3 x 10^4 km^2 (Figure 4.11d). August was once again the month with the least amount of variability across the 16-year period with a mean negative flux of -0.2 x 10^4 km^2 and standard deviation of ±5.6 x 10^4 km^2.

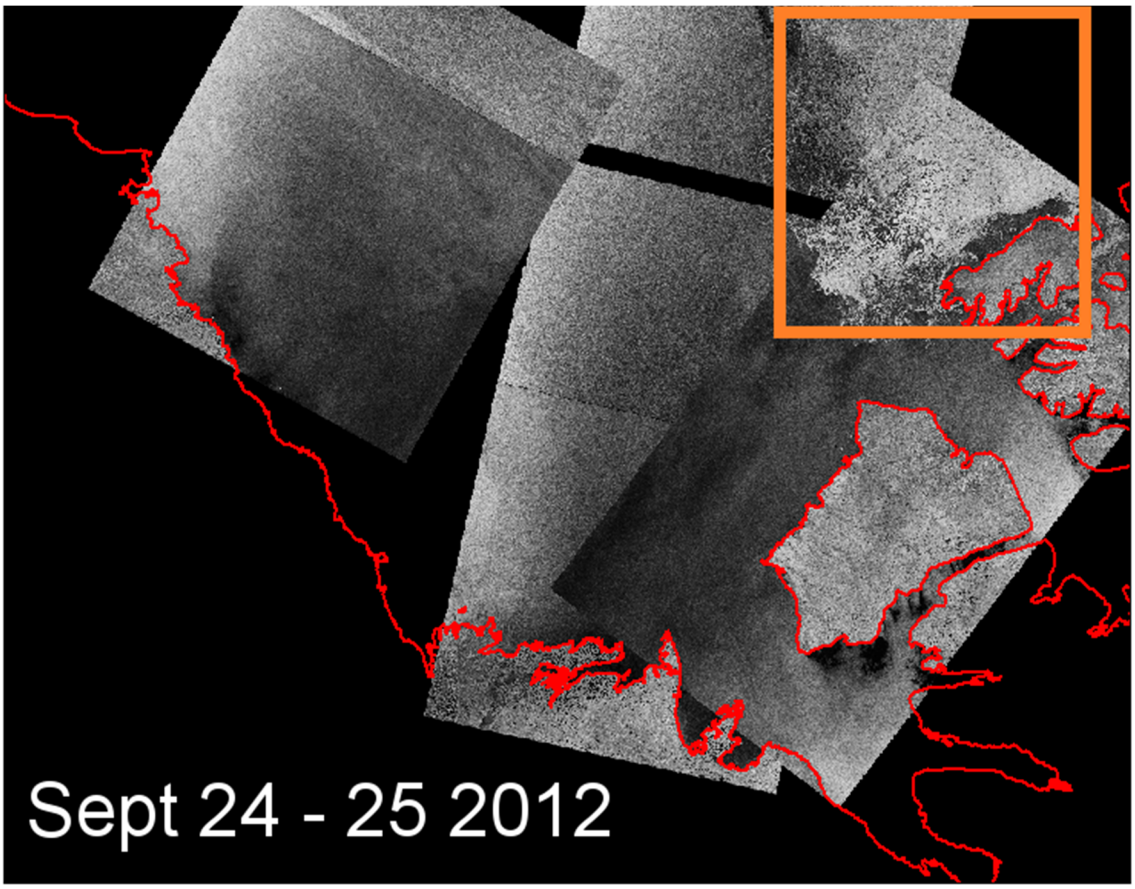

Figure 4.13. RADARSAT-2 mosaic of ScanSAR Wide images showing sea ice extent (outlined in orange) between September 24 & 25, 2012. RADARSAT-2 data © Canadian Space Agency

4.2.3. Barrow Gate

The Barrow gate was established to produce estimates of sea ice area exchange between the Beaufort Sea and the neighbouring Chukchi Sea. Positive values indicate ice crossing into the Beaufort, whereas negative results indicate an outward flow towards the Siberian region of the Arctic Ocean.

1997-2007

Between 1997 and 2007, annual net monthly exchange of sea ice area across the Beaufort gate is primarily ice transiting out of the Beaufort Sea region with occasional net positive monthly flux in spring-summer months of the early 2000s and an anomalously high positive net inflow in January 2005 (Figure 4.10c). Temporal patterns of monthly net ice flux consisted of usually low net exchange in spring-summer followed by rapid outflow in autumn and winter months. In terms of extreme single-month net flux values, November 2004 was the largest outflow with -45.9 x 10^4 km^2, with record inflow occurring in January 2005 with +14.0 x 10^4 km^2. January-December MYI concentrations for the Barrow gate during 1997-2007 oscillate between high (e.g. ~80% in January-July 1997) to very low (e.g. ~50% in September-December 2003) concentrations across the time series (Figure 4.10c). Unlike the results found with other gates, variability in multiannual means of monthly net flux was highest in January with mean exchange of -8.4 x 10^4 km^2 and standard deviation of ±11.6 x 10^4 km^2. November and December also exhibited high variability, although their mean exchanges were more than twice that of January at -20.5 x 10^4 km^2 ±10.4 x 10^4 km^2 and -18.4 x 10^4 km^2 ±10.5 x 10^4 km^2, respectively (Figure 4.11e). Variability in ice exchange was at a minimum during August with a mean outflow of -1.1 x 10^4 km^2 and standard deviation of ±2.5 x 10^4 km^2.

1997-2012

Variability in 1997-2012 mean monthly net flux between July and October was highest in July with a mean of -1.4 x 10^4 km^2 and standard deviation of ±7.6 x 10^4 km^2, just slightly more variable than October whose mean net flux was -7.5 x 10^4 km^2 ±7.0 x 10^4 km^2 (Figure 4.11f).

Similar to findings for the other gates, variability in mean monthly net flux was lowest in August with a mean net flux of -1.1 x 10^4 km^2 and standard deviation of ±2.5 x 10^4 km^2. MYI concentration of sea ice area exchange for the 1997-2012 JASO time period shows the oscillation from high to low values between 1997 and 2007 as seen previously, although in more recent years the MYI content of ice crossing the Barrow gate appears to reach minimums for sustained periods of time especially in September and October 2012 with MYI concentration at near-zero values (Figure 4.12c). In general, net fluxes for the Barrow gate in the years following 2007 are very low, but sea ice concentration does not experience much in the way of recovery to suggest that decreased ice drift speeds are fostering ice retention. This anomaly may instead indicate that there is no resolvable sea ice remaining in the western Beaufort Sea to cross the Barrow gate into neighbouring regions (discussed further in section 4.3.1).

Sea ice exchange results for the 1997-2012 time period were incomplete during July, September and October 2008 due to either a lack of resolvable sea ice in the vicinity of the Beaufort gate, or a lower than normal SAR image inventory for those months. This high net outflow in October 2002 was also the interannual single-month extreme net outflow for the 1997-2012 JASO time series at -17.8 x 10^4 km^2 while extreme net monthly inflow occurred in July 2002 with +12.1 x 10^4 km^2 (Figure 4.12c).

Objective iii) Using the results from i) and ii), explore the drivers of recent variability in sea ice dynamics within the Beaufort Sea

4.3. Trends and Variability of Sea Ice in the Beaufort Sea: 1997-2012

Sections 4.1.1 and 4.2 discuss the changes in sea ice motion and area flux over the 1997-2012 time series. For the 1997-2012 period, JASO mean ice drift speed ranged from 0.35 km day^{-1} in July to 0.65 km day^{-1} in October. Ice area exchange showed a dramatic decline in net export at the Barrow gate, with no sustained deviation from normal variability shown at the remaining gates. The following sections discuss possible drivers of recent variability in sea ice dynamics in the Beaufort Sea.

4.3.1. Sea Ice Area and Concentration in the Beaufort Sea

The monthly time series of total ice and MYI in the Beaufort Sea derived from CISDA ice charts is shown in Figure 4.14. Maximum sea ice coverage of approximately 5.7 x 10^5 km^2 in the Beaufort Sea occurs in December, and retreat begins in the early spring during May or June with some interannual variability (Figure 4.14). September is the month when sea ice in the Beaufort Sea reaches its minimum extent, with the notable exception of 2008 when August experienced the record annual minimum of 8.2 x 10^4 km^2. Extreme sea ice area minima are evident in 1998, 2007, 2008, 2010, 2011 and 2012. MYI area appears to account for the majority of remaining summer sea ice area, indicating a strong resiliency of MYI to ice area loss. However, in years following 2007, MYI recovery peaked at just over 2.3 x 10^5 km^2 before a precipitous drop in area during summer 2012.

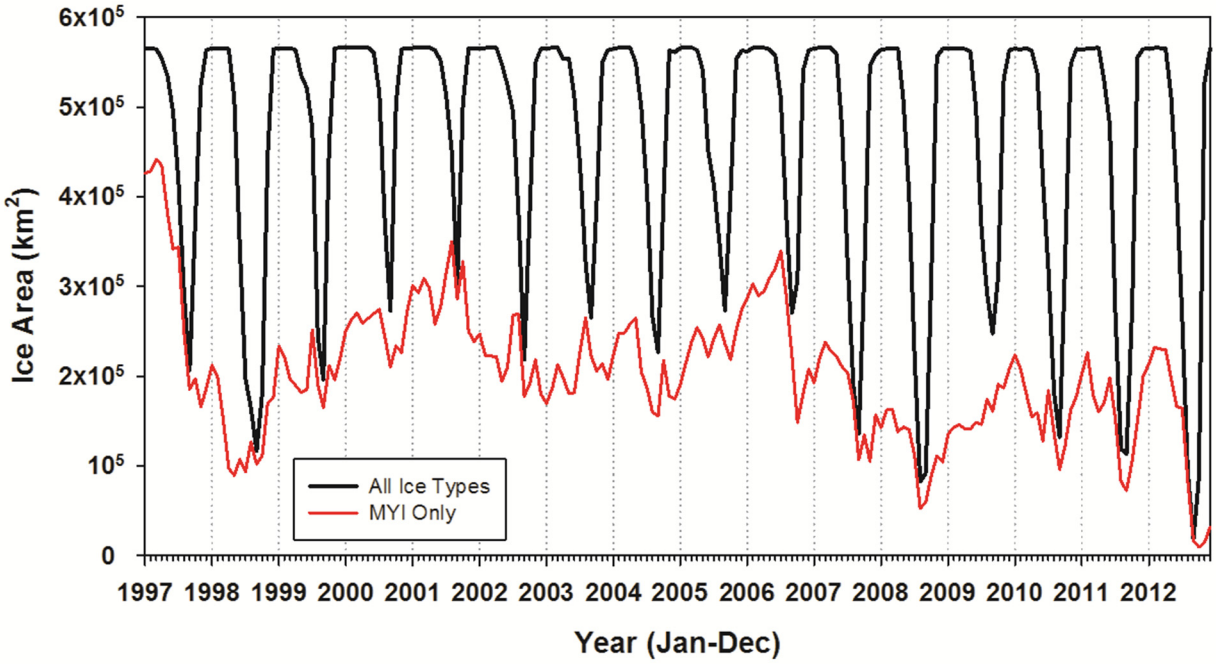

Figure 4.14. January to December inclusive sea ice area in terms of cumulative and MYI-only ice types for the Beaufort Sea between 1997 and 2012.

Monthly sea ice concentration composites for September in each of the 16 years of the 1997-2012 time series is shown in Figure 4.15. Spatial variability in September sea ice concentration is high, although it is clear that the most ice-rich areas continue to be along the northwestern Canadian Arctic Archipelago where the oldest and thickest MYI in the world resides (Bourke and Garrett, 1987; Maslanik et al., 2011). Medium-to-high concentrations of sea ice in the Beaufort Sea extended into the Western Parry Channel of the CAA, except in 1998, 1999, 2007, 2008, 2010, 2011 and 2012 (Figure 4.15). All the latter years except 1999 have been associated with nearly ice-free conditions in the Northwest Passage (Howell et al., 2013a). The last several years also illustrate the dramatic reduction in September sea ice within the Beaufort Sea which has been the subject of several studies (Perovich and Richter-Menge, 2009; Kwok and

Cunningham, 2010; Barber et al., 2014; Krishfield et al., 2014). For example, the extreme minimum during summer 2007 was unique in that a series of related processes including anomalously-high (+500%) surface absorption of solar radiation in the Beaufort Sea (Perovich et al., 2008), a pan-Arctic sea ice thinning trend of -0.57 m decade^{-1} during September between 1987-2006 (Lindsay et al., 2009), and a persistent presence of a high pressure atmospheric pattern over the Canada Basin (Wang et al., 2009) worked together to produce the optimal conditions for a dramatic sea ice extent minimum. The continuing decline of the ice pack raises questions concerning the root causes of decreases in sea ice area as well as possible responses in sea ice dynamics.

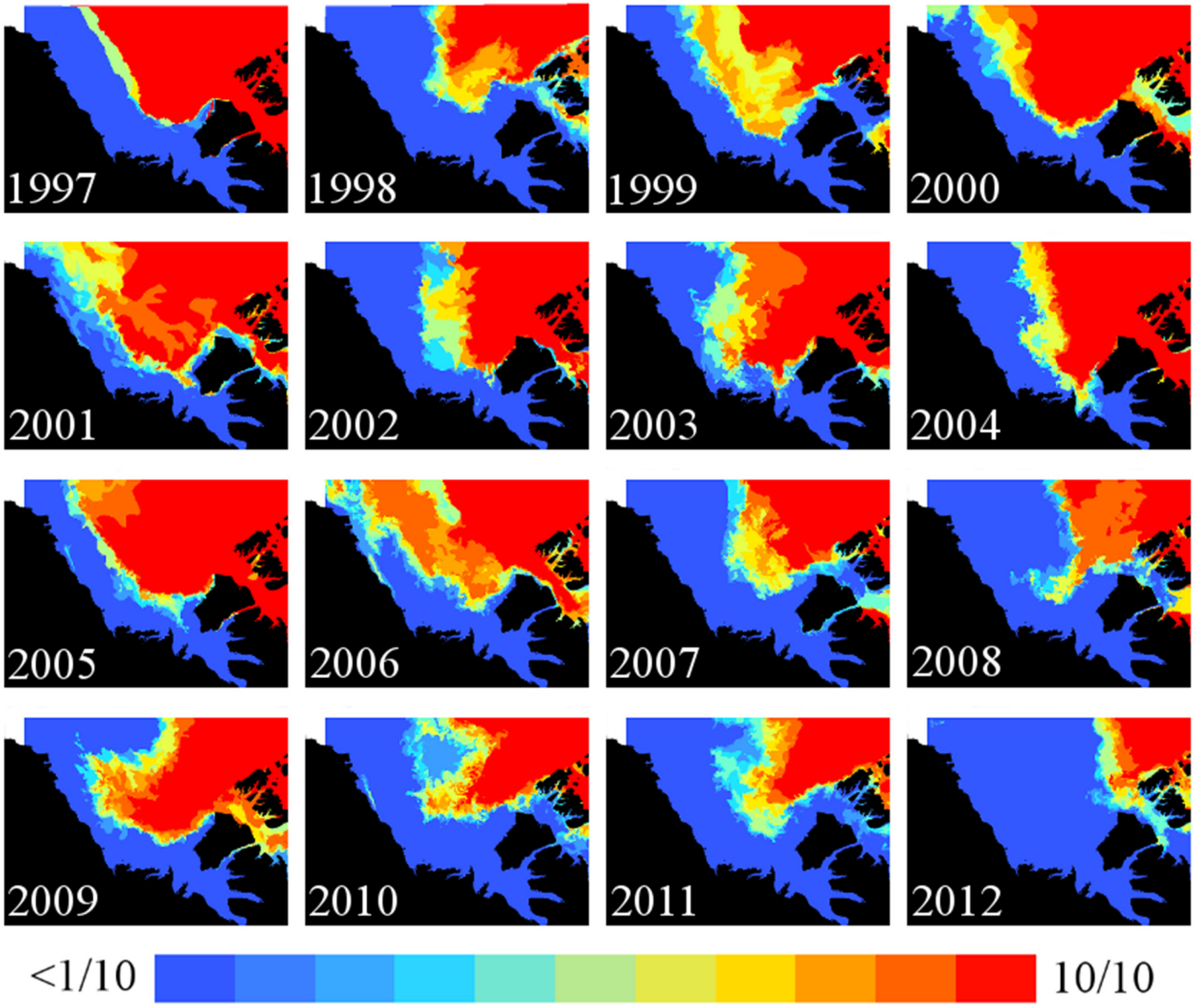

Figure 4.15. September median sea ice concentration for 1997-2012 time series.

4.3.2. Sea Ice Motion

Figure 4.16 shows the 1997 to 2012 time series of JASO ice drift speed. The mean JASO sea ice motion over the entire period was 4.78 km day^{-1} (±3.30 km day^{-1}) and ranged from 2.04 km day^{-1} in 1997 to 10.67 km day^{-1} in 2009. A significant (at 99% confidence interval) positive linear trend of 0.07 km day^{-1} month^{-1} is apparent. This trend represents a 1.5% increase per month in average JASO ice motion speeds when referencing the 1997-2012 mean. Kwok et al. (2013) reported a 17.7% increase per decade in pan-Arctic drift speeds during summer (JJAS) months between 2001 and 2009. The results here show considerably larger changes in sea ice motion within the confines of the Beaufort Sea. In terms of monthly ice drift speeds during the same time

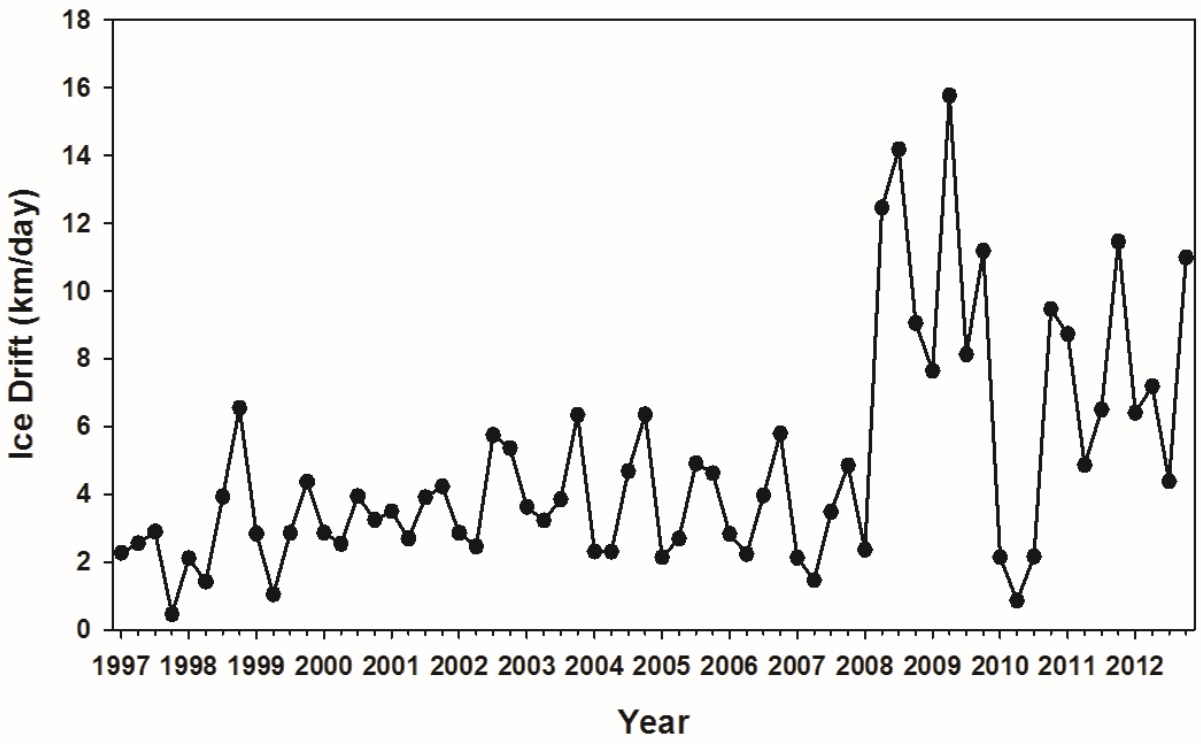

Figure 4.16. Monthly mean ice drift speed time series for JASO month range between 1997 and 2012 in the Beaufort Sea.

period, October (i.e. the month with the highest mean ice velocity) was shown to have a positive trend of 0.55 km day^{-1} $year^{-1}$ (significant at 99% confidence interval). July, August and September also produced positive trends, although none were statistically significant at greater than 86% confidence.

In order to explore possible factors influencing sea ice motion in the Beaufort Sea, correlation analysis between JASO ice motion and SLP, total ice area, open water (OW) area, MYI area, FYI area, and the AO index was performed. Table 4.3 shows that when examining the relationships between these detrended variables on an intermonth basis, SLP and MYI area are found to have relationships significant at >90% confidence. When compared on an annual basis (i.e. JASO months averaged), only SLP is found to have any significant correlation at 0.44 (at 91% confidence interval) (Table 4.4), implying that changes in sea ice area do not necessarily relate to changes in ice motion, and the AO index is generally not ideal for explaining recent variability in ice motion. The negative relationship between MYI and sea ice motion presents the theory that with less MYI, sea ice tends to exhibit faster drift speeds. This would imply that by weakening the mechanical strength of the ice pack by reducing the amount of resilient MYI, it becomes more vulnerable to changes in the dominant forcing terms in the ice motion equation presented in section 2.1.3. This supports the findings of Kwok et al. (2013) who suggest that recent positive trends in drift speed did not appear to correlate with surface wind anomalies and instead more strongly related to negative trends in MYI coverage and thickness.

Table 4.3. Correlation coefficients between detrended CIS-ASITS annual ice drift speed (JASO-averaged) and ancillary variables between 1997 and 2012. Bolded values are significant at >90% confidence.

		AO Index	Total Ice Area	OW Area	MYI Area	FYI Area	SLP
Ice Motion	R	-0.06	0.08	-0.08	**-0.23**	-0.19	**0.23**
	sig	0.64	0.53	0.53	0.07	0.13	0.07

Table 4.4. Correlation coefficients between detrended CIS-ASITS monthly (JASO) ice drift speed and ancillary variables between 1997 and 2012. Bolded values are significant at >90% confidence.

		AO Index	Total Ice Area	OW Area	MYI Area	FYI Area	SLP
Ice Motion	R	-0.16	-0.18	0.18	-0.29	0.14	**0.44**
	sig	0.54	0.50	0.50	0.28	0.61	0.09

4.3.3. Sea Ice Area Flux

Recent changes in monthly sea ice exchange between the Beaufort Sea and surrounding regions (section 4.2) show considerable variability in net fluxes across the time series at each of the 3 exchange gates. The following sections discuss possible driving factors that contribute to these changes as well as trends at each exchange gate.

At the Prince Patrick gate, positive net exchange dominates monthly net ice exchange for JASO months in all years with peak net exchange values of +37.2 x 10^4 km^2 in 2005, +34.2 x 10^4 km^2 in 2010, and +28.5 x 10^4 km^2 in 2004 (Figure 4.17a). Years where net negative ice exchange occurred in the JASO month range reached peak values of -3.7 x 10^4 km^2 in 2000 and -1.2 x 10^4 km^2 in 2006. The composition of sea ice that transited the Prince Patrick gate is expected to be made up of predominantly MYI due to its proximity to the large MYI source north of the CAA (Bourke and Garrett, 1987). This proved to be true for the 1997-2006 period, where MYI consistently attributed for more than 70% of the sea ice that transited across the gate during JASO

months (Figure 4.17a). However, this changed in more recent years when MYI fraction dropped to as low as ~20% in September/October 2012 (Figure 4.12b). No significant trends in monthly or JASO-averaged ice area flux were found (Table 4.5), indicating that there has not been considerable change in area flux for the Prince Patrick gate. When JASO monthly exchange across the Prince Patrick gate was correlated with the SE Beaufort gate, a weak positive correlation of 0.29 (significant at 97% confidence interval) was found (Table 4.6). This correlation strengthened to 0.50 (significant at 95% confidence interval) when the JASO monthly fluxes were averaged to produce a seasonal flux estimate, indicating that while little relationship exists between the gates on a monthly level, seasonal ice exchange across the Prince Patrick gate is moderately related to ice area flux via the SE Beaufort gate.

Table 4.5. Summary of trend for monthly and JASO-averaged net flux for the Prince Patrick (PP), Southeast Beaufort (SEB) and Barrow (B) gates.

		PP	SEB	B
Monthly Net Flux ($km^2\ month^{-1}$)	Trend	-180.76	461.96	2.51
	sig	0.22	0.69	0.83
JASO-Averaged Net Flux ($km^2\ year^{-1}$)	Trend	1619.80	5260.90	6967.45
	sig	0.89	0.69	0.49

Table 4.6. Correlation coefficients for 1997-2012 monthly (N=64) and JASO-averaged (N=16) sea ice area net flux for the Southeast Beaufort (SEB), Prince Patrick (PP), and Barrow (B) gates. Bolded values are significant at >90% confidence.

		SEB vs B	SEB vs PP	B vs PP
Monthly Net Flux	R	**-0.54**	**0.29**	**0.22**
	sig	0.00	0.02	0.08
JASO-Averaged Net Flux	R	-0.37	**0.50**	-0.24
	sig	0.16	0.05	0.36

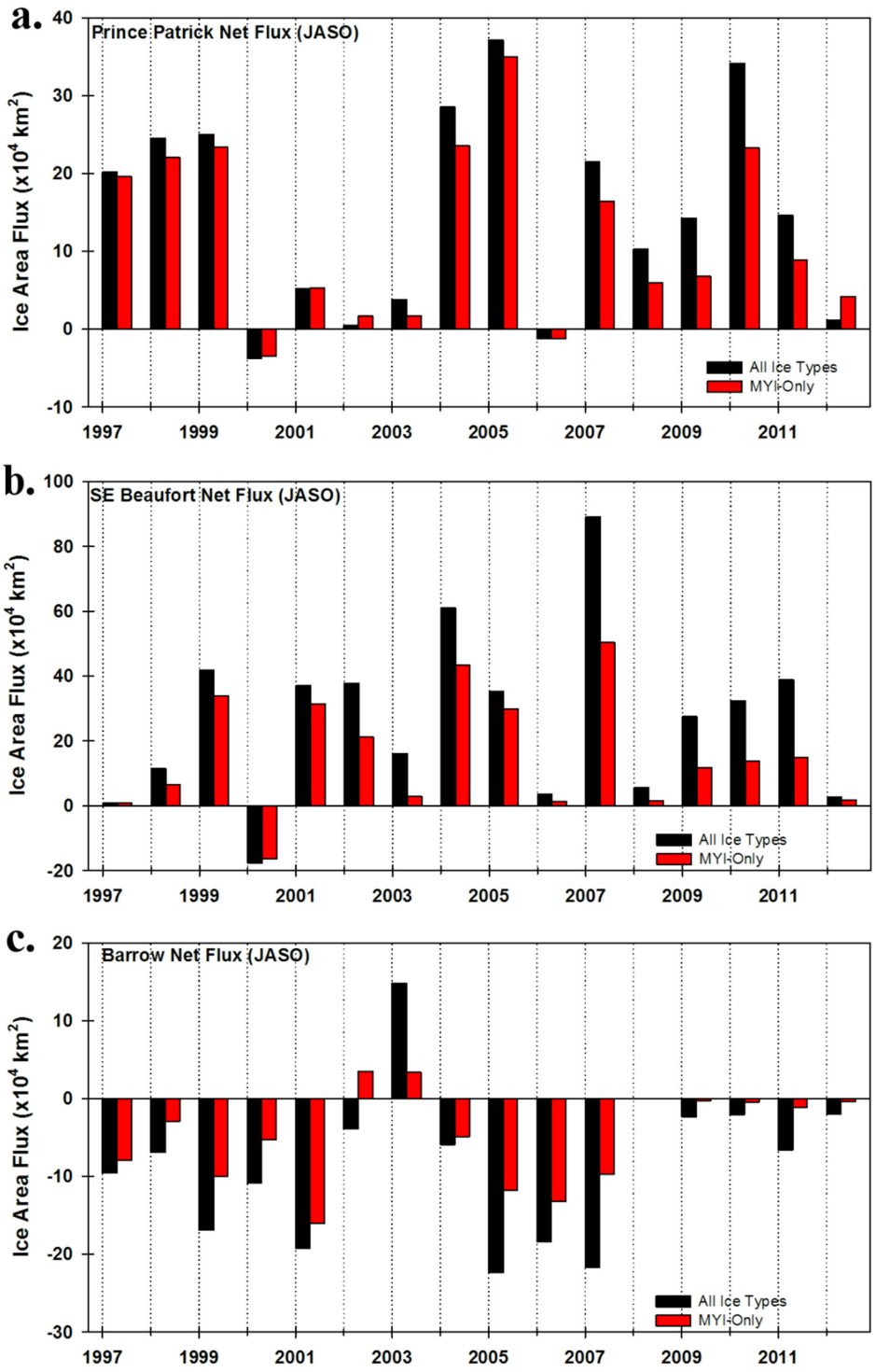

Figure 4.17. Annual net sea ice area flux for JASO months at the Prince Patrick (a), SE Beaufort (b) and Barrow (c) exchange gates.

Annual net flux for the JASO months was predominantly positive at the SE Beaufort gate, indicating primarily westward flow of sea ice area especially in 2007 when the interannual maximum net flux of +89.0 x 10^4 km^2 was reached (Figure 4.17b). However, during 2000 the net annual JASO exchange was anomalously negative at -17.8 x 10^4 km^2, indicating a net flux of ice area towards the CAA. MYI concentration of sea ice transiting the SE Beaufort gate followed a similar evolution as seen at the Prince Patrick gate, where high MYI fractions of 60-80% were seen in JASO months between 1997 and 2006 before dramatically lowering during 2007 to less than 40% of the ice pack (Figure 4.17b). No significant trends in monthly or JASO-averaged ice area flux were found for the SE Beaufort gate (Table 4.5), indicating that little changed in ice exchange during the period of RADARSAT measurements. JASO-averaged sea ice flux across the SE Beaufort gate between 1997 and 2012 correlated well with Prince Patrick ice flux as mentioned previously, but no significant relationship was found when correlating JASO-averaged ice area flux across the Prince Patrick and Barrow gates (Table 4.6). When correlating SE Beaufort gate and Barrow gate monthly net fluxes for the same year range, a moderate negative relationship was found at -0.54 (significant at 99% confidence). When considering the direction of inflow and outflow shown in Figure 3.4, this correlation indicates that net ice area flux crossing the SE Beaufort gate in a southward-bound direction is significantly related to net ice area flux exiting the Beaufort Sea via the Barrow gate.

Between 1997 and 2007, sea ice at the Barrow gate almost always experienced considerable net outflow during JASO months (Figure 4.17c). After 2007, net JASO exchange shows a dramatic reduction in overall ice area flux. Based on the increases in absorbed solar

radiation between 1997 and 2012 in Figure 4.18 and Figure 4.19 as well as previous literature which suggests that the Beaufort Sea is experiencing increased melt (Kwok and Cunningham, 2010), this decrease in ice area flux may be partially the result of a general lack of sea ice in the vicinity of the Barrow gate. However, no significant correlations between area exchange and absorbed solar radiation or open water area during summer were found (Table 4.7). September sea ice concentration for 2008-2012 (Figure 4.15) shows the decline of sea ice coverage spatially, where late-summer sea ice extents have retreated too far north to be able to drift through the Barrow gate. Despite these changes in flux amounts, no significant trends in net area flux were found for the Barrow gate (Table 4.5). As shown in Figure 4.17c, most years in the time series experience net outflow of sea ice in July through October from the Beaufort Sea with the exception of 2002 and 2003. Annual net export of JASO months peaks in 2005 and 2007, with -22.3 $x10^4$ km^2 and -21.7 x 10^4 km^2, respectively. It appears that in 2002 a net outflow of sea ice occurs while MYI for the same year experiences a net inflow. This is possibly the result of a rapid drop in MYI concentration during a large net outflow in October 2002 (Figure 4.12c) having a reduced effect on net MYI exchange values. No significant correlations were found for JASO-averaged net flux between the Barrow gate and the Prince Patrick/SE Beaufort gates (Table 4.6). Along with the moderate correlation between monthly net flux at the Barrow and SE Beaufort gates, a weak positive correlation of 0.22 (significant at 92% confidence) was found when comparing Barrow and Prince Patrick estimates.

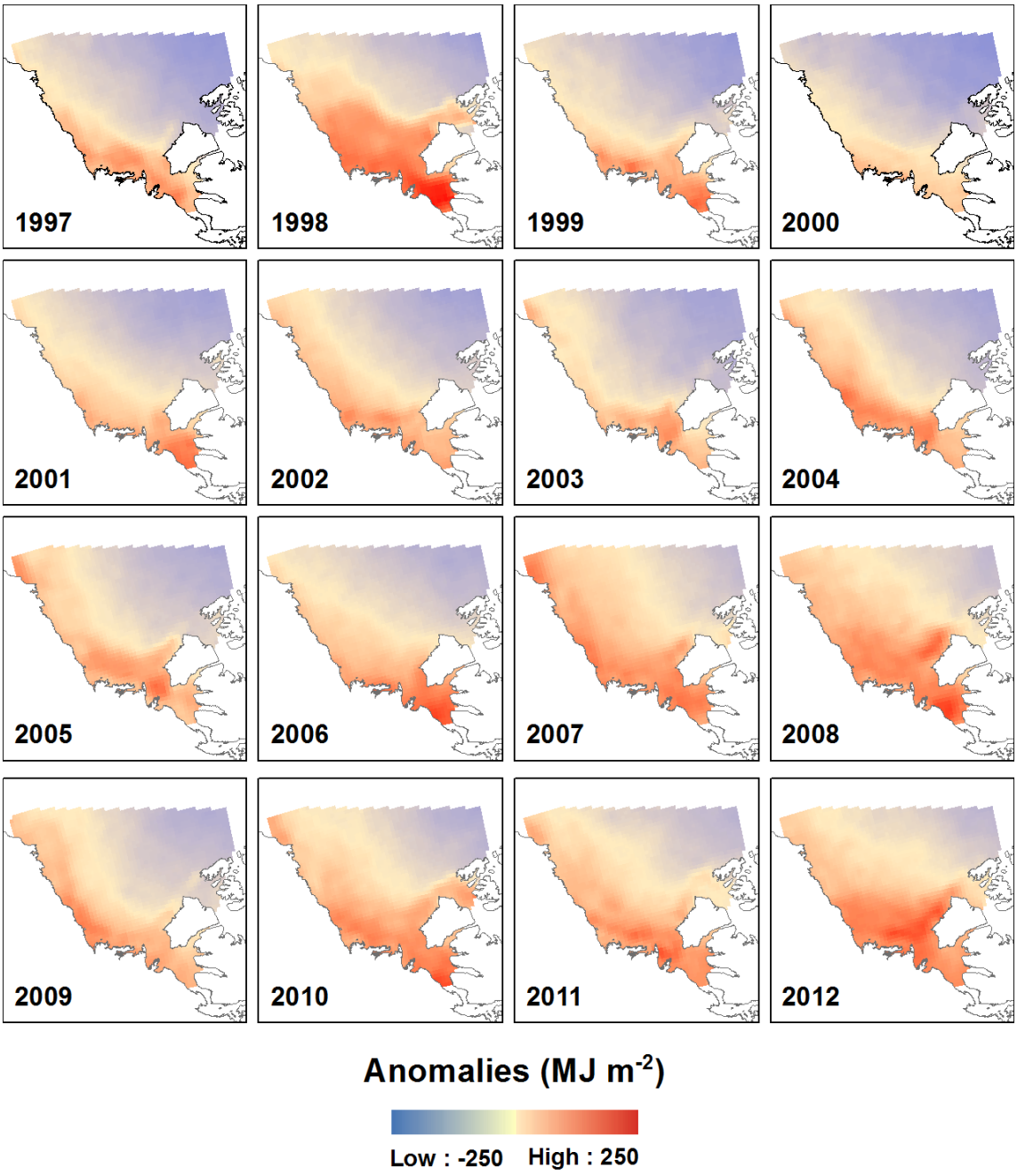

Figure 4.18. May-September total absorbed solar radiation (Q_{total}) anomaly map for 1997-2012 time series.

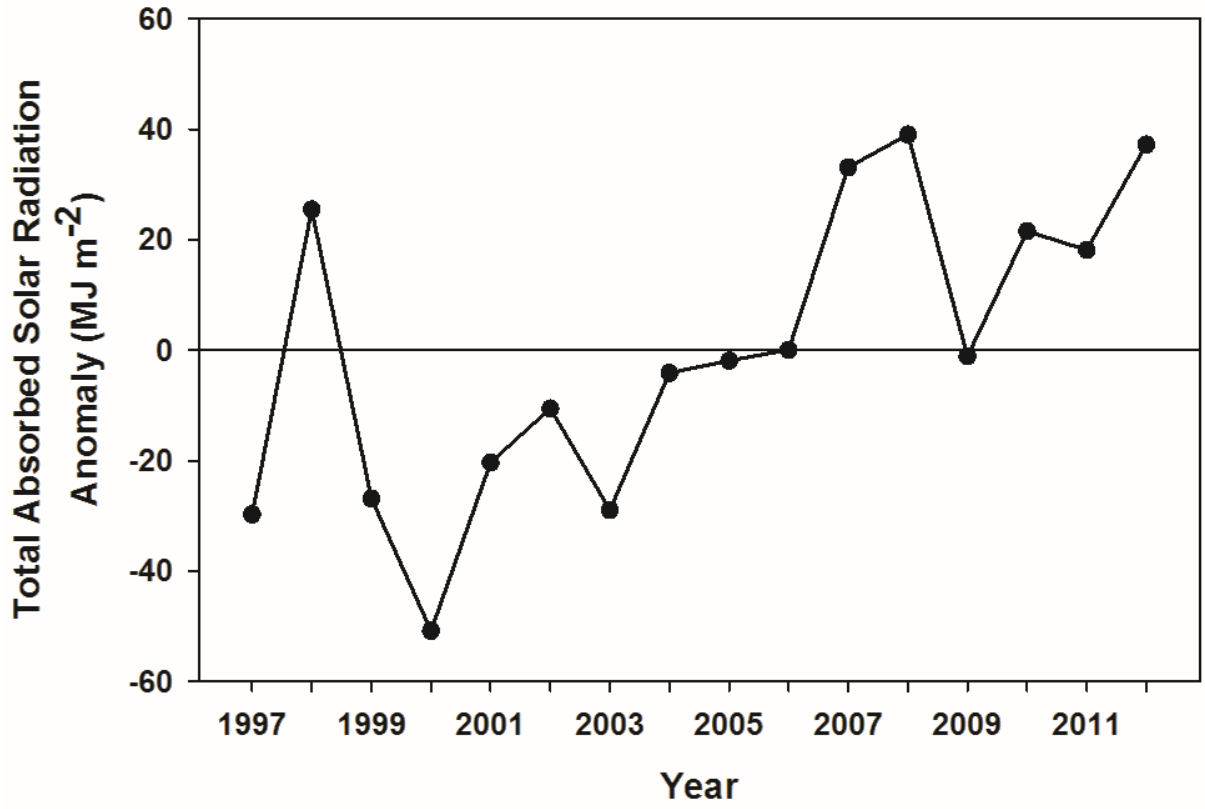

Figure 4.19. Total absorbed solar radiation (Q_{total}) anomaly based on 1997-2012 average.

Table 4.7. Correlation coefficients between detrended total absorbed radiation (Q_{total}), open water (OW) area and JASO-averaged net flux at the Prince Patrick (PP), Southeast Beaufort (SEB) and Barrow (B) gates between 1997 and 2012. Bolded values are significant at >90% confidence.

		PP Flux	SEB Flux	B Flux
Q_{total} (MJJAS)	R	-0.33	-0.74	0.57
	sig	0.58	0.15	0.31
OW Area (JASO)	R	0.24	-0.12	0.23
	sig	0.37	0.66	0.39

Of the 3 exchange gates discussed in this study, the most dramatic changes in sea ice area flux occur at the Barrow gate with reductions in net area exchange shown between 2008 and 2012 (Figure 4.17c). Root causes of this decline are difficult to identify, owing partially to the lack of statistical correlation between area fluxes and related climate variables. However, the combination of melt onset occurring 2.4 days decade^{-1} earlier (Stroeve et al., 2014), the thinning trend of the greater ice pack (Lindsay et al., 2009), and a distinct surface warming signal brought about by increased May-September Q_{total} anomalies (Figure 4.18, Figure 4.19) present compelling evidence that sea ice being imported into the Beaufort Sea does not survive long enough to be exported to neighbouring regions. The trend in May-September Q_{total} anomalies is 4.6 MJ m^{-2} year^{-1} (at 99% confidence) between 1997 and 2012. These increasing Q_{total} anomalies suggest that a higher number of open water areas are absorbing more solar energy, thus increasing the upper ocean layer's energy storage which would be released during the following winter, resulting in inhibited ice growth and predisposing subsequent seasons in a classic feedback mechanism. Furthermore, findings by Kwok and Cunningham (2010) show that recent increased MYI melt in the Beaufort has contributed considerably to the overall decline in Arctic MYI, which would support the theory that much of the Beaufort Sea ice pack does not survive long enough to recirculate into the Arctic Ocean.

The past patterns of migration of sea ice in the Beaufort Sea are characterised by a distinctive clockwise rotation around the Beaufort Sea High pressure system that serves to circulate sea ice in the Canada Basin (Figure 2.10). Under past conditions, a portion of the sea ice that survived the melt season would be exported via the Barrow gate as shown in Figure 4.17c, but in

recent years this exchange has dropped precipitously despite little change in the clockwise direction of ice motion. Without solid evidence of changes in the prevailing circulation patterns, the controlling factors in the changes in sea ice exchange may be found in the variability of sea ice physical characteristics and thermodynamic processes in the Beaufort Sea. Previous evidence suggests that the remaining sea ice cover has become progressively younger in age without much recovery in subsequent growth seasons (e.g. Figure 2.14, Figure 2.24). Further, mean summer sea ice thickness in the Beaufort Sea has experienced a ~50% decline when comparing the 1958-1976 and 2003-2007 means (Figure 1.2). These change in ice age and thickness accentuate the vulnerability of sea ice to the dominant wind and current forcings terms in the ice momentum balance equation (Equation 2.2) by increasing the effects of anomalous wind conditions on the speed of ice drift. With more open water area for sea ice to drift in due to declining summer sea ice concentrations (Figure 4.15), it is not an unusual result for CIS-ASITS ice motion estimates to be greater in recent years.

In terms of thermodynamic processes, prior conditions indicated that a balance between melt in summer and ice replenishment in the winter was relatively stable. However, it is clear that the Beaufort Sea is experiencing increases in absorbed solar radiation (e.g. Figure 4.18, Figure 4.19) along with increases in melt (Perovich et al., 2008; Perovich and Richter-Menge, 2009), SAT (Stroeve et al., 2014), and SST (Steele et al., 2008). This general heating of the ocean and atmosphere has a detrimental effect on sea ice in the Beaufort Sea by dramatically reducing the survivability of sea ice that is imported to the region during summer months, regardless of stage of ice maturity. Although the pattern of ice migration in the Beaufort Sea remains unchanged,

where sea ice is predominantly imported from the northeast and exported to the northwest, fewer instances of ice export are being observed due to the increasing effectiveness of melt processes. Warmer ocean and air temperatures coupled with a thinner and younger ice pack provide ample evidence that the Beaufort Sea is increasingly becoming a region where sea ice is lost rather than a relatively safe zone for ice to thicken and mature. The results of this study also suggest that this scenario is becoming more of a reality, with declines in sea ice area and concentration (Figure 4.14, Figure 4.15) coupled with relatively little variability in sea ice import (Figure 4.17a, b) along with dramatic changes in sea ice export (Figure 4.17c) indicating that sea ice does not survive for long with the presence of thermodynamic processes that favour increased melt in the region.

4.4. Summary

When compared to 4 independent ice motion datasets, the results from the CIS-ASITS approach related most favourably to the PIOMAS gridded ice motion speeds, and least favourably to the IABP interpolated product. In all comparisons, the CIS-ASITS results almost always have a slight positive bias, indicating relatively faster ice motion at co-located points in the independent datasets. Analysis of a time series spanning 1997 to 2012 shows that 5 of the 6 monthly sea ice area minimums in the Beaufort Sea have occurred since 2007 coincident with a northward retreat of the ice pack in recent years. This CIS-ASITS data record identified a positive trend of 0.07 km day^{-1} $year^{-1}$ for JASO ice motion for the 1997-2012 time series. October months most often exhibited the highest mean monthly ice drift speeds as well as the highest extreme maximums. A significant correlation of 0.44 was shown between JASO monthly sea ice motion speeds and

NCEP/NCAR SLP, indicating that variability in ice drift speeds can be partially explained by surface pressure fields in the Beaufort Sea region.

Sea ice area exchange analysis for 3 predefined gates revealed little statistical evidence of trends in the 1997-2012 time series (Table 4.5). Considerable variability exists in JASO monthly net flux, although MYI fraction at all 3 gates has decreased over the course of the time series. This change in MYI content did not have a statistically significant relationship with net exchange amounts. In recent years, JASO sea ice fluxes have been reduced to near-zero at the Barrow gate. Based on the decreased extent of the Beaufort Sea ice pack and increases in absorbed solar radiation since 2008, there is evidence that sea ice dynamically imported into the Beaufort Sea quickly melts before it can be recirculated out towards the Chukchi and East Siberian Sea regions.

Chapter 5. Conclusions

5.1. Key Findings

Understanding the effects of a changing Arctic climate system on the dynamic properties of sea ice is important for gaining insight into related systems including the surface energy balance, primary production, and wildlife habitat. A significant increase in variability and trends in sea ice motion in the Beaufort Sea will produce a heightened need for updated ice motion charts with shorter time periods between issuances to avoid hazards, and motivate improved ice motion forecasting in support of potential transportation through the Northwest Passage sea route. The availability of high-resolution active microwave satellite imagery will assist in the assessment of ice motion by resolving local-scale dynamic events with a synoptic observational repeat cycle. Remote sensing imagery is also useful for evaluating the results of modeling studies for which the acquisition of timely and accurate observational data can be difficult.

In this study of sea ice in the Beaufort Sea, an estimate of the current conditions of sea ice motion for JASO between 1997 and 2012 was derived from RADARSAT imagery using the CIS-ASITS method. With a time series mean ice drift velocity of 4.78 km day^{-1} (±3.30 km day^{-1}), JASO sea ice motion was found to have a positive trend of 0.07 km day^{-1} $month^{-1}$ (significant at 99% confidence interval). This represents a ~1.5% increase in JASO ice drift speeds per month when referencing the 1997-2012 mean, which is considerably higher than the 17.7% $decade^{-1}$ increase in JJAS drift speeds reported by Kwok et al. (2013). The results of the CIS-ASITS method were compared to 4 independent datasets, which showed that the CIS-ASITS results consistently exhibited a positive bias ranging from 0.63 to 2.02 km day^{-1}. No strong correlations were found

between the CIS-ASITS ice motion results and ancillary datasets, with the highest being 0.65 (significant at 95% confidence interval) when compared to the RIPS modeled ice motion dataset.

Estimates of sea ice area exchange between the Beaufort Sea and surrounding waters were calculated for a series of 3 exchange gates during the JASO 1997-2012 time series. Variability in net exchange was high for most months, with a decline in MYI concentration for sea ice transiting across all 3 gates. No significant trend in monthly or JASO-averaged net flux was found for any of the 3 gates (Table 4.5). The Barrow gate was shown to have dramatic decreases in net ice area flux to the Chukchi Sea region in recent years (2008-2012). This raised the question of what processes are driving the observed decline in ice area exchange. Decreased ice export via the Barrow gate suggests that sea ice entering the Beaufort Sea from the Prince Patrick gate may be melting at a heightened rate before it can circulate towards the Barrow gate.

Investigating the causal processes affecting changes in sea ice motion and area flux revealed that SLP had a consistently significant albeit weak to moderate correlation with ice motion, and few variables were useful in accounting for variability in net flux amounts. A positive trend in Q_{total}, the earlier occurrence of melt as reported by Stroeve et al. (2014), and the overall thinning trend of the Arctic ice pack, suggests that a considerable fraction of the sea ice that is imported to the Beaufort Sea no longer survives the melt season. This is supported by the reduced outflow across the Barrow gate in recent years shown in Figure 4.12, by prior findings of increased melt in the Beaufort Sea (Perovich et al., 2008; Kwok and Cunningham, 2010) and rapid retreat of sea ice extent following melt seasons (Stroeve et al., 2011).

5.2. Implications

A high-resolution and long-term record of sea ice motion in the Beaufort Sea provides detailed information for end users in the marine navigation and shipping and natural resources extraction sectors. Understanding the present conditions of sea ice circulation in the Beaufort Sea is of particular importance in the planning and deployment of offshore installations and subsequent maritime transportation corridors. Significant changes in the variability of sea ice motion in recent years are directly relevant to environmental risk assessments for these interested parties, and the positive trend in ice motion shown in this study implies that there may be increased risk associated with mobile ice hazards that may interfere with economic activity in the region. Eventual connections between ice area and volume flux will also be highly relevant to offshore operations and shipping.

The ice motion tracking results produced from the CIS-ASITS method employed in this study will be used to evaluate RIPS sea ice motion predictions to prepare for the eventual operational use by the Canadian Meteorological Centre for sea ice forecasting. The inclusion of sea ice tracking algorithms which use active microwave satellite imagery will provide a robust data source for driving, tuning and evaluating model studies.

High-resolution active microwave satellite imagery provide a better baseline for the production of long-term sea ice motion climatologies, as it is far less complex to scale from high resolution results to coarser resolution composite products than vice versa. If the negative trend in Arctic sea ice continues to promote a less extensive overall coverage, the importance of high resolution imagery will grow as the need to examine a thinner and more fractured ice pack becomes

necessary. Further, the issues associated with relatively small swath widths and limited inventories of active microwave imagery are becoming less relevant as advancements are made in sensor technology and formation/constellation orbits of multiple spaceborne sensors. The capability of high-resolution satellite imagery to identify and track individual ice floes is a powerful tool for examining local-scale variability in Arctic sea ice, and will provide key insight into processes that are not currently captured by coarse-resolution observational datasets.

5.3. Future Work

Further analysis of changes and variability in sea ice motion is necessary to continue to build a diverse knowledge base in order to make informed decisions on future activities in the Beaufort Sea. In addition to acquiring more high-resolution active microwave imagery to provide complete January-December coverage and updating the time series for recent years, recommendations for future studies involving sea ice motion in the Beaufort Sea include:

- Further explore the positive bias in CIS-ASITS velocity estimates compared to other datasets, specifically concerning the possible step change in 2008
- Redefine the area exchange estimation approach to consider individual grid cells as gates, providing a more granular estimate of ice area flux
- Segment the study area into smaller sub-regions for image filtering to optimize swath pair overlap
- Incorporate ice thickness data to examine changes in ice volume exchange between the Beaufort Sea and surrounding waters

- Investigate additional variables including ocean salinity, sea surface height, ocean current velocity, and internal ice stress to examine their relationship with changes in sea ice dynamics
- Adjust the CIS-ASITS method to adapt to increased active microwave data availability (including the RADARSAT Constellation Mission anticipated in 2018)

Addressing these recommendations will improve the understanding of sea ice dynamics in the Beaufort Sea and further assist in robustly characterizing ice behaviour in the region. With a recent emphasis on natural resource exploration in the Arctic, knowledge of the recent changes and variability of sea ice as well as the processes that affect dynamics are integral to moving forward responsibly and sustainably.

References

Aagaard, K., and Carmack, E. C. (1989). The Role of Sea Ice and Other Fresh Water in the Arctic Circulation. *Journal of Geophysical Research*, *94*(C10), 14,485–14,498. doi:10.1029/JC094iC10p14485

Agnew, T., and Howell, S. (2003). The use of operational ice charts for evaluating passive microwave ice concentration data. *Atmosphere-Ocean*, *41*(4), 317–331. doi:10.3137/ao.410405

Barber, D. G., McCullough, G., Babb, D., Komarov, A. S., Candlish, L. M., Lukovich, J. V., … Rysgaard, S. (2014). Climate change and ice hazards in the Beaufort Sea. *Elementa: Science of the Anthropocene*, *2*(1982). doi:10.12952/journal.elementa.000025

Barber, D. G., Yackel, J. J., and Hanesiak, J. M. (2001). Sea Ice, RADARSAT-1 and Arctic Climate Processes: A Review and Update. *Canadian Journal of Remote Sensing*, *27*(1), 51–61.

Bourke, R. H., and Garrett, R. P. (1987). Sea Ice Thickness Distribution in the Arctic Ocean. *Cold Regions Science and Technology*, *13*, 259–280.

Buehner, M., Caya, A., Carrieres, T., and Pogson, L. (2014). Assimilation of SSMIS and ASCAT data and the replacement of highly uncertain estimates in the Environment Canada Regional Ice Prediction System. *Quarterly Journal of the Royal Meteorological Society*. doi:10.1002/qj.2408

Buehner, M., Caya, A., Pogson, L., Carrieres, T., and Pestieau, P. (2013). A New Environment Canada Regional Ice Analysis System. *Atmosphere-Ocean*, *51*(1), 18–34. doi:10.1080/07055900.2012.747171

Canadian Ice Service. (2005). *MANICE: Manual of Standard Procedures for Observing and Reporting Ice Conditions* (9th ed., p. 146). Ottawa, Ontario, Canada.

Cavalieri, D. J., and Parkinson, C. L. (2012). Arctic sea ice variability and trends, 1979–2010. *The Cryosphere*, *6*(4), 881–889. doi:10.5194/tc-6-881-2012

Comiso, J. C. (2012). Large Decadal Decline of the Arctic Multiyear Ice Cover. *Journal of Climate*, *25*(4), 1176–1193. doi:10.1175/JCLI-D-11-00113.1

Comiso, J. C., Parkinson, C. L., Gersten, R., and Stock, L. (2008). Accelerated decline in the Arctic sea ice cover. *Geophysical Research Letters*, *35*(L01703), 1–6. doi:10.1029/2007GL031972

Curry, J. A., Rossow, W. B., Randall, D., and Schramm, J. L. (1996). Overview of Arctic Cloud and Radiation Characteristics. *Journal of Climate*, *9*, 1731–1764.

Curry, J. A., Schramm, J. L., and Ebert, E. E. (1995). Sea Ice-Albedo Climate Feedback Mechanism. *Journal of Climate*, *8*, 240–247.

Derksen, C., Smith, S. L., Sharp, M., Brown, L., Howell, S., Copland, L., … Walker, A. (2012). Variability and change in the Canadian cryosphere. *Climatic Change*, *115*(1), 59–88. doi:10.1007/s10584-012-0470-0

Drobot, S. (2003). Long-Range Statistical Forecasting of Ice Severity in the Beaufort–Chukchi Sea. *Weather and Forecasting*, *18*(6), 1161–1176. doi:10.1175/1520-0434(2003)018<1161:LSFOIS>2.0.CO;2

Eicken, H. (2003). From the Microscopic, to the Macroscopic, to the Regional Scale: Growth, Microstructure and Properties of Sea Ice. In D. N. Thomas & G. S. Dieckmann (Eds.), *Sea Ice: An Introduction to its Physics, Chemistry, Biology and Geology* (1st ed., pp. 22–81). Oxford, UK: Blackwell Science Ltd. doi:10.1002/9780470757161.ch2

Emery, W. J., Fowler, C. W., and Maslanik, J. A. (1995). Satellite remote sensing of ice motion. In M. Ikeda & F. W. Dobson (Eds.), *Oceanographic Applications of Remote Sensing* (pp. 367–379). Boca Raton: CRC Press.

Fowler, C., Emery, W. J., and Maslanik, J. (2004). Satellite-Derived Evolution of Arctic Sea Ice Age: October 1978 to March 2003. *IEEE Geoscience and Remote Sensing Letters*, *1*(2), 71–74. doi:10.1109/LGRS.2004.824741

Fowler, C., Emery, W., and Tschudi, M. (2013). Polar Pathfinder Daily 25 km EASE-Grid Sea Ice Motion Vectors. Version 2. Boulder, Colorado USA: National Snow and Ice Data Center.

Fowler, C., Maslanik, J., Haran, T., Scambos, T., Key, J., and Emery, W. (2000). AVHRR Polar Pathfinder twice-daily 5 km EASE-grid composites. Boulder, Colorado USA: National Snow and Ice Data Center.

Galley, R. J., Else, B. G. T., Prinsenberg, S. J., Babb, D., and Barber, D. G. (2013). Summer Sea Ice Concentration, Motion, and Thickness Near Areas of Proposed Offshore Oil and Gas Development in the Canadian Beaufort Sea – 2009. *Arctic*, *66*(1), 105–116.

Haas, C. (2003). Dynamics versus Thermodynamics: The Sea Ice Thickness Distribution. In D. N. Thomas & G. S. Dieckmann (Eds.), *Sea Ice: An Introduction to its Physics, Chemistry, Biology and Geology* (1st ed., pp. 82–111). Oxford, UK: Blackwell Science Ltd. doi:10.1002/9780470757161.ch3

Haas, C., Hendricks, S., Eicken, H., and Herber, A. (2010). Synoptic airborne thickness surveys reveal state of Arctic sea ice cover. *Geophysical Research Letters*, *37*(L09501), 1–5. doi:10.1029/2010GL042652

Hamidi, D., Lehner, S., and König, T. (2010). *On the Sea Ice Motion Estimation with Synthetic Aperture Radar* (pp. 1–10). Wessling, Germany. Retrieved from http://sss.terrasar-x.dlr.de/papers_sci_meet_4/oral/CAL0166_hamidi.pdf

Howell, S. E. L., Wohlleben, T., Dabboor, M., Derksen, C., Komarov, A., and Pizzolato, L. (2013a). Recent changes in the exchange of sea ice between the Arctic Ocean and the Canadian Arctic Archipelago. *Journal of Geophysical Research: Oceans*, *118*(7), 3595–3607. doi:10.1002/jgrc.20265

Howell, S. E. L., Wohlleben, T., Komarov, A., Pizzolato, L., and Derksen, C. (2013b). Recent extreme light sea ice years in the Canadian Arctic Archipelago: 2011 and 2012 eclipse 1998 and 2007. *The Cryosphere*, *7*(6), 1753–1768. doi:10.5194/tc-7-1753-2013

Hunke, E. C., and Lipscomb, W. H. (2010). *CICE: the Los Alamos Sea Ice Model Documentation and Software User's Manual* (pp. 1–76). Los Alamos, New Mexico.

Kalnay, E., Kanamitsu, M., Kistler, R., Collins, W., Deaven, D., Gandin, L., … Joseph, D. (1996). The NCEP/NCAR 40-Year Reanalysis Project. *Bulletin of the American Meteorological Society*, *77*(3), 437–471. doi:10.1175/1520-0477(1996)077<0437:TNYRP>2.0.CO;2

Key, J. R. (2002a). Streamer User's Guide: Version 3.0. Madison, Wisconsin, USA: Cooperative Institute for Meteorological Satellite Studies, University of Wisconsin-Madison.

Key, J. R. (2002b). The Cloud and Surface Parameter Retrieval (CASPR) system for Polar AVHRR: User's Guide: Version 4.0. Madison, Wisconsin, USA: University of Wisconsin-Madison.

Key, J. R., and Schweiger, A. J. (1998). Tools for atmospheric radiative transfer: Streamer and FluxNet. *Computers and Geosciences*, *24*(5), 443–451. doi:10.1016/S0098-3004(97)00130-1

Key, J. R., Stroeve, J. C., and Fowler, C. (2001). Estimating the cloudy-sky albedo of sea ice and snow from space. *Journal of Geophysical Research*, *106*(D12), 12,489–12,497. doi:10.1029/2001JD900069

Komarov, A., and Barber, D. (2012). Detection of sea ice motion from co- and cross-polarization RADARSAT-2 images. In *2012 IEEE International Geoscience and Remote Sensing Symposium* (Vol. 7, pp. 3277–3280). IEEE. doi:10.1109/IGARSS.2012.6350604

Komarov, A. S., and Barber, D. G. (2014). Sea Ice Motion Tracking From Sequential Dual-Polarization RADARSAT-2 Images. *IEEE Transactions on Geoscience and Remote Sensing*, *52*(1), 121–136. doi:10.1109/TGRS.2012.2236845

Krishfield, R. A., Proshutinsky, A., Tateyama, K., Williams, W. J., Carmack, E. C., McLaughlin, F. A., and Timmermans, M.-L. (2014). Deterioration of perennial sea ice in the Beaufort Gyre from 2003 to 2012 and its impact on the oceanic freshwater cycle. *Journal of Geophysical Research: Oceans*, *119*, 1271–1305. doi:10.1002/2013JC008999

Kwok, R. (1998). *The RADARSAT Geophysical Processor System*. Pasadena, CA.

Kwok, R. (2006). Contrasts in sea ice deformation and production in the Arctic seasonal and perennial ice zones. *Journal of Geophysical Research*, *111*(C11), C11S22. doi:10.1029/2005JC003246

Kwok, R. (2007). Near zero replenishment of the Arctic multiyear sea ice cover at the end of 2005 summer. *Geophysical Research Letters*, *34*(5), L05501. doi:10.1029/2006GL028737

Kwok, R. (2010). Satellite remote sensing of sea-ice thickness and kinematics: a review. *Journal of Glaciology*, *56*(200), 1129–1140. doi:10.3189/002214311796406167

Kwok, R., and Cunningham, G. F. (2010). Contribution of melt in the Beaufort Sea to the decline in Arctic multiyear sea ice coverage: 1993–2009. *Geophysical Research Letters*, *37*(20), 1–5. doi:10.1029/2010GL044678

Kwok, R., Cunningham, G. F., and Nghiem, S. V. (2003). A study of the onset of melt over the Arctic Ocean in RADARSAT synthetic aperture radar data. *Journal of Geophysical Research*, *108*(C11), 3363. doi:10.1029/2002JC001363

Kwok, R., Curlander, J. C., McConnell, R., and Pang, S. S. (1990). An ice-motion tracking system at the Alaska SAR facility. *IEEE Journal of Oceanic Engineering*, *15*(1), 44–54. doi:10.1109/48.46835

Kwok, R., and Rothrock, D. A. (1999). Variability of Fram Strait ice flux and North Atlantic Oscillation. *Journal of Geophysical Research*, *104*(1998), 5177–5189. doi:10.1029/1998JC900103

Kwok, R., and Rothrock, D. A. (2009). Decline in Arctic sea ice thickness from submarine and ICESat records: 1958–2008. *Geophysical Research Letters*, *36*(15), 1–5. doi:10.1029/2009GL039035

Kwok, R., Spreen, G., and Pang, S. (2013). Arctic sea ice circulation and drift speed: Decadal trends and ocean currents. *Journal of Geophysical Research: Oceans*, *118*(5), 2408–2425. doi:10.1002/jgrc.20191

Lemieux, J.-F., Beaudoin, C., Dupont, F., Roy, F., Smith, G. C., Shlyaeva, A., … Ferry, N. (2014). The Regional Ice Prediction System (RIPS): verification of forecast sea ice concentration. *Quarterly Journal of the Royal Meteorological Society*.

Lindsay, R. W., and Stern, H. L. (2004). A New Lagrangian Model of Arctic Sea Ice. *Journal of Physical Oceanography*, *34*(1), 272–283. doi:10.1175/1520-0485(2004)034<0272:ANLMOA>2.0.CO;2

Lindsay, R. W., Zhang, J., Schweiger, A., Steele, M., and Stern, H. (2009). Arctic Sea Ice Retreat in 2007 Follows Thinning Trend. *Journal of Climate*, *22*, 165–176. doi:10.1175/2008JCLI2521.1

Livingstone, C. E., Onstott, R. G., Arsenault, L. D., Gray, A. L., and Singh, K. P. (1987). Microwave Sea-Ice Signatures Near the Onset of Melt. *IEEE Transactions on Geoscience and Remote Sensing*, *GE-25*(2), 174–187. doi:0196-2892/87/0300-0174$01 .00

Lukovich, J. V., Babb, D. G., and Barber, D. G. (2011). On the scaling laws derived from ice beacon trajectories in the southern Beaufort Sea during the International Polar Year - Circumpolar Flaw Lead study, 2007–2008. *Journal of Geophysical Research*, *116*, C00G07. doi:10.1029/2011JC007049

Lukovich, J. V., and Barber, D. G. (2006). Atmospheric controls on sea ice motion in the southern Beaufort Sea. *Journal of Geophysical Research*, *111*(D18), 1–12. doi:10.1029/2005JD006408

Malenovský, Z., Rott, H., Cihlar, J., Schaepman, M. E., García-santos, G., Fernandes, R., and Berger, M. (2012). Sentinels for science: Potential of Sentinel-1 , -2 , and -3 missions for scientific observations of ocean, cryosphere, and land. *Remote Sensing of Environment*, *120*, 91–101. doi:10.1016/j.rse.2011.09.026

Markus, T., Stroeve, J. C., and Miller, J. (2009). Recent changes in Arctic sea ice melt onset , freezeup , and melt season length. *Journal of Geophysical Research*, *114*(C12024), 1–14. doi:10.1029/2009JC005436

Maslanik, J. A., Fowler, C., Stroeve, J., Drobot, S., Zwally, J., Yi, D., and Emery, W. (2007). A younger, thinner Arctic ice cover: Increased potential for rapid, extensive sea-ice loss. *Geophysical Research Letters*, *34*(24), L24501. doi:10.1029/2007GL032043

Maslanik, J. A., Key, J., Fowler, C. W., Nguyen, T., and Wang, X. (2001). Spatial and temporal variability of satellite-derived cloud and surface characteristics during FIRE-ACE. *Journal of Geophysical Research*, *106*(D14), 15,233–15,249. doi:10.1029/2000JD900275

Maslanik, J., Stroeve, J., Fowler, C., and Emery, W. (2011). Distribution and trends in Arctic sea ice age through spring 2011. *Geophysical Research Letters*, *38*(13), 2–7. doi:10.1029/2011GL047735

Maykut, G. A. (1986). The surface heat and mass balance. In N. Untersteiner (Ed.), *The Geophysics of Sea Ice* (pp. 395–464). Springer US. doi:10.1007/978-1-4899-5352-0_6

Maykut, G. A., and McPhee, M. G. (1995). Solar heating of the Arctic mixed layer. *Journal of Geophysical Research*, *100*(C12), 24,691–24,703. doi:10.1029/95JC02554

Meier, W. N., Hovelsrud, G. K., van Oort, B. E. H., Key, J. R., Kovacs, K. M., Michel, C., … Reist, J. D. (2014). Arctic sea ice in transformation: A review of recent observed changes and impacts on biology and human activity. *Reviews of Geophysics*, *51*, 1–33. doi:10.1002/2013RG000431

Meier, W. N., Stroeve, J., and Fetterer, F. (2007). Whither Arctic sea ice? A clear signal of decline regionally, seasonally and extending beyond the satellite record. *Annals of Glaciology*, *46*(1), 428–434. doi:10.3189/172756407782871170

Melling, H., and Riedel, D. A. (2005). Trends in the draft and extent of seasonal pack ice, Canadian Beaufort Sea. *Geophysical Research Letters*, *32*(L24501), 1–5. doi:10.1029/2005GL024483

Olason, E., and Notz, D. (2014). Drivers of variability in Arctic sea-ice drift speed. *Journal of Geophysical Research: Oceans*, *119*, 1–21. doi:10.1002/2014JC009897

Parkinson, C. L., and Cavalieri, D. J. (2008). Arctic sea ice variability and trends, 1979–2006. *Journal of Geophysical Research*, *113*(C07003), 1–28. doi:10.1029/2007JC004558

Perovich, D. K., Light, B., Eicken, H., Jones, K. F., Runciman, K., and Nghiem, S. V. (2007). Increasing solar heating of the Arctic Ocean and adjacent seas, 1979 - 2005: Attribution and role in the ice-albedo feedback. *Geophysical Research Letters*, *34*(L19505), 1–5. doi:10.1029/2007GL031480

Perovich, D. K., and Richter-Menge, J. A. (2009). Loss of Sea Ice in the Arctic. *Annual Review of Marine Science*, (1), 417–443. doi:10.1146/annurev.marine.010908.163805

Perovich, D. K., Richter-Menge, J. A., Jones, K. F., and Light, B. (2008). Sunlight, water, and ice: Extreme Arctic sea ice melt during the summer of 2007. *Geophysical Research Letters*, *35*(L11501), 1–4. doi:10.1029/2008GL034007

Pizzolato, L., Howell, S. E. L., Derksen, C., Dawson, J., and Copland, L. (2014). Changing sea ice conditions and marine transportation activity in Canadian Arctic waters between 1990 and 2012. *Climatic Change*, *123*(2), 161–173. doi:10.1007/s10584-013-1038-3

Polyakov, I. V., Walsh, J. E., and Kwok, R. (2012). Recent Changes of Arctic Multiyear Sea Ice Coverage and the Likely Causes. *Bulletin of the American Meteorological Society*, (February), 145–151. doi:10.1175/BAMS-D-11-00070.1

Post, E., Bhatt, U. S., Bitz, C. M., Brodie, J. F., Fulton, T. L., Hebblewhite, M., … Walker, D. A. (2013). Ecological consequences of sea-ice decline. *Science*, *341*(6145), 519–524. doi:10.1126/science.1235225

Proshutinsky, A., Bourke, R. H., and McLaughlin, F. A. (2002). The role of the Beaufort Gyre in Arctic climate variability: Seasonal to decadal climate scales. *Geophysical Research Letters*, *29*(23), 1–4. doi:10.1029/2002GL015847

Rampal, P., Weiss, J., and Marsan, D. (2009). Positive trend in the mean speed and deformation rate of Arctic sea ice, 1979–2007. *Journal of Geophysical Research*, *114*(C5), 1–14. doi:10.1029/2008JC005066

Rigor, I. G. (2002). IABP drifting buoy, pressure, temperature, position and interpolated ice velocity. Compiled by the Polar Science Center, Applied Physics Laboratory, University of Washington, Seattle, in association with NSIDC, Boulder, CO: National Snow and Ice Data Center. Retrieved from http://dx.doi.org/10.7265/N53X84K7

Rigor, I. G., and Wallace, J. M. (2004). Variations in the age of Arctic sea-ice and summer sea-ice extent. *Geophysical Research Letters*, *31*(9), 2–5. doi:10.1029/2004GL019492

Rigor, I. G., Wallace, J. M., and Colony, R. L. (2002). Response of Sea Ice to the Arctic Oscillation. *Journal of Climate*, *15*(18), 2648–2663. doi:10.1175/1520-0442(2002)015<2648:ROSITT>2.0.CO;2

Rosen, P. A., Esien, H., Shen, Y., Hensley, S., Shaffer, S., Veilleux, L., … Joughin, I. (2010). DESDynl - Deformation, Ecosystem Structure and Dynamics of Ice. In *90th American Meterological Society Annual Meeting* (p. 39). Atlanta, Georgia.

Rothrock, D. A., Yu, Y., and Maykut, G. A. (1999). Thinning of the Arctic sea-ice cover. *Geophysical Research Letters*, *26*(23), 3469–3472. doi:10.1029/1999GL010863

Screen, J. A., and Simmonds, I. (2010). The central role of diminishing sea ice in recent Arctic temperature amplification. *Nature*, *464*(7293), 1334–7. doi:10.1038/nature09051

Serreze, M. C., and Barrett, A. P. (2011). Characteristics of the Beaufort Sea High. *Journal of Climate*, *24*(1), 159–182. doi:10.1175/2010JCLI3636.1

Serreze, M. C., Barrett, A. P., Stroeve, J. C., Kindig, D. N., and Holland, M. M. (2009). The emergence of surface-based Arctic amplification. *The Cryosphere*, *3*(1), 11–19. doi:10.5194/tc-3-11-2009

Serreze, M. C., and Barry, R. G. (2009). *The Arctic Climate System* (p. 404). Cambridge University Press.

Serreze, M. C., Holland, M. M., and Stroeve, J. (2007). Perspectives on the Arctic's shrinking sea-ice cover. *Science*, *315*, 1533–1536. doi:10.1126/science.1139426

Simmonds, I., and Rudeva, I. (2012). The great arctic cyclone of August 2012. *Geophysical Research Letters*. doi:10.1029/2012GL054259

Smith, L. C., and Stephenson, S. R. (2013). New Trans-Arctic shipping routes navigable by midcentury. *Proceedings of the National Academy of Sciences of the United States of America*, *110*(13), 6–10. doi:10.1073/pnas.1214212110

Smith, S. D., Muench, R. D., and Pease, C. H. (1990). Polynyas and Leads: An Overview of Physical Processes and Environment. *Journal of Geophysical Research*, *95*(C6), 9461–9479. doi:10.1029/JC095iC06p09461

Spreen, G., Kwok, R., and Menemenlis, D. (2011). Trends in Arctic sea ice drift and role of wind forcing: 1992–2009. *Geophysical Research Letters*, *38*(19), 1–6. doi:10.1029/2011GL048970

Steele, M., Ermold, W., and Zhang, J. (2008). Arctic Ocean surface warming trends over the past 100 years. *Geophysical Research Letters*, *35*(L02614), 1–6. doi:10.1029/2007GL031651

Stephenson, S. R., Smith, L. C., and Agnew, J. A. (2011). Divergent long-term trajectories of human access to the Arctic. *Nature Climate Change*, *1*(3), 156–160. doi:10.1038/nclimate1120

Stewart, E. J., Howell, S. E. L., Draper, D., Yackel, J., and Tivy, A. (2007). Sea Ice in Canada's Arctic: Implications for Cruise Tourism. *Arctic*, *60*(4), 370–380. doi:10.14430/arctic194

Stroeve, J. C., Markus, T., Boisvert, L., Miller, J., and Barrett, A. (2014). Changes in Arctic melt season and implications for sea ice loss. *Geophysical Research Letters*, *41*(4), 1216–1225. doi:10.1002/2013GL058951

Stroeve, J. C., Maslanik, J., Serreze, M. C., Rigor, I., Meier, W., and Fowler, C. (2011). Sea ice response to an extreme negative phase of the Arctic Oscillation during winter 2009/2010. *Geophysical Research Letters*, *38*(2), 1–6. doi:10.1029/2010GL045662

Stroeve, J. C., Serreze, M. C., Holland, M. M., Kay, J. E., Maslanik, J., and Barrett, A. P. (2012). The Arctic's rapidly shrinking sea ice cover: a research synthesis. *Climatic Change*, *110*(3-4), 1005–1027. doi:10.1007/s10584-011-0101-1

Stroeve, J., Markus, T., Meier, W. N., and Miller, J. (2006). Recent changes in the Arctic melt season. *Annals of Glaciology*, *44*(1), 367–374. doi:10.3189/172756406781811583

Sturm, M., Perovich, D. K., and Holmgren, J. (2002). Thermal conductivity and heat transfer through the snow on the ice of the Beaufort Sea. *Journal of Geophysical Research*, *107*(C21). doi:10.1029/2000JC000409

Thompson, A. A. (2010). Innovative Capabilities of the RADARSAT Constellation Mission. In *8th European Conference on Synthetic Aperture Radar* (pp. 1–3). Aachen, Germany: VDE VERLAG.

Thompson, D. W. J., and Wallace, J. M. (1998). The Arctic oscillation signature in the wintertime geopotential height and temperature fields. *Geophysical Research Letters*, *25*(9), 1297–1300. doi:10.1029/98GL00950

Thorndike, A. S., and Colony, R. (1982). Sea ice motion in response to geostrophic winds. *Journal of Geophysical Research*, *87*(C8), 5845–5852. doi:10.1029/JC087iC08p05845

Tivy, A., Howell, S. E. L., Alt, B., McCourt, S., Chagnon, R., Crocker, G., … Yackel, J. J. (2011). Trends and variability in summer sea ice cover in the Canadian Arctic based on the Canadian Ice Service Digital Archive, 1960–2008 and 1968–2008. *Journal of Geophysical Research*, *116*(C3), 1–25. doi:10.1029/2009JC005855

Wadhams, P. (2000). *Ice in the Ocean* (1st ed., p. 364). CRC Press.

Wang, J., Zhang, J., Watanabe, E., Ikeda, M., Mizobata, K., Walsh, J. E., … Wu, B. (2009). Is the Dipole Anomaly a major driver to record lows in Arctic summer sea ice extent? *Geophysical Research Letters*, *36*(5), 1–5. doi:10.1029/2008GL036706

Wang, X., and Key, J. R. (2003). Recent Trends in Arctic Surface, Cloud, and Radiation Properties from Space. *Science*, *299*, 1725–1728. doi:10.1126/science.1078065

Wang, X., and Key, J. R. (2005). Arctic Surface, Cloud, and Radiation Properties Based on the AVHRR Polar Pathfinder Dataset. Part I: Spatial and Temporal Characteristics. *Journal of Climate*, *18*, 2558–2574. doi:10.1175/JCLI3438.1

Wang, X. L., and Swail, V. R. (2001). Changes of Extreme Wave Heights in Northern Hemisphere Oceans and Related Atmospheric Circulation Regimes. *Journal of Climate*, *14*, 2204–2221. doi:10.1175/1520-0442(2001)014<2204:COEWHI>2.0.CO;2

WMO. (1970). *WMO sea ice nomenclature* (p. 147). Geneva: World Meteorological Organization.

Wohlleben, T., Howell, S. E. L., Agnew, T., and Komarov, A. (2013). Sea-Ice Motion and Flux within the Prince Gustaf Adolf Sea, Queen Elizabeth Islands, Canada during 2010. *Atmosphere-Ocean*, *51*(1), 1–17. doi:10.1080/07055900.2012.750232

Zhang, J., and Hibler, W. D. I. (1997). On an efficient numerical method for modeling sea ice dynamics. *Journal of Geophysical Research*, *102*(C4), 8691–8702. doi:10.1029/96JC03744

Zhang, J., Lindsay, R., Schweiger, A., and Rigor, I. (2012). Recent changes in the dynamic properties of declining Arctic sea ice: A model study. *Geophysical Research Letters*, *39*(20), 1–6. doi:10.1029/2012GL053545

Zhang, J., and Rothrock, D. (2001). A Thickness and Enthalpy Distribution Sea-Ice Model. *Journal of Physical Oceanography*, *31*(1), 2986–3001. doi:10.1175/1520-0485(2001)031<2986:ATAEDS>2.0.CO;2

Zhang, J., and Rothrock, D. A. (2003). Modeling Global Sea Ice with a Thickness and Enthalpy Distribution Model in Generalized Curvilinear Coordinates. *Monthly Weather Review*, *131*(5), 845–861. doi:10.1175/1520-0493(2003)131<0845:MGSIWA>2.0.CO;2

Zhang, J., Rothrock, D., and Steele, M. (2000a). Recent Changes in Arctic Sea Ice: The Interplay between Ice Dynamics and Thermodynamics. *Journal of Climate*, *13*, 3099–3114.

Zhang, M. (2004). Cloud-climate feedback: how much do we know. In X. Zhu, X. Li, M. Cai, S. Zhou, Y. Zhu, F.-F. Jin, … M. Zhang (Eds.), *Observation, Theory, and Modeling of Atmospheric Variability, World Scientific Series on Meterology of East Asia 3* (Vol. 3, pp. 1–23). Singapore: World Scientific Publishing Co.

Zhang, X., Vincent, L. A., Hogg, W. D., and Niitsoo, A. (2000b). Temperature and precipitation trends in Canada during the 20th century. *Atmosphere-Ocean*, *38*(3), 395–429. doi:10.1080/07055900.2000.9649654